GSI

Dipl. 2011 - 01
January

Development of an Ion Trap Experiment for the Measurement of the Electron Magnetic Moment by Double-Resonance Spectroscopy

David-Friedrich Freiherr von Lindenfels

(Diplomarbeit der Ruprecht-Karls-Universität Heidelberg)

GSI Helmholtzzentrum für Schwerionenforschung GmbH
Planckstraße 1 · D-64291 Darmstadt · Germany
Postfach 11 05 52 · D-64220 Darmstadt · Germany

Fakultät für Physik und Astronomie

Ruprecht-Karls-Universität Heidelberg

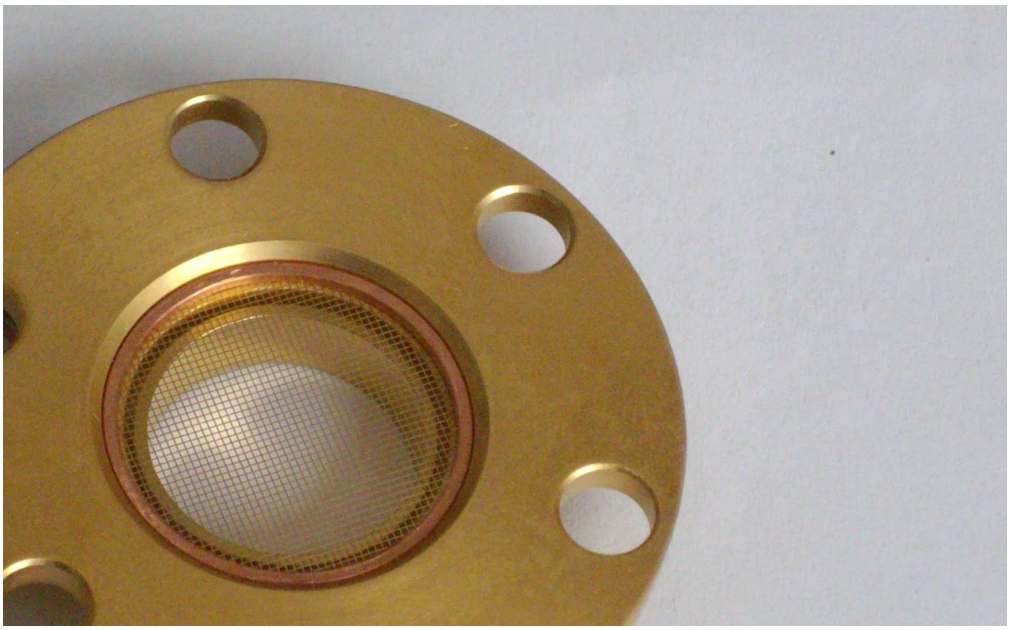

Diplomarbeit

Im Studiengang Physik

vorgelegt von

David-Friedrich Freiherr von Lindenfels

aus Lüneburg

2010

Development of an Ion Trap Experiment for the Measurement of the Electron Magnetic Moment by Double-Resonance Spectroscopy

Die Diplomarbeit wurde von

David-Friedrich Freiherr von Lindenfels

ausgeführt am

GSI Helmholtzzentrum für Schwerionenforschung GmbH

unter der Betreuung von

Herrn Priv.-Doz. Dr. Wolfgang Quint

Development of an Ion Trap Experiment for the Measurement of the Electron Magnetic Moment by Double-Resonance Spectroscopy. Abstract:
Precise determination of bound-electron g-factors in highly charged ions provides stringent tests for state-of-the-art theoretical calculations. The scope reaches from relativistic electron correlation effects on the one hand to bound-state QED terms on the other. Besides, the investigation can contribute to the determination of the fine-structure constant α. In a first approach with boron-like ions with spinless nuclei (e.g. $^{40}Ar^{13+}$ and $^{40}Ca^{15+}$), we will excite the $2\,^2P_{1/2} - 2\,^2P_{3/2}$ fine-structure transition with laser radiation and probe microwave transitions between Zeeman sub-levels in the magnetic field of a Penning trap. From this laser-microwave double-resonance technique the g-factor can be determined on a ppb level of accuracy. We have prepared a cryogenic trap assembly with a creation trap and a spectroscopy trap—a half-open compensated cylindrical Penning trap. Argon gas will be injected through a remotely controlled valve, working at cryogenic temperature and in the field of a superconducting magnet. Ions are produced by electron impact ionization with electrons from a field emission source. In the future, the trap will be connected to the HITRAP facility at GSI, and the method will be applied to hyperfine-structure transitions of hydrogen-like heavy ions in order to measure electronic and nuclear magnetic moments. This thesis presents important preparations towards the experiment.

Title: The upper end cap electrode with spectroscopy mesh attached and correction electrode below, gold-plated.

Entwicklung eines Ionenfallenxperiments zur Messung des magnetischen Moments des Elektrons mithilfe von Doppelresonanzspektroskopie. Zusammenfassung:
Die präzise Messung von g-Faktoren gebundener Elektronen in hochgeladenen Ionen stellt einen wichtigen Test für die aktuellsten theoretischen Berechnungen dar. Dabei werden beispielsweise relativistische Effekte der Elektronenkorrelation und Phänomene der QED gebundener Zustände berücksichtigt. Dies kann zur Bestimmung der Feinstrukturkonstante α beitragen. Zunächst arbeiten wir mit Bor-ähnlichen Ionen mit spinlosen Kernen, z.B. $^{40}Ar^{13+}$ und $^{40}Ca^{15+}$. Mit Laserstrahlung regen wir den Feinstrukturübergang $2\,^2P_{1/2} - 2\,^2P_{3/2}$ an und messen Mikrowellenübergänge zwischen Zeeman-Unterzuständen im Magnetfeld einer Penningfalle. Diese Laser-Mikrowellen Doppelresonanztechnik erlaubt es, den g-Faktor mit neunstelliger Genauigkeit zu bestimmen. Wir haben einen kryogenen Fallenturm entwickelt, der aus einer Erzeugungsfalle und einer Spektroskopiefalle besteht – letztere ist eine halboffene kompensierte zylindrische Penningfalle. Argongas wird durch ein ferngesteuertes Ventil eingelassen, das sich bei kryogener Temperatur im Feld eines Supraleitenden Magneten befindet. Die Ionenerzeugung erfolgt durch Stoßionisation mit Elektronen aus einer Feldemissionsquelle. In Zukunft wird die Falle an die HITRAP-Anlage der GSI angeschlossen. Dann wird die Spektroskopiemethode auf Hyperfeinstrukturübergänge Wasserstoffähnlicher Schwerionen angewandt, um magnetische Momente von Elektronen und Kernen zu messen. Diese Arbeit stellt wichtige Vorbereitungen für das Experiment vor.

Titel: Die obere Endkappe mit angebrachtem transparenten Netz und über einer Korrekturelektode, vergoldet.

Contents

List of Figures

List of Tables

Chapter 1

Motivation and Introduction

Measurements of the electron magnetic moment have been milestones towards an understanding of the quantum behavior of nature during the past century. The observation of the Zeeman effect and the Stern-Gerlach experiment demonstrated the spatial quantization of angular momenta [SG22, Vog09] and eventually inspired the discovery of the electron spin [MR82, Hun75]. The fundamental description of electrons with the Dirac equation explained the value two instead of the classical expectation of unity for the g-factor [Dir28].

Precise atomic physics experiments by Kusch and Foley [KF47, KF48] revealed a deviation from two in the per mil regime. This was an impressive confirmation for the quantum formalism of electrodynamics (QED) [Sch48] in the late 1940s. The tradition of comparing precision measurements with advancing calculations has been continued successfully both for bound atomic states and fundamental particles such as single electrons a Penning trap. For the free electron, QED effects have been calculated to the four-loop order [AHKN07], resulting in a theoretical g-factor of 2.002 319 304 365 6(154). A measurement of this quantity at Harvard University [HFG08] yielded 2.002 319 304 361 46(56), which is one of the most precise tests in physics.

The accuracy of the theoretical value is currently limited by the uncertainty in our knowledge of the fine-structure constant α. If QED itself and the calculations are exact, the tremendous precision can be used to determine this fundamental quantity with smaller uncertainty. However, independent determinations of α are required to validate this assumption. Heavy-ion experiments are a good candidate for this purpose. Depending on the physical system, the g-factor has different values due to different effects such as binding corrections, nuclear structure and inter-electronic correlation [Vog09]. Also QED effects are enhanced by the strong fields close to heavy nuclei. They can be refined from other corrections, if hydrogen-, lithium- and boron-like states of the same nuclide (that is, with one, three or five electrons bound to the nucleus) are compared to each other. In the same sense as for the free electron, this can be used as a probe for the fine-structure constant [SGO$^+$06].

Particular interest has also risen in studying the variation of α in time [FK07]. The constant is derived from the electroweak unification as a product of the weak coupling constant and the sine square of the Weinberg angle [Wei67]. Here, we find dimensionless numbers which are fundamental in the sense that we don't know a mathematical derivation for their values. There are speculations that parameters of the most fundamental theories are floating and somewhere in space-time lead

to a combination which allows our existence. What we perceive as fine tuning of fundamental constants, would be explained by chance [FK07]. Probing for this claim concerns the foundations of our world view. However, the current limit on the time variation $\dot{\alpha}/\alpha = (-1.6 \pm 2.3) \cdot 10^{-17}\ \mathrm{yr}^{-1}$ from comparison of $^{27}Al^{+}$ and $^{199}Hg^{+}$ single-atom optical clocks [RHS^{+}08, CHK^{+}10] is consistent with zero. Absolute determinations of the fine-structure constant still lack the tremendous accuracy required for a variation measurement. Nevertheless, such philosophical questions about our existence are a strong motivation for high-precision experiments.

History also shows that a fundamental understanding of the laws of nature has triggered many technological developments that now contribute to our welfare. Accurate verification of theoretical predictions is a necessary link in this chain. Besides the test of state-of-the art QED calculations and the determination of fundamental constants, the study of hydrogen-like ions will also yield data for nuclear magnetic moments without the presence of diamagnetic shielding. On the one hand, this reaches out to nuclear physics; on the other, the information can be used to benchmark models of this shielding due to the atomic shell [QMSV08].

Experiments with light hydrogen-like ions in Penning traps have already proven suitable for measurements with outstanding accuracy. For instance, the g-factor determinations of the electron in hydrogen-like carbon $^{12}C^{5+}$ and oxygen $^{16}O^{7+}$ ions, respectively, have supplied the most precise value of the electron mass to date [HBH^{+}00, VDS^{+}04, SGS^{+}02, PCJY05, BHH^{+}02]. These experiments employed the continuous Stern-Gerlach effect [DE73]. Measurements with hydrogen-like silicon and calcium are under preparation. The subject of the present experiment is the g-factor of boron-like argon $^{40}Ar^{13+}$. In contrast to the other examples of light and medium-heavy ions mentioned before, we will apply a laser-microwave double-resonance technique for this determination [LBB^{+}11]. The boron-like charge state of the spinless argon nuclide is well suited for this method, because it has a fine-structure transition in the optical regime [LJCLU^{+}05]. We can measure the Zeeman splitting of this line and profit from the well-defined conditions in a Penning trap at liquid helium temperature. Thus, our project forms an important contribution to the series of precise g-factor determinations for different nuclear charges.

We also consider the bound-electron g-factor measurement in highly charged argon as a pilot study for future experiments. The setup is situated next to the HITRAP facility (highly charged ions trap) at GSI in Darmstadt. With few modifications we will investigate—for instance—the hyperfine structure of hydrogen-like bismuth $^{209}Bi^{82+}$.

My work stands at the beginning of the installations for the HITRAP g-factor experiment. The design of the spectroscopy trap was accomplished in an internship of eight weeks just after the measurement technique had been proposed [QMSV08]. During the editing time of this thesis, we planned and constructed an ion source for off-line experiments. Many details for the optical excitation and detection were implemented and await completion.

The experimental parameters—the field of a superconducting magnet, liquid helium temperature, high and ultra-high vacuum (UHV) and fluorescence intensities corresponding to a hundred photons per second—are an exotic combination. We repeatedly face the demanding situation that there is little industrial experience and poor willingness to develop solutions for a single customer. This, however, led to new developments, in particular a cryogenic gas valve, which has been conceived by the community with great interest.

In the following chapter 2, I give an excursus about different theoretical models for the g-

factor. Then I explain our method to determine this quantity experimentally (chapter 3). Chapter 4 introduces the general setup and describes several components. It is followed by a detailed discussion of the spectroscopy trap in chapter 5. Here I explain why a harmonic trapping potential is required and how we achieve it. This entity allows for spectroscopy with highly charged medium-heavy and heavy ions almost at rest in a well-defined electromagnetic field.

Chapter 6 first presents the principle of charge-breeding in an electron beam ion source (EBIS) and relates this to the production of Ar^{13+} with an ionization threshold of 686 eV. The novel development of a cryogenic gas valve is introduced in the second section, together with details of the design and first simulations. It has been particularly designed for the injection of controlled amounts of argon gas. Nevertheless, it will be applicable to other gases with similar thermodynamical properties.

The EBIS is completed by a field emission source of electrons, which can also be used for ion cooling and excitation. Chapter 7 starts with an explanation of the quantum physical process of field emission. The following sections report on the production and test of the field emission points (FEP).

Chapter 8 summarizes the results of this thesis and gives an outlook on the immediate next steps in the experimental preparations. Finally we throw a glance at the placement of our experiment in the HITRAP project.

Chapter 2

The Bound Electron g-Factor

We are preparing an experiment which is designed to measure the magnetic moment of bound electrons, or the closely related g-factor. In this chapter I want to define these quantities. The following sections give some theoretical background and link the g-factor to the fine structure constant.

2.1 Angular Momenta and Magnetic Moments

The angular momentum $\vec{J}$ of a particle defines a spatial direction and can be aligned with respect to a magnetic field $\vec{B} = B\vec{e}_z$. If the particle has electric charge, this is connected with a potential energy. The coupling strength is measured by the magnetic (dipole) moment $\vec{\mu}$:

$$V_{\vec{\mu}} = -\vec{\mu} \cdot \vec{B}. \tag{2.1}$$

Vector quantities of elementary particles are traced back to the angular momentum. So we can define a proportionality constant, the gyromagnetic factor, which is also called Landé factor or simply g-factor [HW00, Vog09]:

$$\frac{\vec{\mu}_J}{\mu_B} = g_J \cdot \frac{\vec{J}}{\hbar}. \tag{2.2}$$

Throughout the entire present thesis, lower-case m denotes the electron mass and e the elementary charge, if not other specified. The Bohr magneton $\mu_B = e\hbar/2m$ is a measure of the charge-to-mass ratio of the electron and Planck's constant $\hbar = h/2\pi$ is the unit of angular momentum. The projection of a momentum to the magnetic field axis can only be changed by multiples of this number. This leads to discrete levels, separated by the energy

$$\Delta E \equiv \hbar\omega_L = g_J \mu_B B \tag{2.3}$$

with the Larmor frequency ω_L. Orbital angular momenta have $g_L = 1$, whereas for spin momenta g_S is ca. 2.

The angular momentum $\vec{j}$ of a single bound electron has an according g-factor g_j. It can be approximately understood in the vector model of angular momenta [Foo05]. The total angular momentum is regarded as a vector sum of the momenta $\vec{l}$ and $\vec{s}$, while $\vec{\mu}_j$ is composed of their magnetic moments. Since the respective g-factors are not equal, the vector

$$\vec{\mu}_j = \frac{\mu_B}{\hbar}(g_l\vec{l} + g_s\vec{s})$$

is not necessarily parallel to $\vec{j}$. The vector model states that $\vec{j}$ is aligned with the magnetic field and therefore only the projection $(\vec{\mu}_j \cdot \vec{j})\vec{j}/|\vec{j}|^2$ contributes to the interaction H_{int}, which leads to very similar equations as 2.1 and 2.2:

$$H_{\text{int}} = -\vec{\mu}_j \cdot \vec{B} \equiv g_j \mu_B \frac{\vec{j}}{\hbar} \cdot \vec{B}. \tag{2.4}$$

First we calculate

$$\begin{aligned}
\vec{j} \cdot \vec{\mu}_j &= \frac{\mu_B}{\hbar}\vec{j} \cdot (g_l\vec{l} + g_s\vec{s}) \approx \frac{\mu_B}{\hbar}\vec{j} \cdot (\vec{j} + \vec{s}) \\
&= \frac{\mu_B}{\hbar}\left(|\vec{j}|^2 + \frac{1}{2}(|\vec{j}|^2 + |\vec{s}|^2 - |\vec{l}|^2)\right) \\
&= \mu_B\hbar\frac{1}{2}\left(3j(j+1) + s(s+1) - l(l+1)\right).
\end{aligned}$$

Since the total angular momentum is parallel to the magnetic field, we can replace $\vec{B}$ in the defining equation 2.4:

$$\begin{aligned}
\vec{\mu}_j \cdot \vec{j} &= -g_j\mu_B\frac{\vec{j}}{\hbar} \cdot \vec{j} = -g_j\mu_B j(j+1)\hbar \\
\Rightarrow -g_j &\approx \frac{3}{2} + \frac{s(s+1) - l(l+1)}{2j(j+1)}.
\end{aligned}$$

The minus sign comes from the negative charge of the electron. Usually the g-factor is defined positive. For $l = 1$ and $s = 1/2$, we evaluate

$$g_{1/2} \approx \frac{2}{3}, \quad g_{3/2} \approx \frac{4}{3}. \tag{2.5}$$

The approximation neglects the relativistic mass enhancement of the electron, if it is strongly bound to the Coulomb potential of a nucleus with Z protons. For a relativistic treatment, we must solve the Dirac equation [Dir28],

$$E\psi(\vec{r}) = \left(-\imath\hbar c\vec{\alpha} \cdot \vec{\nabla} - \frac{Z\alpha\hbar c}{r} + mc^2\alpha_0\right)\psi(\vec{r}). \tag{2.6}$$

$\vec{\alpha}$ and α_0 are complex 4×4 matrices and $\alpha = e^2/(4\pi\varepsilon_0\hbar c)$ is the fine-structure constant. The expressions

$$E_{n\kappa} = mc^2 \left(1 + \left(\frac{Z\alpha}{n - \kappa + \sqrt{\kappa^2 - (Z\alpha)^2}}\right)^2\right)^{-\frac{1}{2}}$$
$$g_D = \frac{\kappa}{j(j+1)} \left(\kappa \frac{E_{n\kappa}}{mc^2} - \frac{1}{2}\right) \tag{2.7}$$

stand for the energy and g-factor of a single Dirac electron with principle quantum number n and Dirac quantum number $\kappa = (-1)^{j+l+1/2}(j+1/2)$, bound to a point-like nucleus [Zap79, SGO+06]. We find the leading order of the binding correction in the $2p_{1/2}$ and $2p_{3/2}$ state in hydrogen-like argon ($Z = 18$):

$$g_{1/2} = \frac{2}{3} - \frac{1}{6}(Z\alpha)^2 + \cdots \approx 0.6638,$$
$$g_{3/2} = \frac{4}{3} - \frac{2}{15}(Z\alpha)^2 + \cdots \approx 1.331. \tag{2.8}$$

The correction for the ground state has been predicted by Breit [Bre28] to be:

$$g_{1s} = 2 - \frac{2}{3}(Z\alpha)^2 + \cdots \approx 1.988. \tag{2.9}$$

2.2 Quantum Electrodynamics and Nuclear Corrections

Quantum electrodynamics (QED) causes further shifts, that also depend on the quantum state [PSS+97]. The perturbative expansion in orders of α/π starts with

$$g_{\text{free}} = 2 + \frac{\alpha}{\pi} + \cdots \approx 2.0023 \tag{2.10}$$

for the free electron [Sch48]. As I have stated in the introduction, g-factor measurements can use the relation between the bound electron g-factor and the fine structure constant, equation 2.7 or 2.10, to probe for this fundamental quantity. For instance, if equation 2.8 was accurate, α could be extracted from a bound-electron g-factor measurement [Vog09, BDH+05] with a relative uncertainty of

$$\frac{\delta\alpha}{\alpha} = \frac{3g}{(\alpha Z)^2}\frac{\delta g}{g}. \tag{2.11}$$

An experimental accuracy of $\delta g/g = 7 \cdot 10^{-10}$ for bound-electron g-factor measurements in highly charged lead ions could lead to a relative uncertainty of $4 \cdot 10^{-9}$ in the determination of α from an idealized heavy-ion experiment. Such an accuracy has already been achieved in measurements with hydrogen-like carbon and oxygen ions [Her00, HBH+00, VDS+04, BDH+05]. This is comparable to the accuracy of the value $\alpha^{-1} = 137.035\,999\,45(62)$, obtained by atom recoil experiments [CdMC+08]. They provide the best determination except for the extraction from measurements of the anomalous magnetic moment of the electron (the g-factor), which are about an order of

magnitude more precise [SVDJD81, Deh84, HFG08].

For an accurate treatment of the bound-electron g-factor, also nuclear effects have to be considered [PSS$^+$97, Qui95]. They can form serious difficulties, since in many cases the nuclear properties are not known well enough. However, nuclear structure contributions to the bound-electron g-factor cancel to a high degree in a specific difference of the g-factors for $1s_{1/2}$ and $2p_{1/2}$ states, so that α can be extracted with the accuracy stated above, provided all other corrections are evaluated to the required level [SGO$^+$06]. The application of this method is made possible by comparing bound electron g-factors in hydrogen-like and boron-like heavy ions, as for example in lead $^{208}\mathrm{Pb}^{81+}$ and $^{208}\mathrm{Pb}^{77+}$. Here, the interaction of multiple electrons comes into play, because in an atomic ground state with an unpaired p-electron, the lower-lying s-shells are occupied. (This is why I use capital letters for electronic terms in the following chapters.)

The great potential of the cancellation method in heavy ions mainly has two reasons: Firstly, the energy-equivalent of the electron mass is negligible compared to its potential energy close to the nucleus. The ratio $Z\alpha\hbar c/R_{\mathrm{nuc}}$ to mc^2 is only 3.6 in hydrogen, 12.5 in argon, but 33 in lead. This simplifies the Dirac equation 2.6 and minimizes the qualitative difference between $s_{1/2}$ and $p_{1/2}$ wave functions. Secondly, the inter-electronic correlation effects are suppressed by the inverse of the nuclear charge, compared to the attractive central force. Therefore, and because of the scaling of equation 2.11 with the nuclear charge, the sensitivity of the bound-electron g-factor to the fine-structure constant is less pronounced in case of medium-heavy ions. Altogether this results in an uncertainty $\delta\alpha/\alpha$ at least 30 times higher than what is possible for heavy ions.

However, the study of g-factors in medium-heavy ions, as for example argon, has a further interesting aspect: Electron correlation corrections to the g-factor are of purely relativistic origin. So their measurement serves as a sensitive probe of relativistic electron correlation effects in a regime where these effects are stronger than in light ions, but where higher orders in the inverse nuclear charge are not yet suppressed by a too high nuclear charge. I close this theoretical section with a quick estimation for the electronic g-factor in the ground state of boron-like argon [Sha10]: The unperturbed value from the Dirac theory (eqn. 2.7) is 0.663 775 447. The inter-electronic correlation contributes with 0.000 650 0, which is overcompensated by the QED shift −0.000 768 7. Finite nuclear size effects are immeasurably small, and the nuclear recoil correction −0.000 009 8 plays a minor role. Altogether, the preliminary theoretical g-factor is 0.663 647(1) for the atomic system $^{40}\mathrm{Ar}^{13+}$, which is studied in this thesis.

Chapter 3

Measurement Principle

A Penning ion trap supplies the magnetic field B which is required for the Larmor frequency to be in the microwave regime. We modify equation 2.3 to the from

$$\omega_L = \frac{g}{2}\frac{e}{m}B \tag{3.1}$$

and note that it resembles the cyclotron frequency of a stored ion with the known charge-to-mass ratio Q/M,

$$\omega_c = \frac{Q}{M}B. \tag{3.2}$$

The latter relation is used to calibrate the magnetic field. This is the basis of g-factor measurements in a Penning trap: The ratio of the two frequencies can be determined very precisely and it is independent[1] of the magnetic field—only the mass ratio of electron and ion enters as an external parameter. The ion charge Q is assumed to be an exact multiple of the elementary charge. The g-factor is then given by

$$g = 2\frac{\omega_L}{\omega_c}\frac{m}{M}\frac{Q}{e}. \tag{3.3}$$

Using this relation, bound-electron g-factors of hydrogen-like carbon and oxygen have been measured with high accuracy [Vog09, HBH$^+$00, VDS$^+$04]. Theses experiments used the method of the so-called 'continuous Stern-Gerlach effect' [DE73]: In an inhomogeneous magnetic field, a spin flip causes a frequency shift. This can be exploited to detect the spin state.

The following section explains another option for a measurement of the Larmor frequency, namely double-resonance spectroscopy. Its application to hyperfine transitions in heavy highly charged ions has been proposed in [QMSV08]. Here we apply it to a fine-structure transition in

[1] This holds for the linear Zeeman effect and is an approximation of the more general Breit-Rabi formula [QMSV08]. If the magnetic field is too strong, it cannot be seen as a perturbation to the fine structure coupled levels (Paschen-Back effect). The magnetic field of 7 T is weak in the sense that the Zeeman splitting is much smaller than the fine structure splitting, as the numbers given in section 3.1 demonstrate. However, for a precise analysis, this effect needs to be considered.

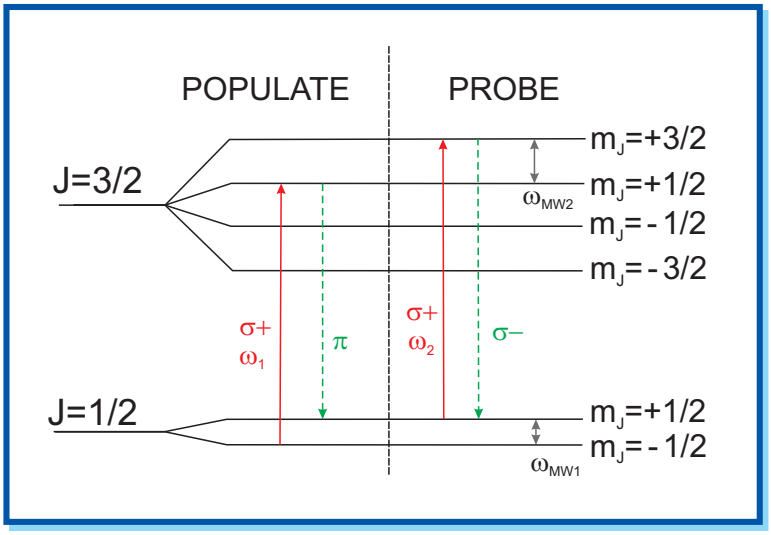

Figure 3.1: Spectroscopy on the $2\,^2P_{1/2}$ – $2\,^2P_{3/2}$ fine-structure transition in a boron-like argon ion with Zeeman effect. The level scheme (not to scale) and measurement principle for the double-resonance technique are shown. Solid arrows indicate excitation by laser and microwave photons [QMSV08].

a medium-heavy highly charged system. Section 3.2 summarizes the principles of a Penning trap, which includes the determination of the cyclotron frequency as a standard method.

3.1 Laser-Microwave Double-Resonance Spectroscopy

Boron-like ions have one valence electron in the $2p$ shell. The splitting of the two fine-structure levels $^2P_{1/2}$ and $^2P_{3/2}$ scales with the nuclear charge as Z^4. In the case of boron-like Ar^{13+}, the magnetic dipole transition between the levels can be excited with laser radiation at a wavelength of about $\lambda = 441$ nm [DCLUD$^+$03]. The magnetic field of 7 T in the Penning trap leads to further splitting into Zeeman sub-levels with a spacing of $\omega_{\mathrm{MW1}} = 2\pi \cdot 65$ GHz in the $^2P_{1/2}$ state and $\omega_{\mathrm{MW2}} = 2\pi \cdot 130$ GHz in the $^2P_{3/2}$ state (see figure 3.1). A laser at frequency ω_1 resonantly depopulates the lowest Zeeman sub-state $|J, m_J\rangle = |1/2, -1/2\rangle$ by optical pumping. Then a closed cycle between extreme sub-levels $|1/2, +1/2\rangle$ and $|3/2, +3/2\rangle$ is driven at the laser frequency ω_2—the spontaneous decay of the state $|1/2, +1/2\rangle$ to $|1/2, -1/2\rangle$ is practically impossible on an experimental time scale.

In the normal Zeeman effect, the state-selective excitation to the extreme Zeeman sub-level $|3/2, +3/2\rangle$ would require $\sigma+$ polarized light. Different components in an unpolarized mixture would excite transitions to different states. Here, due to the J-dependent Zeeman splitting (anomalous Zeeman effect), all visible transitions between different sub-levels are separated by at least $\Delta\omega = 2\pi \cdot 65$ GHz, as seen in figure 3.2. This is much larger than the laser linewidth, the spacing of Doppler side bands or the natural linewidth. If the ions are irradiated with unpolarized light, the suitable polarization component is absorbed—other components are far off-resonant from their respective transition and have no effect.

Once the laser has been tuned to the resonance frequency ω_2, it remains there and repeatedly excites the $|3/2, +3/2\rangle$ state, which decays back to $|1/2, +1/2\rangle$. Then, tunable microwave radi-

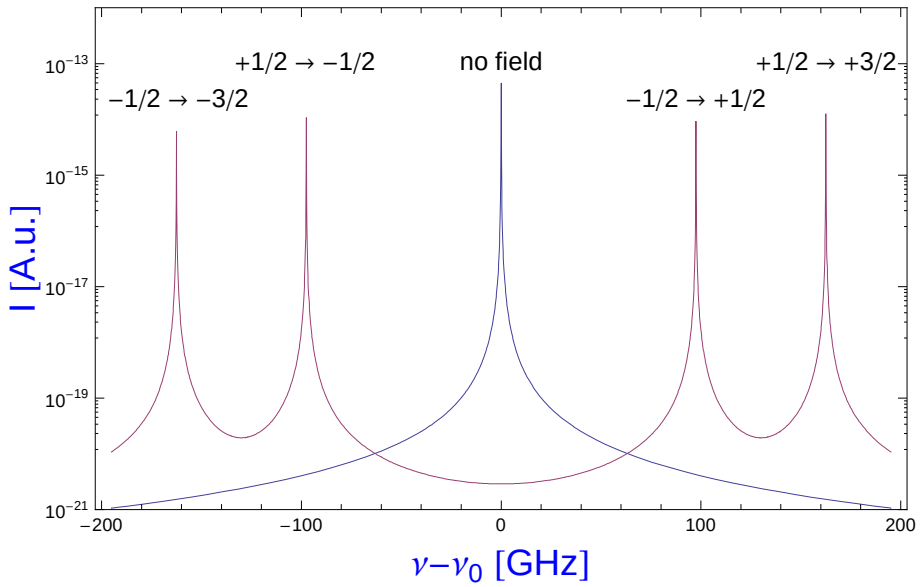

Figure 3.2: Line shape with magnetic field (4 red peaks, only circular polarization) and without field (single blue peak). ν_0 is the field-free fine-structure transition frequency.

ation is shone in. When the microwave frequency is scanned and comes into resonance with the Larmor frequency of the ions in the magnetic field, population is transferred to the $|1/2, -1/2\rangle$ level, in which the laser radiation cannot be absorbed. This results in a minimum of the observed fluorescence intensity. Thus, the visible fluorescence serves as a probe for the population of the $J = 1/2$ sub-levels, indicating resonance of the microwave radiation to the Larmor frequency. This resonance frequency, together with the cyclotron frequency ω_c, yields the g-factor (see above equation 3.3).

The lifetime of the upper fine-structure level in Ar^{13+} is 9.6 ms [LJCLU+05], which corresponds to a saturation intensity of approximately 20 nWcm^{-2}. Matching the unpolarized laser radiation with 1 MHz linewidth to the narrow transition makes a power density of 6 mWcm^{-2} necessary. An ensemble of about 10^5 trapped ions will cover a projected area of roughly 0.1 cm^2, requiring an estimated laser power of 0.6 mW. As fluorescence signal, 20 counts per second can be expected on a channel photomultiplier detector (CPM), taking into account limited solid angle, transmission losses and the detector quantum efficiency, see also section 4.3. The laser will be pulsed with a duration comparable to the upper state lifetime. During illumination, the detector is in a blind mode. Background light by photons scattered in the trap dies out after some microseconds and will not disturb when the CPM is in its sensitive mode.

3.2 Cyclotron Frequency

The measurement of the cyclotron frequency exploits basic properties of Penning traps [MGW05]: The strong homogeneous magnetic field

$$\vec{B} = (0, 0, B)$$

confines charged particles radially. A static electric quadrupole field

$$\vec{\mathcal{E}} = \frac{U_0}{2d^2}(-x, -y, 2z) \tag{3.4}$$

assures confinement in the axial direction (see chapter 5 for the definition of the parameters $U_0 < 0$ and d). The equations of motion for an ion with charge Q and mass M are derived from the Lorentz force $\vec{F} = Q(\vec{\mathcal{E}} + \vec{v} \times \vec{B})$ and can be written in the form

$$\begin{aligned} 0 &= \ddot{x} - \omega_c \dot{y} - \frac{\omega_z^2}{2} x \\ 0 &= \ddot{y} + \omega_c \dot{x} - \frac{\omega_z^2}{2} y \\ 0 &= \ddot{z} + \omega_z^2 z, \end{aligned} \tag{3.5}$$

where we use the cyclotron frequency as in equation 3.2 and the axial frequency

$$\omega_z = \sqrt{\frac{|QU_0|}{Md^2}}. \tag{3.6}$$

This set of differential equations can be solved to describe three independent motions. One is the oscillation in z-direction with the angular frequency $\omega_z \approx 2\pi \cdot 0.37$ MHz (values for Ar^{13+} in the trap that is presented in section 5.3). x and y are decoupled to the reduced cyclotron motion $a_+(t)$ and the magnetron motion $a_-(t)$ with the respective angular frequencies

$$\omega_\pm = \frac{\omega_c}{2} \pm \sqrt{\frac{\omega_c^2}{4} - \frac{\omega_z^2}{2}}. \tag{3.7}$$

ω_+ is the cyclotron frequency, modified by a small perturbation due to the electric field, and has the approximate value $2\pi \cdot 35$ MHz. The much slower magnetron motion ($\omega_- \approx 2\pi \cdot 2.0$ kHz) is a drift through the crossed electric and magnetic fields, as in a Wien filter. The invariance theorem

$$\omega_c^2 = \omega_z^2 + \omega_+^2 + \omega_-^2 \tag{3.8}$$

relates the free cyclotron frequency to the motional frequencies [BG82], which are observed in the following way: A moving charge induces image currents, which are resonantly picked up in a tuned circuit and amplified at liquid helium temperature.

Space-charge effects would corrupt the accuracy that can be reached in a dedicated precision trap [WVST06]. For this reason, the determination of motional frequencies requires the reduction to a single particle. Transporting the ions between the precision trap and a reservoir trap will allow to switch quickly between laser-microwave spectroscopy and cyclotron frequency measurement, thus minimizing the uncertainty due to a magnetic field drift.

Chapter 4

Overview of the experiment

Before going into detail about different components, I give a short overview of the general setup as depicted in figure 4.1. The experiment will be performed in a Penning trap assembly consisting of a

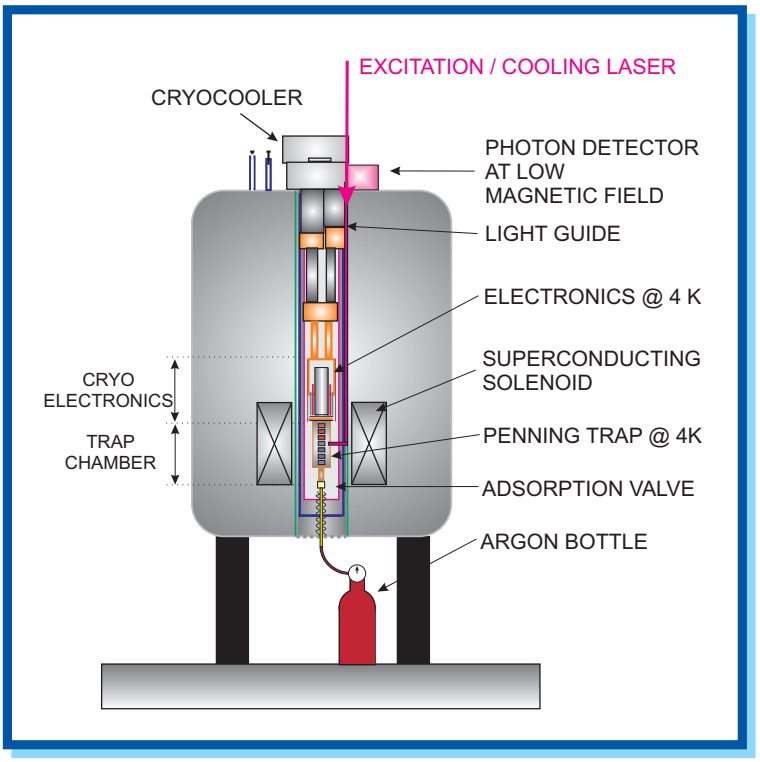

Figure 4.1: The experimental setup viewed in vertical section.

creation trap, transport electrodes and a spectroscopy trap (see fig. 4.2). The creation trap serves for ion production, intermediate storage (hence, it is also called 'reservoir trap') or capturing ions coming from the HITRAP beamline. It comprises a field emission electron source, which is discussed in chapter 7. The precision measurements of the Larmor and motional frequencies takes place in the spectroscopy trap. This trap has nearly the same electric potential as a closed compensated cylindrical Penning trap [GM84, GHR89], but is open on one side. This is detailed out in chapter 5. Ions can easily be loaded from the creation trap and there is optical access

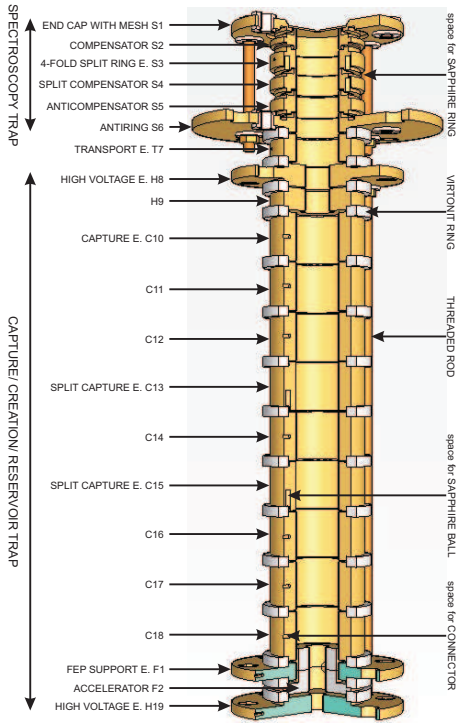

Figure 4.2: Complete trap assembly with nomenclature. E. stands for electrode. (Courtesy of N. Brantjes)

with large solid angle for spectroscopy experiments (see fig. 4.3). The electrodes are contained in an UHV chamber, made from copper. The threaded rods carrying the electrodes are attached to the mounting flange. Low and high voltage (HV) vacuum feedthroughs and a central quartz glass vacuum window for transmission of ultraviolet (UV) light are also part of the flange. The counterpart is a cylinder with a pumping tube connected to the empty port in the bottom of figure 4.4. More information about this is found in section 6.2. The copper vacuum chamber is sealed with an indium ring.

Together with resonator coils, amplifiers, lenses and a multi-fiber light guide, the chamber is suspended from a pulse-tube cooler in the evacuated (warm) bore of a superconducting magnet. The cooler, magnet and optics are subject of the following sections. The magnet stands on three legs, which contain air bags for vibrational decoupling. The legs are fixed to an aluminum frame that has its foundations in the concrete floor of the HITRAP platform. A vertical beamline will supply heavy highly charged ions from below for the experiment at a later stage. For better access to the single components, a wooden platform has been built around the magnet tower. Figure 4.5 shows a picture of the magnet when the wooden platform had not yet been completed.

4.1 The Cryocooler

The vacuum chamber and cryogenic electronics are cooled by a SRP-082B two-stage pulse tube cooler from SHI Cryogenics Group (Sumitomo) [SHI08b], which is operated together with an F-70H compressor. The cold-head is depicted in figure 4.6. The first stage is designed for a temperature

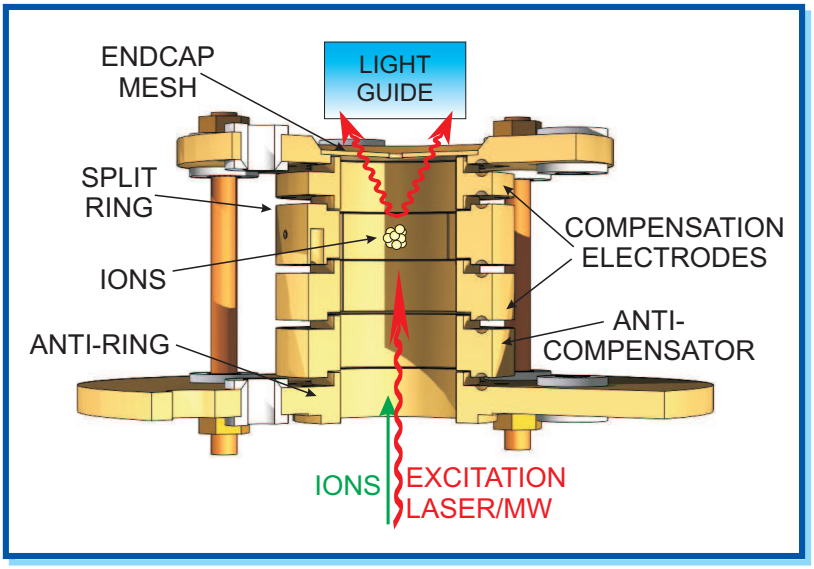

Figure 4.3: Drawing of the spectroscopy trap with a schematic view of ions and photons. (Courtesy of N. Brantjes and M. Vogel)

Table 4.1: Dimensions [mm] and weight [kg] of the cryocooler components.

Instance	Height	Width	Length	Weight
Cold-head	581	190	347	26
Compressor	576	444	529	100

of 45 K at 40 W cooling power, the second stage reaches 4.2 K with 1.0 W heat load. The second stage is connected to the trap vacuum chamber via OFHC copper rods, whereas the first cools a surrounding aluminum radiation shield.

Furthermore, the cooler can reach a minimum temperature of below 3 K and is specified with a cool-down time of less than 80 min, maximum vibrational amplitudes of 7 μm (1^{st} stage) and 9 μm (2^{nd} stage). These small values are possible because there are no moving parts inside the cold-head. Dimensions and weight are listed in table 4.1, the power consumption is 7.2 kW with a tree-phase current supply. The cold-head is made for vertical orientation only.

While this thesis is being written, we are assembling a cryogenic test facility on the HITRAP experimental platform at GSI. At times when the g-factor experiment is shut down, other groups may use the cooler in this framework, which will be finished by the beginning of 2011. A vertical CF200 cross piece with 250 mm length and two CF40 connectors will be mounted to a steel frame and carry the cold-head on a rubber-sealed adapter at a height of roughly 1.5 m. A technical drawing of the cold-head can be found in appendix C.

We also supply the following optional components: The CF40 orifices can be closed with a multi-connector low voltage feedthrough and a single high voltage feedthrough with HV BNC connectors on both sides. An aluminum radiation shield with 146 mm inner diameter and 580 mm

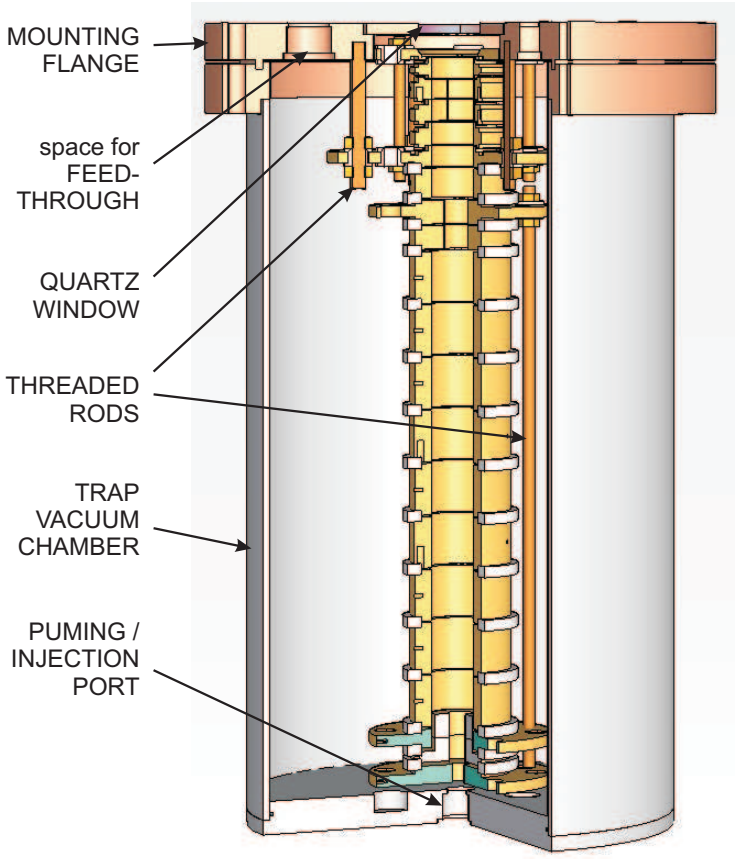

Figure 4.4: Drawing of the copper ultra-high vacuum chamber with the trap assembly. (Courtesy of N. Brantjes)

length will be fixed to the first stage. The vacuum chamber will be completed by a 513 mm long CF200 T-piece and a flange with a central KF16 adapter. The setup can be evacuated via the horizontal CF150 connector of the T-piece.

4.2 The Magnet

We use a Magnex 7 T 160 mm vertical actively shielded ion trap magnet. The field is generated by a current of 240 A flowing through a multi-filamentary NbTi superconductor with a high percentage of copper [Mag09c]. 160 mm refers to the diameter of the 1730 mm long warm bore. Additional shim coils and passive ferromagnetic elements ensure the homogeneity over the trapping region as well as the shielding to the outside. The coils are immersed in a liquid helium bath, which is pre-cooled by liquid nitrogen.

The acceptance document [Mag09b] states a central field strength of 7.003 T, short term persistence of 0.19 ppm/h, an inhomogeneity of 0.14 ppm over a 1 cm^3 cubic volume as well as 8.71 ppm over a cylindrical volume of 10 cm length and 0.5 cm diameter. We have been observing the cryogen boil off rates since the magnet has been energized in 2009. The liquid nitrogen consumption is around 0.25 l/h and we refill the volume of 180 l every 14 days. The dewar for liquid helium

Figure 4.5: The magnet cryostat on the aluminum frame.

has a capacity of 600 l with 300 l above the superconducting joints. The 42 cm^3/h boil off rate translates to a hold time of 300 days.

The delivering company Magnex supplied a polar plot of the stray field (figure 4.7 left) as well as a theoretical curve of the field on axis (figure 4.8(d)). I undertook additional measurements with respect to safety and ion optical issues, since a magnetic field B deflects the trajectory of charged particles. The radius of curvature r can be calculated with the (non-relativistic) velocity v and the charge-to-mass ratio Q/M. Typical values at HITRAP are an acceleration voltage of 6 kV and $\frac{1}{3}\frac{e}{u}$, which leads to a magnetic rigidity $Br = Mv/Q \approx 0.02$ Tm. The terrestrial magnetic field of $B_E \approx 0.3$ G $= 30\ \mu$T causes a 670 m cyclotron radius, which will be compensated. Any other field—stronger or in a different direction—should be considered as well.

The stray field as indicated by Magnex quickly drops down to 5 G outside the bore. The field center is at 4 m height above the HITRAP platform. The right part of figure 4.7 shows an overview of the platform. The g-factor magnet is surrounded by the wooden tower in the upper

Figure 4.6: Image of the Sumitomo cold-head taken from [SHI08b].

middle. The field center is marked red as well as the (not yet constructed) beamlines and the end point of the HITRAP facility, the multi-passage spectrometer (MPS, to the right). This is the starting point of the beamline to the experiments: First the g-factor experiment above the line, then SPECTRAP to the lower left. The MPS serves as reference for figure 4.8(a).

The field along the main beamline (fig. 4.8(a)) increases towards about 1 G directly below the g-factor magnet, situated ca. 4 m away from the MPS. It is little stronger than the terrestrial magnetic field. On the beamline to the SPECTRAP experiment (fig. 4.8(b)), the field decreases back to the minimum value of 0.3 G, indicating that the component caused by the magnet is at least $0,6$ G. The distance refers to the SPECTRAP magnet axis and is oriented towards the main beamline.

Only directly below the g-factor experiment and only at sufficient height the magnetic field exceeds the terrestrial value significantly (fig. 4.8(c)). Still the strength of 3.5 G at 2 m height is well below the strictest threshold of 7 G (0.7 mT) for pacemakers in static magnetic fields. The area of increased exposition (1.27 kG, max. 2 hours per day) ends 20 cm below the base flange of the magnet. More information about radiation protection can be found in [UWS02].

The values measured along the beamline up to the magnet are depicted in figure 4.8(d). They agree fairly well with the data calculated by Magnex, which are listed in [Mag09a].

4.3 The Optical Components

In section 3.1, I have mentioned some details about the spectroscopy scheme. Laser radiation has to be coupled into the vacuum chamber, and a high fraction of the fluorescence light needs to be collected and guided to a detector.

The ion cloud has a diameter of roughly 1 mm and is 18 mm away from the vacuum window. So it can be regarded as a small light source, which is suitable for optical imaging to a light guide and detector with limited sizes. The window has a diameter as big as 18 mm to satisfy the demand

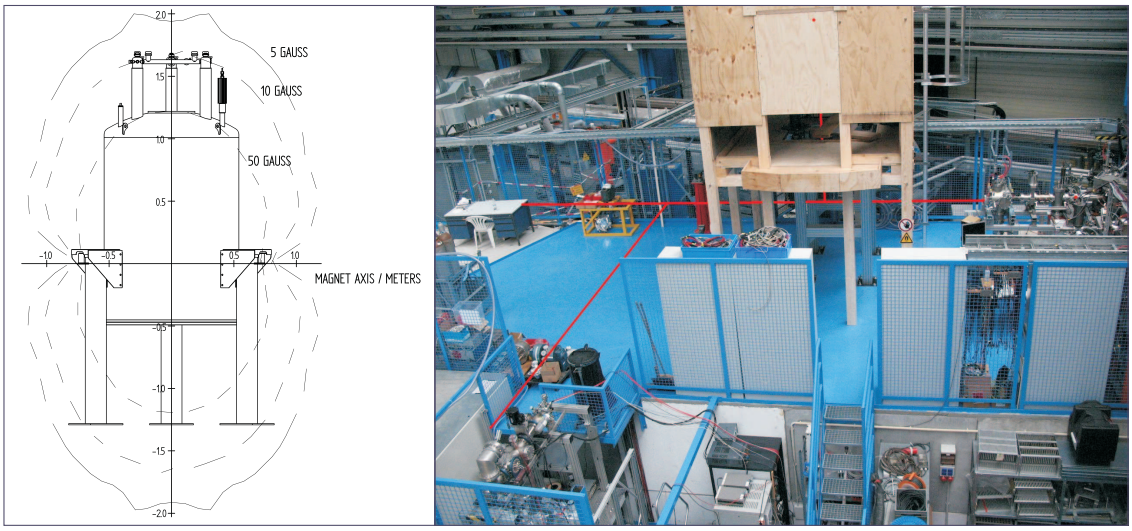

Figure 4.7: Polar field plot [Mag08] and HITRAP platform with beamline and important points, marked in red.

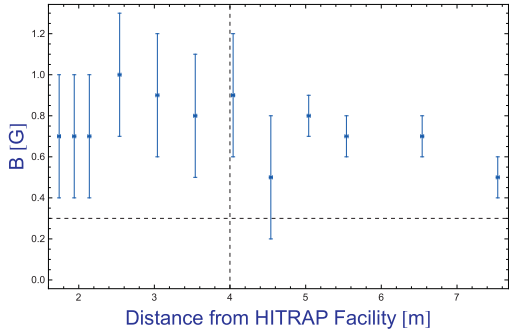

(a) Along the HITRAP main beamline. The magnet axis is marked with the vertical dashed line at 4 m.

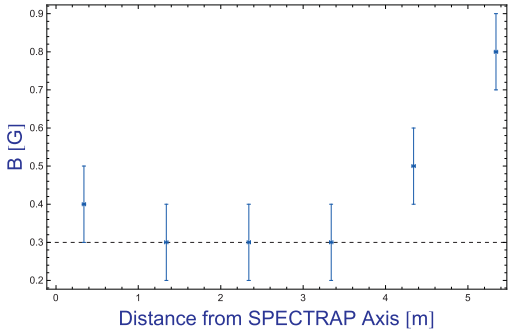

(b) Along the SPECTRAP beamline.

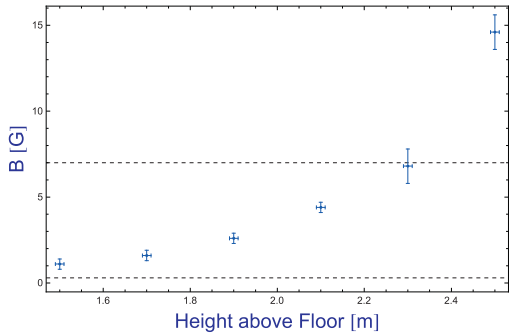

(c) Below the g-factor magnet.

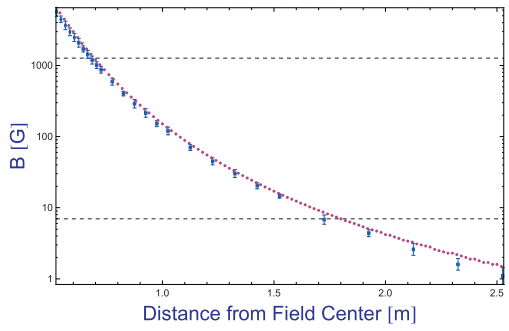

(d) Along the g-factor beamline. Values calculated by Magnex (red) and measured at GSI (blue).

Figure 4.8: Plots of the magnetic field strength, measured at selected places on the HITRAP platform, as each caption explains. Horizontal dashed lines indicate the terrestrial magnetic field and two safety thresholds as mentioned in the text.

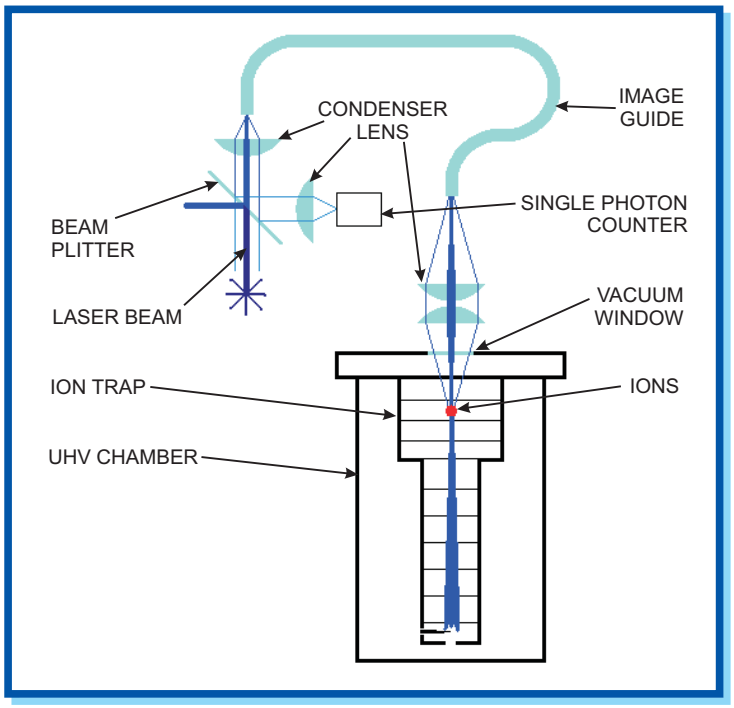

Figure 4.9: Schematic drawing of the imaging principle.

for a large solid angle. We will use a pair of aspherically corrected condenser lenses (THORLABS ACL4532-A), which are made for high image quality even at a large aperture. One of them is installed next to the window, the other one focuses the light to a spot above the lens pair. Figure 4.9 shows a sketch of the assembly. At this spot we will place one end tip—the cold end—of a multi-fiber image guide. The SCHOTT Wound Fiber Bundle IG-154-72 has a 4 mm × 4 mm active area with 50 light points per millimeter. These fibers do not conserve the polarization. The numerical aperture of 0.63 matches the lens aperture quite well. We chose a length of 1830 mm for the bundle to conduct the light out of the magnet bore. We ordered a version with very thin Teflon sheathing to reduce the minimum bend radius to 25 mm. Teflon end tips are compatible with the magnetic field. The light is coupled out at the warm end tip and again collimated and refocused by a pair of condenser lenses. At this end we use the smaller version ACL 2520-A, because there is no need for the large diameter as at the cold end. The focus will be on the active area of a single photon detector—a PerkinElmer Channel Photomultiplier, which has been mentioned in section 3.1, would be an option.

The laser radiation for excitation of the ions must illuminate the same spot that is viewed by the detector. Therefore, it can use the same light path. This is implemented by a beam splitter plate (Edmund NT46-609). This beam splitter can be aligned in a housing with four C-mount ports. I designed mounting adapters for three of these ports: The first holds the warm end of the image conduit at a well-defined position with respect to the beam splitter; the second does the same to the detector. Both include an adjustable support for the coupling lens. The third port is connected to a laser fiber coupler (THORLABS PAF-X-11-A) that comes with a collimating lens itself. The fourth port is closed with a beam dump. The components on the warm side can be

adjusted during operation.

A similar housing mount has been constructed for the lenses and end tip in the magnet bore. It conserves the relative alignment of these instances with each other and with the ion cloud. However, this is not accessible for adjustments when it is installed. We have to move the lenses to a theoretical position, initially. Fluorescent trapped ions will be used to give a feedback of the alignment: Their position in the trap can be manipulated until they match the focus. A good adjustment will be found after some iterations of cooling down, looking for the focal point, warming up and shifting the lens.

At some point, the image guide needs to be fed through a vacuum flange. It must be sealed up, such as to limit the gas load to the evacuated magnet bore. An optical faceplate will be bonded to the end tip, the tip will be screwed and bonded to its adapter mount, and this mount will be screwed to a vacuum flange with a rubber seal squeezed in between.

Chapter 5

Trap Design

In chapter 3 we have assumed that ions are trapped in a perfectly harmonic potential[1]. This chapter points out why this is of importance for a precision measurement. The subsequent sections deal with the approximation of a harmonic potential by an imperfect trap and relate this to experimental requirements.

5.1 Ideal and Real Penning Traps

The electrostatic field of an ideal Penning trap (eqn. 3.4) is derived from the potential

$$\Phi(\rho, z) = \frac{U_0}{4d^2}(\rho^2 - 2z^2). \tag{5.1}$$

For positive ions, this implies an attractive harmonic potential $V(z) = \frac{1}{2}M\omega_z^2 z^2$ along the z-axis with the angular frequency from equation 3.6. $\rho = \sqrt{x^2 + y^2}$ and z are cylindrical coordinates. U_0 and d can be seen as arbitrary parameters; they originate from the use of traps with hyperbolic electrodes as shown in figure 5.1 left.

The end caps (double-leaf hyperboloid) have a minimum distance z_0 from the trap center and are grounded. The ring electrode (single-leaf hyperboloid with minimum radius ρ_0) is biased with U_0, where U_0 is negative for positive ions. This geometry generates a quadrupole potential, because the metal surfaces follow corresponding equipotential lines. The potential coincides with eqn. 5.1 (except for a constant term), if d is chosen according to the definition of the characteristic distance of the trap, $\frac{1}{2}\sqrt{{\rho_0}^2 + 2{z_0}^2}$.

Only in a harmonic potential, the axial frequency is independent of the energy. For instance, in a potential with a fourth-order perturbation,

$$V(z) = c_2 \left(\frac{z}{d}\right)^2 + c_4 \left(\frac{z}{d}\right)^4,$$

[1]The notions of an electrostatic potential Φ and a potential energy $V = Q \cdot \Phi$ are both referred to as 'potential'. As long as we deal with positive charges Q, the distinction has in principle no meaning. However, the first has as negative derivative of an electric field, whereas the second is connected with a force.

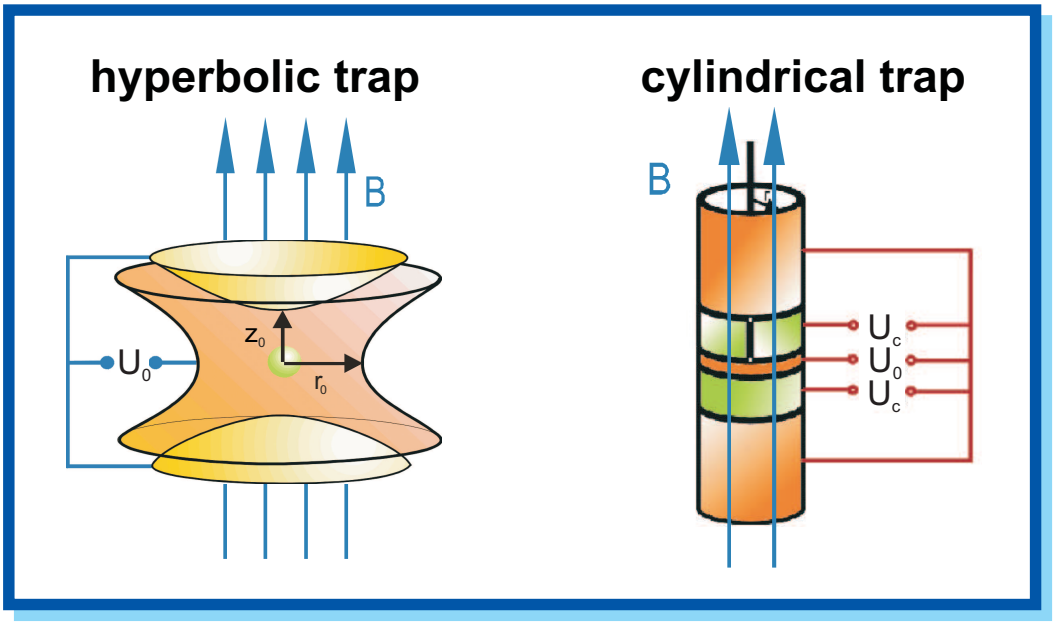

Figure 5.1: With hyperbolic electrodes (left), the ideal potential can be approximated very well. Open end tube cylindrical Penning traps (right) need sophisticated compensation. (Courtesy of S. Stahl and M. Vogel)

the finite axial energy E_z causes a relative frequency shift [GHR89, VQN10] by

$$\frac{\Delta\omega_z}{\omega_z} = \frac{3c_4}{2c_2}\frac{E_z}{M\omega_z^2 d^2} \tag{5.2}$$

A sixth-order perturbation $c_6(z/d)^6$ can be treated with an effective fourth-order term

$$\tilde{c}_4 = c_4 + \frac{5}{4}c_6\frac{E_z}{M\omega_z^2 d^2} \tag{5.3}$$

instead of c_4 [GHR89]. We will come back to this later. Since the motional frequencies are used to determine the magnetic field, harmonicity of the trapping potential is of great value. The reduced cyclotron and the magnetron frequency can also be shifted in an imperfect trap. In general, all frequencies can depend on the energies in each mode, if the electric field is not quadrupolar or the magnetic field is not homogeneous. A strong homogeneous magnetic field is generated by the superconducting magnet introduced in section 4.2. The harmonic potential comes naturally in a trap with hyperbolic geometry as mentioned above. Still cylindrical electrodes can be handled much easier and under certain conditions approach the ideal potential as well [GM84, GHR89]. For this purpose, additional electrodes are introduced next to the ring to compensate for the modified shape. Careful selection of trap parameters minimizes anharmonicities.

The precision trap stands in a context with the trap for ion capture or production, from which the particles are loaded. Therefore it has to be open at least on one side. The use of electrical compensation in a cylindrical Penning trap (by one additional pair of electrodes) leaves two choices, open or closed. There are several traps with end tubes on both sides [GHR89, Sta98,

Ota07, VAB$^+$08, HBH$^+$00], which can be seen in figure 5.1 right. This open geometry provides the required access for ions and is again symmetric. A drawback is related to the fluorescence light emitted in the electronic transition of interest: The light has an angular distribution given by

$$I(\theta)\mathrm{d}\theta \propto (1+\cos^2\theta)\mathrm{d}\theta, \tag{5.4}$$

where θ is the spherical polar angle (see appendix A). This directional characteristic prefers emission along the axis of the magnetic field. The end tubes of open cylindrical traps need to be very long, which leaves only a small solid angle. On the contrary, we can replace the upper end cap of a closed trap by a transparent mesh—more information about this is given in section 5.5—and use the relatively high solid angle of 1.77 sr (which is 14 % of the full sphere, anticipating the results of this chapter) for detection. The fraction of intensity arriving at each end cap is even 18.6 % of the total emitted emitted intensity. Therefore, we choose the principle of a closed trap, but we replace the lower end cap by further correction electrodes. This is explained after the section about the closed trap.

5.2 The Closed Trap

The closed compensated cylindrical Penning trap consists of a ring electrode and two end caps, similar to the hyperbolic trap. Again, the voltage U_0 is applied to the ring, whereas the end caps are grounded. Different from the hyperbolic geometry, the ring is now a hollow cylinder with a radius of ρ_0 and length z_r, and the end caps are flat, having a distance of z_0 from the trap center. Two correction electrodes (or compensators, used synonymously) next to the ring have the length z_c and are set to the voltage U_c. In order to avoid short circuits, sparks and parasitic capacitance, the electrodes are separated by sapphire rings. The inner surface therefore has gaps of the width z_g. A similar electrode stack can be seen in figure 5.2. It has been further modified according to the discussion in the following sections.

The electrostatic potential in the trap volume is a linear superposition of the potentials which are created by the single electrodes:

$$\Phi(\rho,z) = \sum_i U_i \phi^{(i)}(\rho,z). \tag{5.5}$$

The functions $\phi^{(i)}$ are solutions of the Laplace equation with the boundary conditions $\phi^{(i)} = 1$ at the active electrode i and $\phi^{(i)} = 0$ at all other electrodes. To complete the conditions, we assume a linear slope in the gaps between active electrode and its neighbors, thus forming a trapezoid function. A solution to the Laplace equation can be written as a linear combination of the basis functions

$$b_n(\rho,z) = \frac{J_0\left(\frac{n\pi\rho}{z_t}\right)}{J_0\left(\frac{n\pi\rho_0}{z_t}\right)} \sin\left(\frac{n\pi z}{z_t}\right),$$

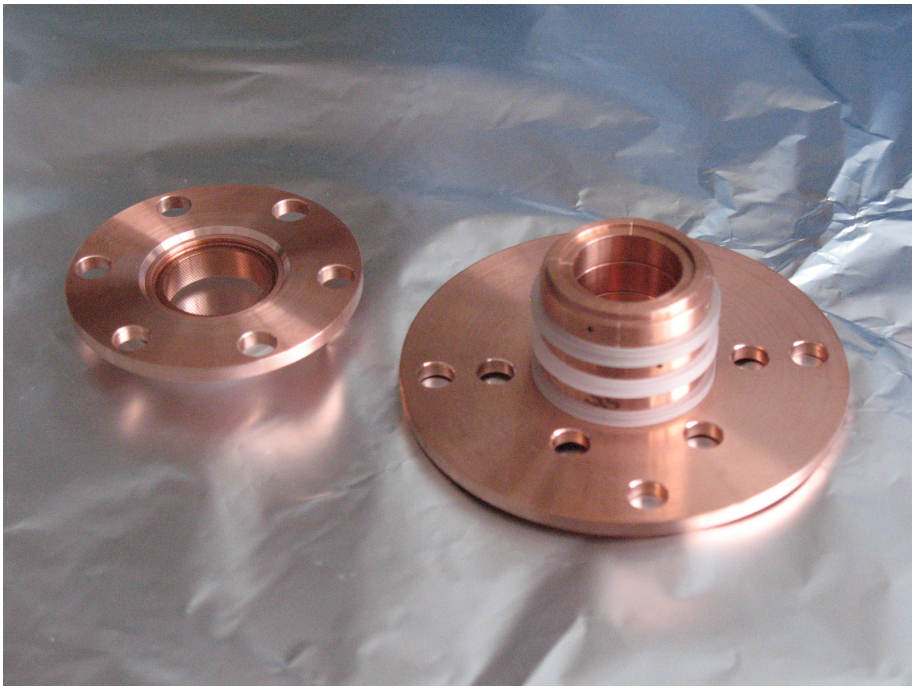

Figure 5.2: The spectroscopy trap before gold-plating.

if it is rotation-invariant and zero at the end points $z = 0$ and $z = z_t$ [GM84]. We normalized the Bessel function J_0 to one at the lateral area of the hollow cylinder ($\rho = \rho_0$). On this surface, the linear combination $\phi^{(i)} = \sum_n a_n^{(i)} b_n$ can be evaluated,

$$\phi^{(i)}(\rho_0, z) = \sum_n a_n^{(i)} \sin\left(\frac{n\pi z}{z_t}\right), \tag{5.6}$$

keeping in mind that these values are specified by the boundary conditions. At the same time, the expression 5.6 has the form of a Fourier sum. For an electrode between $z = a$ and $z = b$ at unit voltage, we obtain the Fourier coefficients by an integration:

$$\begin{aligned} a_n^{(a,b)} &= \frac{2}{z_t} \int_0^{z_t} \mathrm{d}z \; \phi^{(a,b)}(\rho_0, z) \; \sin\left(\frac{n\pi z}{z_t}\right) \\ &= \frac{4}{n\pi} \left(\cos\left(\frac{n\pi a}{z_t}\right) - \cos\left(\frac{n\pi b}{z_t}\right)\right) \sin\left(\frac{n\pi z_g}{z_t}\right) \frac{z_t}{n\pi z_g}. \end{aligned} \tag{5.7}$$

Now we specialize these results to the closed trap with three active electrodes. The trap length is $z_t = 2z_0$, the coordinates of the ring and compensators are applied accordingly. The contributions of the correction electrodes are summarized to one function $\phi^{(c)}$. In order to analyze the anharmonicity, we expand the potential in a power series around the trap center

$$\Phi(0, z) = \sum_{j \text{ even}} C_j \left(\frac{z - z_0}{d}\right)^j. \tag{5.8}$$

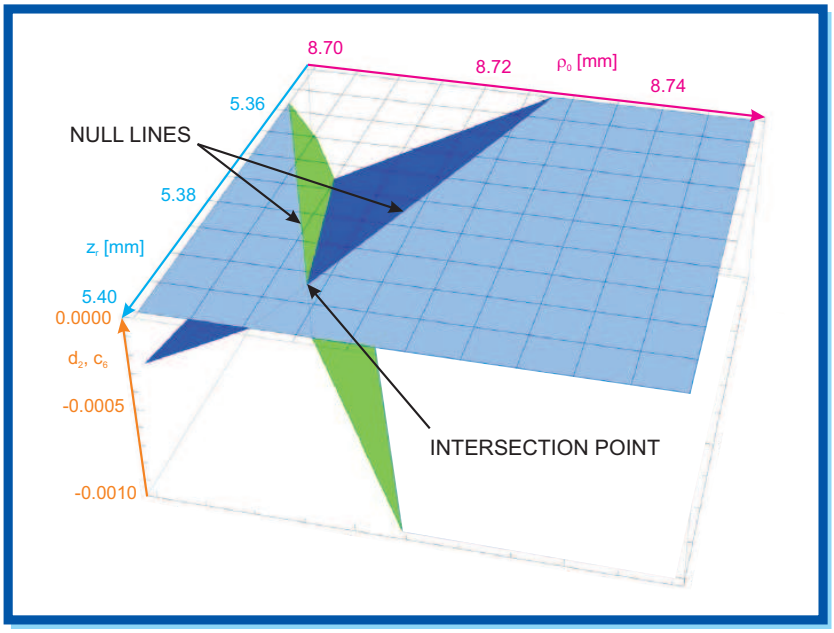

Figure 5.3: c_6 (dark blue) and d_2 (green) as functions of the ring length and radius. We determine the coordinates of the intersection point, $z_r = 5.392$ and $\rho_0 = 8.713$.

There are only even terms, because $z = z_0$ defines a symmetry plane of the trap. Following the idea of equation 5.5, we decompose the C_j coefficients into the contributions of the ring electrode and the compensators, $C_j = U_0 e_j + U_c d_j$. Defining the tuning ratio $T = U_c/U_0$, we can write $C_j = U_0(e_j + T d_j) = U_0 c_j$. Here, e_j and d_j are the Taylor coefficients of the sine function times the respective Fourier coefficients of the particular electrodes, calculated in equation 5.7. They only depend on the trap dimensions. We search for a geometry where all higher orders than the second in the expansion 5.8 vanish. This results in an over-determined non-linear system of equations for the variables T, z_0, z_r, z_g, ρ_0. The compensator length follows from the other dimensions.

The gap width is constrained by electrical requirements and apart from that, the electrostatic problem is invariant with respect to rescaling the entire trap. For this reason we leave the gap width and at this point also the trap length untouched and restrict ourselves to three free parameters: The tuning ratio, the ring length, and the radius. The optimal tuning ratio is determined by the requirement of a vanishing lowest-order anharmonicity, $T = -e_4/d_4$. In the experiment, when the geometry is fixed, the electrical tuning is the only way to compensate for the anharmonicity. Therefore, the trap should be orthogonal, which means that the ion oscillation frequency is independent of the tuning, or equivalently $d_2 = 0$.

This condition and the sixth order of the Taylor expansion are used to find the ring length and radius with a graphical method: We plot d_2 and c_6 as functions of z_r and ρ_0, where c_6 is evaluated with the optimal tuning ratio—see figure 5.3. Both functions have null lines in the three-dimensional plot. The lines intersect in the point $(z_r, \rho_0)_{d_2 = c_6 = 0}$. This defines the optimal geometry, where the 2 lowest-order perturbations can be tuned out (compensated) simultaneously without affecting the axial frequency (orthogonal trap). The results are summarized in table 5.1.

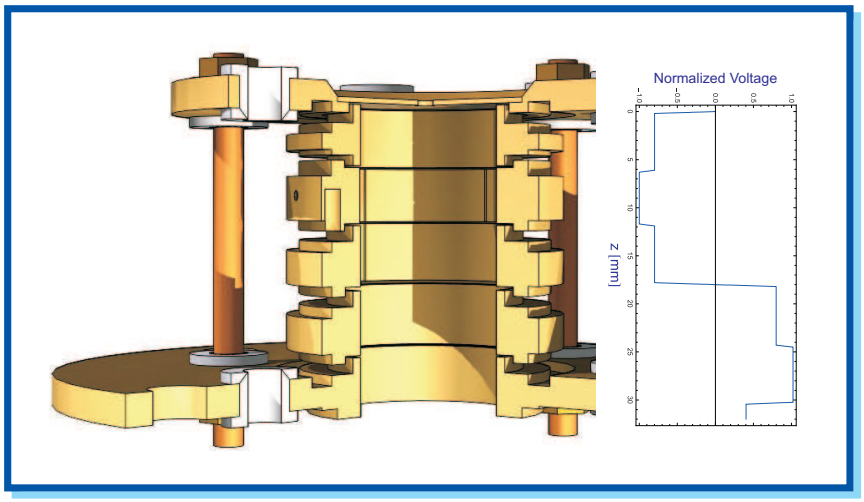

Figure 5.4: Voltage definitions at the electrodes of the spectroscopy trap. (Drawing: Courtesy of N. Brantjes)

5.3 The Half-Open Trap

As I pointed out before, we cannot use the closed trap which has been designed with two end caps in the previous section. Nevertheless, we use a geometry that approximates the potential calculated there: Additional electrodes mimic the effect of the missing end cap. The idea behind this is to build a mirror image of the closed trap, biased with the opposite voltages—the 'antitrap'. Then, for symmetry reasons the potential will be zero in the plane of the virtual end cap. The strict application of this idea would again lead to a closed trap. However, at some distance, further modifications are tolerable, because their effect on the trap center is shielded by the electrodes in between.

So we take over the geometry of the closed trap with all voltages. Then, we remove the lower end cap and install an anticompensator, antiring and some more electrodes, referred to as 'rest'. This rest is assumed with a uniform voltage in order to keep the number of degrees of freedom reasonable. For other purposes, such as ion transport, these electrodes may be differentiated. The whole assembly is modeled with the length $z_t = 8z_0$, an arbitrary choice. The anticompensator is set to the negative voltage of the compensator, whereas the voltages T_1U_0 of the antiring and T_2U_0 of the rest are still to be determined by a model fit. Another two free parameters are found in the anticompensator and antiring length, z_{ac} and z_{ar}, resp. Between the electrodes, we keep the same gap width as in the closed trap, with one exception: The gap between the lower correction electrode and the anticompensator is doubled, in order to keep the virtual end cap in the original place. Figure 5.4 shows the boundary conditions (namely the potential values at $\rho = \rho_0$) and a drawing of the geometry.

As we did for the closed trap, we determine the contribution $\phi^{(i)}(\rho, z)$ of each electrode in the new arrangement. According to formula 5.5, the trapping potential $\Phi(\rho, z)$ is again made up as a linear combination of these functions, multiplied with the respective voltages U_i, which are defined in the previous paragraph. The resulting function is evaluated in the plane of the virtual end cap, $z = 2z_0$. This is a function of one variable, the radius, with four fit parameters. Then,

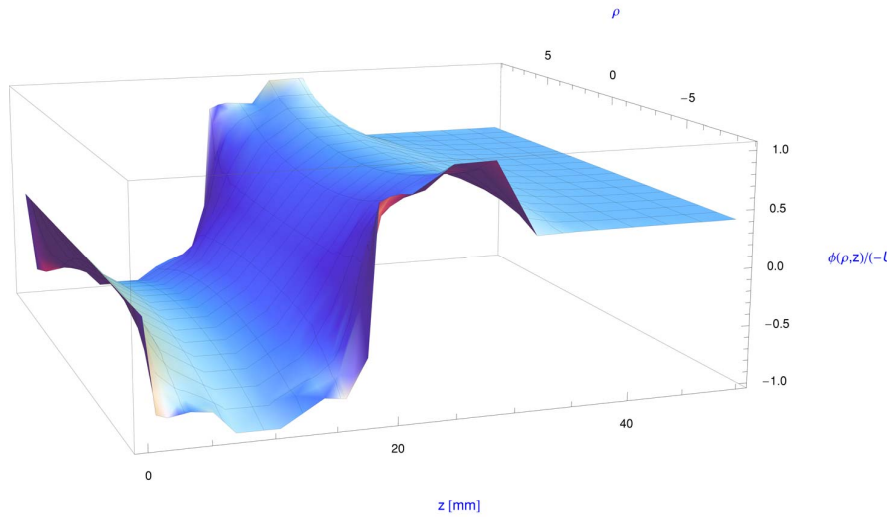

Figure 5.5: The potential is 'spanned' between the electrodes like a thin film.

Table 5.1: Results of the semi-analytical calculations for the closed trap and of the fit method for the asymmetric trap. Lengths and radius in mm, tunings are dimensionless.

z_0	z_r	ρ_0	z_c	T	z_g	z_{ac}	z_{ar}	T_1	T_2
9.000	5.392	8.713	5.904	0.799404	0.200	6.200	5.740	-1.02071	-0.402493

ten equidistant points ($\rho/\rho_0 = 0, 1, 2, ..., 9$) in the plane are chosen for an artificial data set to have the value zero. A fit routine finds the best values for the model parameters to describe the artificial data. This makes the potential in the relevant plane as close to zero as possible. In figure 5.5 the resulting potential is depicted.

Despite all efforts to find the optimum geometry, the potential will not be perfect. The inevitable asymmetry introduces odd terms in the Taylor expansion 5.8, which shift the trap center. Furthermore it is unrealistic to expect that the electrodes are machined with higher accuracy than a micrometer. To account for this, we round the calculated dimensions and fix them to values listed in table 5.1. With these definitions we can find an estimation for realistic expansion coefficients (tab. 5.2). Now we can evaluate the perturbative expressions for the shift of the axial frequency (only 4^{th} and 6^{th} order: equations 5.2 and 5.3) and obtain $\Delta\omega_z/\omega_z \approx 8.0 \cdot 10^{-10}$ for Ar^{13+} ions with an energy corresponding to 60 K in the axial vibration mode, if the ring voltage is -10 V.

Table 5.2: Coefficients for the Taylor expansion 5.8 of the potential in the half-open trap.

c_1	c_2	c_3	c_4	c_5	c_6
$-1.6 \cdot 10^{-5}$	-0.522644	$-1.8 \cdot 10^{-5}$	$-1.4 \cdot 10^{-5}$	$-1.1 \cdot 10^{-5}$	$-1.8 \cdot 10^{-5}$

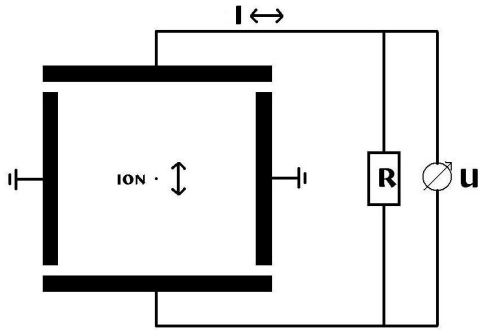

Figure 5.6: An ion moves between two electrodes and causes image current. Energy is dissipated in the resistor and a voltage drop can be detected.

After the rounding, the trap is also no longer orthogonal, which is quantified by $d_2 = 4.5 \cdot 10^{-5}$. This has the effect that the axial frequency is shifted with the correction voltage according to $\partial\omega_z/\partial U_c \approx 2\pi \cdot 1.6$ Hz/V. Keeping in mind that the frequency itself is around $2\pi \cdot 0.37$ MHz and that the correction voltage is stable in the sub-mV range, this translates to a ppb effect.

Further sources of imperfection are patch effects: Traces of different materials on the electrode surfaces cause a non-uniform voltage. Insulators can even build up charged areas. For this reason, the electrodes are gold plated in galvanic baths: first a silver diffusion barrier of 20 μm thickness and then a gold layer of less than a micrometer are deposited on the electrodes. The noble metals prevent the electrodes from corrosion. However, the galvanic process prefers sharp corners and grows thicker layers there. The effect of 50 μm relief structure must not be underestimated, as a detailed numerical analysis of a different geometry shows [Lin08]. The different thermal contractions of copper and sapphire during the cool-down from room temperature to 4 K are also discussed there. This effect can be compensated, if the designed dimensions for the sapphire parts are rescaled by a factor of 0.9973.

5.4 Ion Detection and Absolute Size of the Trap

The electronic detection of ions in a Penning trap uses the principle of image charges [WVST06]. Moving ions induce an image current in the electrodes which leads to a voltage drop in a resistor, as shown in fig. 5.6. The power that is dissipated in the resistor at the same time cools the ions.

An ion with charge Q shall move with the velocity $\dot{z}$ between two infinite planes at distance D (a capacitor, perpendicular to the z-axis). This ion would induce the current

$$I = Q\frac{\dot{z}}{D}$$

in the planes. Vice versa, such planes would cause an electric field

$$\begin{aligned} \vec{\mathcal{E}} &= \frac{U}{D}\vec{e}_z \\ \Rightarrow D &= \frac{U}{\vec{\mathcal{E}} \cdot \vec{e}_z}, \end{aligned} \tag{5.9}$$

Table 5.3: Effective distances for ion detection. The first column gives the electrode from which the signal is gripped, the second says which motion is detected: The cyclotron motion takes place perpendicular to the z-axis. Then the effective distances in mm are listed for an earlier and the final version of the trap.

Electrode	Motion	D_{old}	D_{new}
Upper end cap	Axial	49	29
Upper compensator	Axial	54	32
Split ring	Cyclotron	52	31

if a potential difference U was applied to them. Real electrodes are described by an 'effective distance' D [Sta98] which is defined according to equation 5.9, following the idea of a symmetric coupling strength between the ion and the trap wiring. If two different assemblies have the same effect on an ion, then also the ion must influence both equally.

For our geometry considerations, the following point is of particular interest: Both detection and cooling efficiency are inversely proportional to the square of the distance, and D obviously scales with the trap dimensions. We have calculated effective distances of several electrodes for an earlier version of the trap (see tab. 5.3) and decided to scale the whole trap down from 30mm to 18mm trap length ($2z_0$) in order to increase every efficiency by a factor of 25/9.

The table mentions a split ring for the detection of the cyclotron motion. Split electrodes can also be seen in all figures showing the real trap, for instance 4.2, 4.3, 5.2 and 5.4. For excitation, cooling or detection of a radial motion, we need an electrode configuration that can create a non-zero radial field component at the trap center. Otherwise the effective distance of any electrode is infinity, as can be seen, if the unit vector in equation 5.9 is replaced by $\vec{e}_x$. Such a field component is impossible in a rotation-symmetric trap. Split electrodes, however, allow for radial manipulations.

5.5 The Spectroscopy Mesh

The spectroscopy mesh (INDUSTRIAL NETTING Micro-Mesh Electroformed Screens BM 0052-01) is made of a copper foil with 5.08 μm thickness. It has a density of 2.07 wires per mm with 96.5 μm width. In contrast to the solid electrodes, the mesh has been plated with a silver layer of only 5 μm and again less than a micrometer of gold. These characteristics correspond to 60% light transmission and an areal mass density of 60 g/m^2.

After the plating, the mesh has been squeezed between the support electrode and a copper ring. Figure 5.7 demonstrates this. The mesh serves as upper end cap of the spectroscopy trap. Therefore, small deformations of this very fine piece of metal would lead to electrostatic potential distortions and corrupt precision. We estimate the gravitational and electrical force—or rather stress—acting on the mesh to be 0.6 Pa and below 7 mPa, respectively. The latter is calculated with the maximum electrical field $\hat{\mathcal{E}} = 40$ kV/m and the analogy of a capacitor: The two plates experience an areal force density of $p_{\mathcal{E}} = \varepsilon_0/2\ |\mathcal{E}|^2$, if there is the electrical field $\mathcal{E}$ between them. However, this contribution is negligible compared to the gravitational effect. And we do not

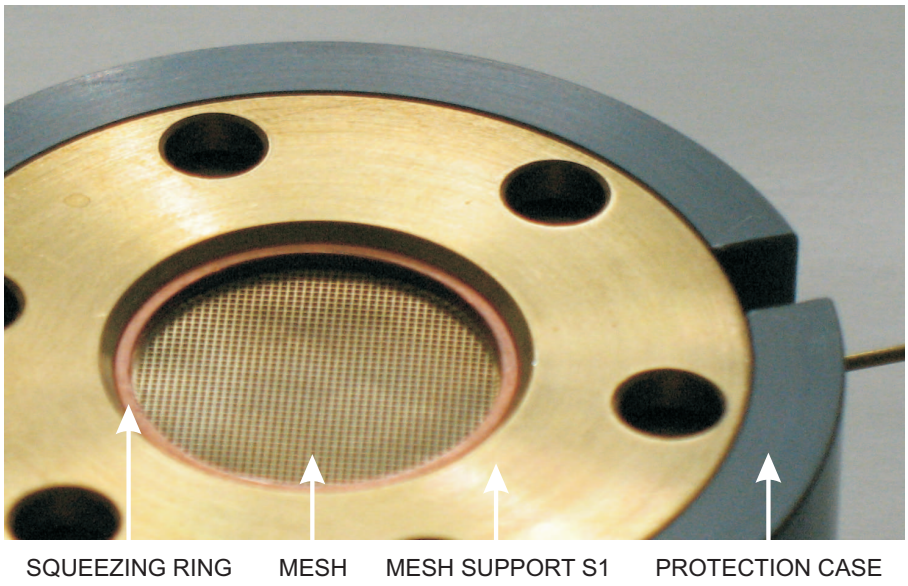

Figure 5.7: The spectroscopy mesh, attached to electrode S1.

observe a deformation of the mesh when the electrode is turned upside down. The deformations visible in figure 5.7 have probably occurred in the galvanic process or when the mesh was fixed to the electrode body. This sets a serious limit to the precision of the trapping potential but it could hardly have been avoided.

Chapter 6

Ion Production

The g-factor experiment is part of the HITRAP project at GSI, which will be an intense source of slow heavy highly charged ions [KBB$^+$08]. The HITRAP facility also comprises a small commercial electron beam ion trap as test ion source. Yet it is of great advantage to have an independent ion source as part of our own setup:

- First tests in order to characterize the experimental components and techniques can be performed with a manifold of ion species.
- Measurements with medium-heavy highly charged ions such as Ar^{13+} form an important contribution to the series of g-factor determinations up to heavy ions. For these purposes we need not rely on expensive beam time or other complications involved with external ion sources.
- The field emission electron source (see chapter 7) with separate energy and current control serves also as a tool for excitation of highly energetic atomic levels. In combination with laser and microwave excitation the trap setup thus becomes a very versatile device for ion spectroscopy.
- Another gain of the electron beam is the sympathetic cooling of ions in a nested trap [Zwi06, NTZ07, Mae08].

This chapter focuses on the production of Ar^{13+} ions from argon gas in the UHV chamber. The first section discusses the principle of electron impact ionization. It is followed by a detailed description of a cryogenic gas valve, which has been developed within the scope of this thesis.

6.1 Electron Impact Ionization

One of several techniques to create ions is electron impact ionization. It has been applied successfully in cryogenic Penning traps to produce medium-heavy highly charged ions [VAD$^+$05]. The underlying process is the removal of one or several electrons with the energy of an incoming electron,

$$e^- + \mathrm{Ar}^{q+} \rightarrow e^- + \mathrm{Ar}^{(q+m)+} + me^-.$$

For simplicity we limit ourselves to the case of single ionization ($m = 1$), which is the dominant process when it comes to higher charge states. This process can take place if the impact energy exceeds the ionization potential I_q of the initial charge state.

The integral production rate $\dot{N}$ of higher charge states depends on the densities of colliding particles and on their physical properties. Let ρ_q and ρ_e be the density of atoms (or ions, q indicating the charge state) and electrons, respectively, and v their relative velocity. σ denotes the cross-section for an arbitrary collision process between atoms and electrons (for ionization see below). Then the event rate for this process is

$$\dot{N} = \int \mathrm{d}V \ \rho_q \rho_e v \sigma.$$

If the reactants have uniform respective velocities, we can define the luminosity L separately, which measures the densities of colliding particles. We also approximate the local densities by constant values in an intersecting volume V and obtain

$$\dot{N} = L_q \sigma, \quad L_q \approx \rho_q \rho_e v V.$$

In the case of atoms, the electron cloud defines the size of the volume V, because it is contained in the atom cloud. In our experimental situation it has a diameter of 0.7 cm, whereas the atoms almost fill a cylinder of 1.75 cm diameter. We are mainly interested in the ionization rate R_0^i for a single atom. For a general reaction (ionization, recombination, loss etc.) we define the rate per ion or atom as

$$R_q \equiv \frac{\dot{N}}{N_q},$$

where N_q is the total number of ions in the charge state q. Then our focus is on the luminosity per atom:

$$L_0/N_0 = \rho_e v \left(\frac{0.7}{1.75}\right)^2 = 0.16 \rho_e v, \tag{6.1}$$

assuming that the cylinders have the same length. If argon is singly ionized, the ions will be trapped and contained within the electron cloud, and their number is equal to $\rho_q V$. Thus, the luminosity per ion is:

$$L_q/N_q = \rho_e v. \tag{6.2}$$

In section 7.4 we estimate the electron density to be roughly 10^9 cm^{-3}. The relative velocity in equations 6.1 and 6.2 is given by the impact energy ϵ and reduced mass μ. These quantities are almost equal to the velocity, kinetic energy and mass $m = 511$ keV/c^2, resp., of the electrons:

$$v = \sqrt{\frac{2\epsilon}{\mu}} = \sqrt{\frac{2\epsilon}{511 \text{ keV}}}\ c,$$

so that equations 6.1 and 6.2 can be evaluated to

$$L_0/N_0 \approx 10^{16}\ \mathrm{cm}^{-2}\mathrm{s}^{-1}\sqrt{\frac{\epsilon}{\mathrm{eV}}} \tag{6.3}$$

$$L_q/N_q \approx 6\cdot 10^{16}\ \mathrm{cm}^{-2}\mathrm{s}^{-1}\sqrt{\frac{\epsilon}{\mathrm{eV}}}. \tag{6.4}$$

The energy-dependent reaction probability is described by the electron-impact ionization cross-section σ_q. There are not many experimental data for the ionization of highly charged ions, but over the last decades several semi-empirical models have been developed to predict such probabilities, see e.g. [Lot67, BRM00]. We will use a general scaling law found by Fisher et al. [FRG$^+$95], approximating cross-sections in the low-energy regime for an arbitrary element, charge state and number of extracted electrons. It holds to within a factor of 2 for all available data, particularly for argon with charge $q \leq 4$ and single or double ionization. They introduce the scaled kinetic energy x of a projectile electron (almost identical to the impact energy),

$$x = \frac{\epsilon}{I_q},$$

and the scaled cross-section

$$\tilde{\sigma}_q = \frac{\sigma_q}{S_q}.$$

The scaling factor

$$S_q = \pi {a_0}^2 \left(\frac{I_\mathrm{H}}{I_q}\right)^2 \zeta_q \approx 0.78 \left(\frac{\alpha\hbar c}{I_q}\right)^2 \zeta_q$$

contains only fundamental constants, the ionization potential and the number ζ_q of electrons in the outermost shell. The scaling law states that for a sufficiently low energy $1 \leq x \leq x_q^i$ the scaled cross-section follows the universal curve

$$\tilde{\sigma}_q \approx \tilde{\sigma}_u = 4\frac{\ln x}{x^{1.4}}\left(1 - 2e^{-0.7x}\right).$$

This means that the energy dependence of electron-impact ionization probability can be roughly described by the curve depicted in figure 6.1 for all elements and charge states.

The ionization rate $R_q^i \approx L_q/N_q \cdot \tilde{\sigma}_u \propto \sqrt{x}\cdot\tilde{\sigma}_u$ reaches a maximum for energies of a few times the ionization potential—according to the approximation at $\epsilon = 4.7 I_q$. For most efficient charge breeding, the impact energy should be increased simultaneously with the most abundant charge state in order to abide in this maximum. Table 6.1 summarizes some important values for the case of argon.

The last column of table 6.1 however reflects the following idea: Ar^{13+} can be produced most quickly, when the energy is raised up to 3.3 kV during the process. Still, at this energy also the step from Ar^{13+} to Ar^{14+} is achieved at a relatively high rate, limiting the fraction of the desired species. If instead one uses electrons between the respective production thresholds (i.e. the 13^{th}

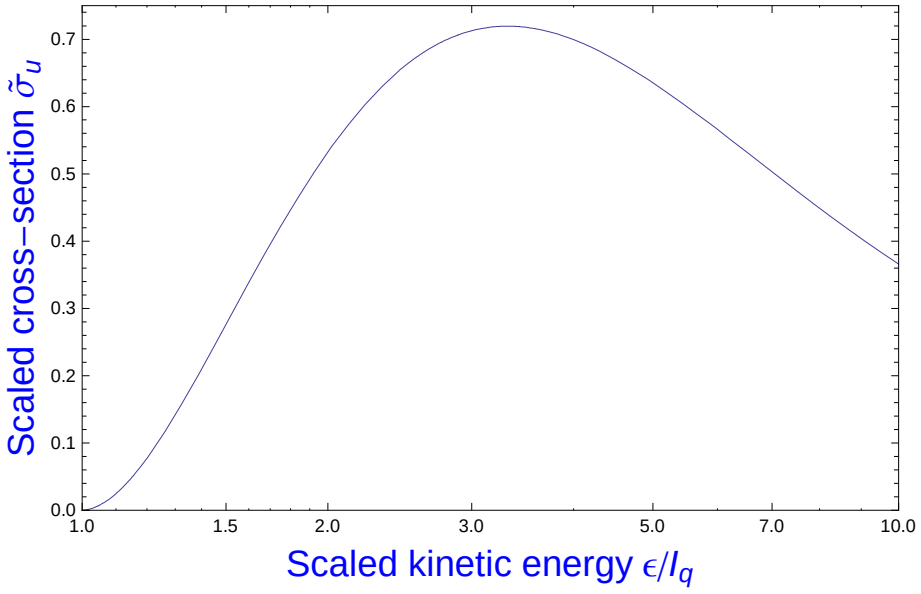

Figure 6.1: The universal approximation for the energy-dependent electron-impact ionization cross-section as found empirically by Fisher et al. [FRG+95].

Table 6.1: Initial charge state, ionization potential, energy to maximize the ionization rate, corresponding cross-section, maximal ionization rate and ionization rate if the voltage is kept at 750 V.

q	I_q [eV]	ϵ [eV]	σ_q [10^{-18} cm^2]	$R^i_{\max}$ [Hz]	$R^i_{750\text{ eV}}$ [Hz]
0	15.8	74.8	342	28.1	9.44
1	27.6	131	97.4	66.2	31.5
2	40.7	193	38.4	31.7	18.9
3	59.7	283	14.9	14.9	10.9
4	75.1	357	7.53	8.44	6.87
5	91	432	3.85	4.75	4.19
6	124	590	1.37	1.98	1.93
7	143	681	0.516	0.8	0.796
8	423	2.01 k	0.476	1.27	0.515
9	480	2.28 k	0.323	0.915	0.254
10	540	2.56 k	0.219	0.657	0.11
11	619	2.94 k	0.139	0.446	0.0292
12	686	3.26 k	0.0903	0.306	0.00494
13	755	3.59 k	0.0559	0.199	0

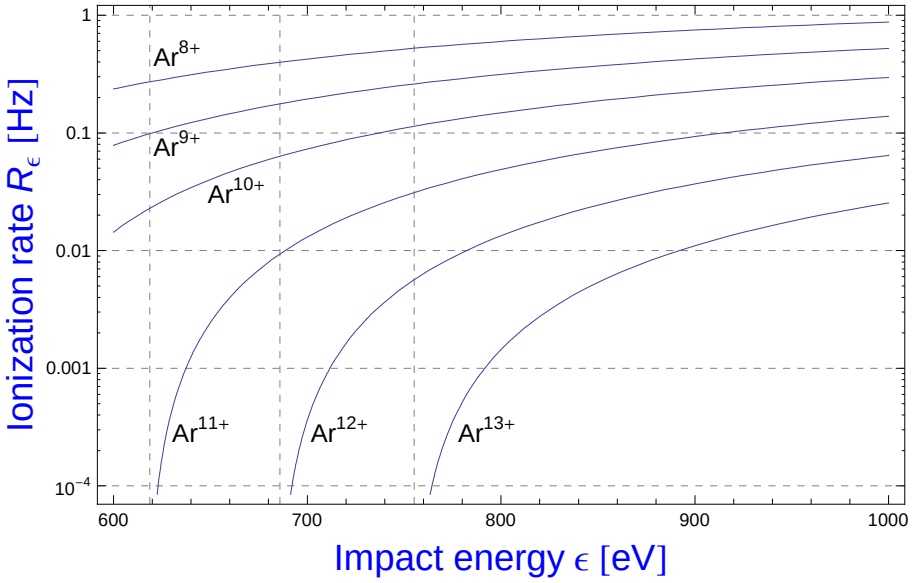

Figure 6.2: Ionization rates for argon charge states from 8 through 13 as a function of the impact energy. The vertical dashed lines mark the 12^{th}, 13^{th} and 14^{th} ionization potential.

and 14^{th} ionization potential $I_{12} = 685.9\,\text{eV}$ and $I_{13} = 755.2\,\text{eV}$, resp.), Ar^{13+} breeding takes several minutes, but it will not be further ionized. Figure 6.2 depicts the ionization rates for various species at different energies.

Still the results have to be treated carefully, since no model has been precisely tested for high charge states. In particular, the Fisher scaling law has only been checked for $q \leq 4$ (concerning argon) and the critical scaled energy x_q^i is often below 2 and thus also below the value for maximum cross-section ($x = 3.32$). Furthermore, we have neglected competing processes, such as radiative and dielectronic recombination (RR, DR) with electrons as well as charge exchange (CE) with neutral atoms—argon or any residual gas. Ions can reduce their charge state by these mechanisms. If instead a particle is heated up to an energy higher than the trap depth, it will be lost. This is most important for neutral atoms, since they are not trapped by the electromagnetic field. Ions are not affected by this, because of the magnetic field and the attraction to the electron beam: A textbook calculation shows that in the present case, the space charge of the electron beam causes a voltage difference of 30 V between the axis and the electrode surface at a radius of 1.75 cm. This excludes radial ion loss due to collisions with a 750 eV electron beam (energies are distributed according to the inverse mass in thermal equilibrium).

All these processes are described by a set of coupled linear differential equations, the solution of which gives some more accurate results than the simple estimation presented here. Several simulation programs such as CBSIM [BKS06] and DITHER are widely used in the EBIS/T community and are capable of yielding an evolution of charge states under consideration of ionization and competing mechanisms. Figure 6.3 depicts such an evolution, calculated by CBSIM [Mar10]. Recombination was suppressed, because we were only interested in a rough estimate. We also set the storage potential to a much higher value than 400 eV, what would apply for Ar^{13+} because of the before mentioned considerations.

The program simulates and plots the relative abundance of charge stages versus a logarithmic

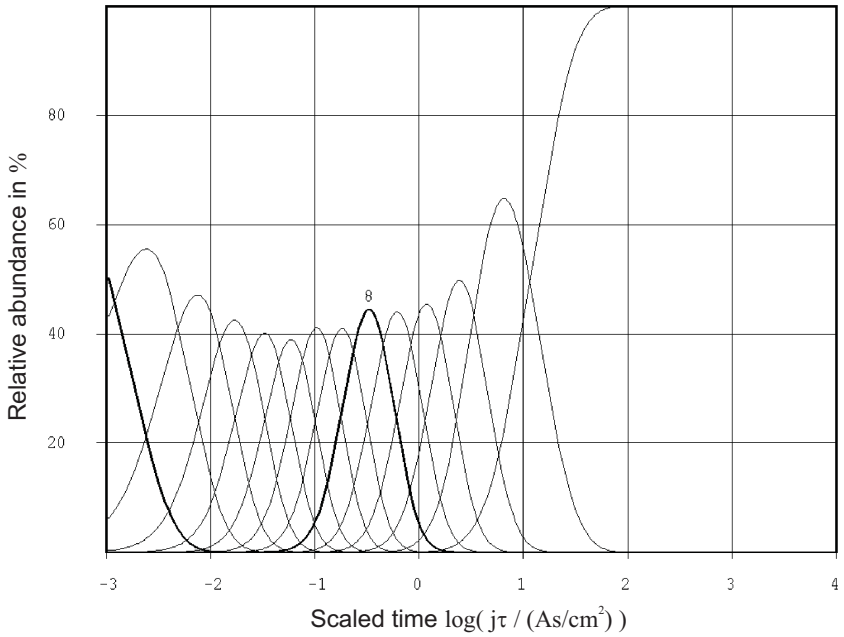

Figure 6.3: Charge breeding of argon, simulated with CBSIM. Parameters were 750 eV impact energy, $3 \cdot 10^4$ eV storage potential. Recombination and charge exchange were suppressed. The residual gas pressure was 10^{-7} mbar with 7 eV ionization potential.

time axis. Only such reactions are involved which depend linearly on the electron current density $j = e\rho_e v$. Therefore the editors of the program chose the quantity $j \cdot \tau$, measured in As/cm^2, as independent variable. The estimation 6.4 and the acceleration voltage 750 V yield $j \approx 0.25$ A/cm^2. With the information that the abundance of Ar^{13+} exceeds 60 % at $\log(j\tau) \approx 1.2$, we conclude[1] a breeding time of 80 s.

The first ionization step is treated differently: The loss rate R_0^s for atoms due to adsorption to the cold walls is given by the thermal velocity $v_a \approx 30000$ cm/s at room temperature, the approximate path length in the trap, $b \approx 10$ cm, and the sticking coefficient $S \approx 1$. These are conservative estimations, in particular the thermal velocity, because atoms will most probably slow down before they enter the vacuum chamber (see section 6.2). The rate $R_0^s = S\frac{v}{b} \approx 3$ kHz is a hundred times the optimized ionization rate 28 Hz, meaning that one percent of all atoms will be ionized.

There is an upper limit to the amount of gas that can be brought into the trap chamber, because we do not want to cover the electrodes with an insulating argon crystal. This will be estimated with the number of atoms needed to build up a monolayer on the $F = 37$ cm^2 inner surface of the creation trap. The lattice constant of closely packed argon atoms is $a = 4.1$ Å. Therefore, a monolayer corresponds to $N_M \approx F/a^2 = 2.2 \cdot 10^{16}$ atoms, translating to an upper limit of $N_1 = 2.2 \cdot 10^{14}$ Ar^+ ions. This is more than enough for our purpose. The necessary injection of argon gas is further discussed in the following section.

[1]This is apparently more optimistic than the lower limit according to table 6.1: Starting with a pure Ar^{12+}, the population of the daughter species will arrive at $60\ \% = 1 - e^{-0.92}$ only after $0.92/R = 186$ s. And this estimation neglects the time for production of the mother. However, we are satisfied with the result that a significant fraction of initially ionized argon atoms are bred to the 13^{th} charge state within reasonable time.

6.2 Gas Injection

Our present method of ion creation has the advantage that no charged particles must be injected into the magnetic field and vacuum chamber. Instead, argon in neutral form needs to be brought in. Hydrogen, carbon, oxygen or other elements richly abundant in solid matter, can be deposited in great amounts as part of a plastic target, for instance [Ulm06], or they are even found in contaminations without any extra efforts.

However, there are no natural compounds containing sufficient amounts of argon [KPR+00], since it is a noble gas. One option to obtain argon is to rely on the following argument: Argon makes up $p_{\mathrm{Ar}}/p = 1\ \%$ of the atmosphere. If the vacuum chamber of volume V_C is evacuated to 10^{-4} mbar before cryopumping, it will still contain

$$N = \frac{p_{\mathrm{Ar}} V_C}{kT} \approx 8 \cdot 10^{11}$$

argon atoms within the volume of the creation trap. These will be more or less uniformly adsorbed to the surface, of which the electron beam can access a fraction of 1 %. Bombardment with fast electrons can sputter atoms from the target material. However, such a maximum amount of 8 billion atoms may be sufficient for single particle experiments, but we would not rely on such a reservoir for the demands of spectroscopy.

Instead, a gas pipe is required, interrupted by a gas valve with the following properties [LBB+11]: It should separate the cryogenic vacuum in a trap chamber from a room-temperature low-pressure tube, attached to a gas bottle. Due to the proximity of the trapping region, the valve is situated in a strong magnetic field and has to be operable at cryogenic temperatures with remote control. To our knowledge, no such valve is commercially available. Here I describe a solution we have developed recently, modifying the idea of a cryogenic cell, operated at JINR Dubna [DDD+09]. It comprises no moving parts, but makes use of varying temperatures.

This cryogenic gas valve is connected to the lower side of the ultra high vacuum chamber (for an overview see chapter 4 and figure 4.1). Through this port, the chamber will be pre-pumped and, after cool-down, loaded with controlled amounts of gas for ion production. The gas valve is constructed in the following way: After a narrow stainless steel tube below the vacuum chamber comes an oven, namely a cylindrical copper box, partially divided by several baffles, which has a heating resistor attached (see fig. 6.4). The thermal contact to the trap chamber at 4 K ensures a temperature of about 7 K in the cold, i.e. 'closed', mode of the oven—section 6.2.1 goes into detail about heat and gas conduction. Another stainless steel tube is connected below the oven, leading out of the magnet bore, and thermally connected to the 45 K radiation shield at an intermediate point.

The working principle relies on cryogenic adsorption: Atoms coming into the oven have to hit the surface many times in order to travel through. In the cold mode, they will most probably stick to a wall, so the box acts like a closed valve and continuously pumps residual gas entering from the warm tube. When heated to about 80 K, two things occur: Firstly, the walls release adsorbed matter. Secondly, the sticking probability decreases, so that the valve is in the open mode. Depending on the temperature, this allows a controlled flow of atoms to the vacuum chamber. Section 6.2.2 presents a more quantitative discussion of the sticking.

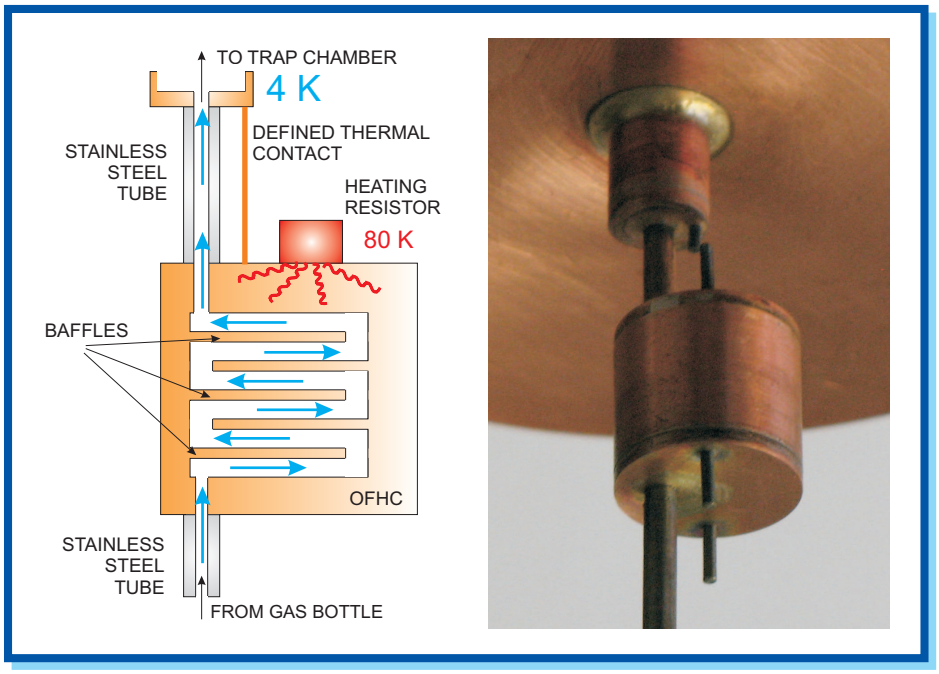

Figure 6.4: Schematic drawing of the adsorption valve with resistor case and copper wire mounted, viewed in vertical section, and photograph of the ca. 1.5 cm long oven with tubes, soldered to the vacuum chamber.

This consideration supposes that atoms will be reflected diffusely from the inner surface of the warm oven. Otherwise it would hardly be possible to match an atom beam into the aperture of the tube towards the chamber. Even in this low temperature regime, argon has a thermal wavelength of $\lambda = h/(2\pi M k_B T) \approx 20$ pm. This is much smaller than the structure of any realistic surface. Therefore diffuse reflection is granted, and there will be a fraction entering the attached pipe, even in the right direction to penetrate through the entire length. The pipe remains partially cold, so that atoms will freeze out there, if they deviate too much from the upward direction.

Several operating parameters of the valve can be set almost deliberately, such as pressure on the warm side, temperature of the box, heating time etc. This will enable us to adjust the optimum amount of gas injected into the trap chamber for ion production.

After charge-breeding to the boron-like state Ar^{13+} (see sec. 6.1) and cooling (section 5.4), the ion cloud will form a very stable reservoir for the measurements mentioned in section 3. The electrons can be removed from the chamber by setting the mesh end cap to a positive potential. Few particles or the cloud as a whole can be brought to the spectroscopy trap by transporting them in a moving electric potential minimum. As I have mentioned before, the magnetic field will be calibrated using the cyclotron frequency of a single known ion. For this purpose, only a small fraction of the cloud is brought into the spectroscopy trap. Similarly to evaporative cooling, the potential barrier is lowered until a single particle is left. Immediately after the cyclotron frequency measurement, the remaining ions are loaded from the reservoir for the spectroscopy experiment. Then the cloud is shifted back to the reservoir and a new cycle begins.

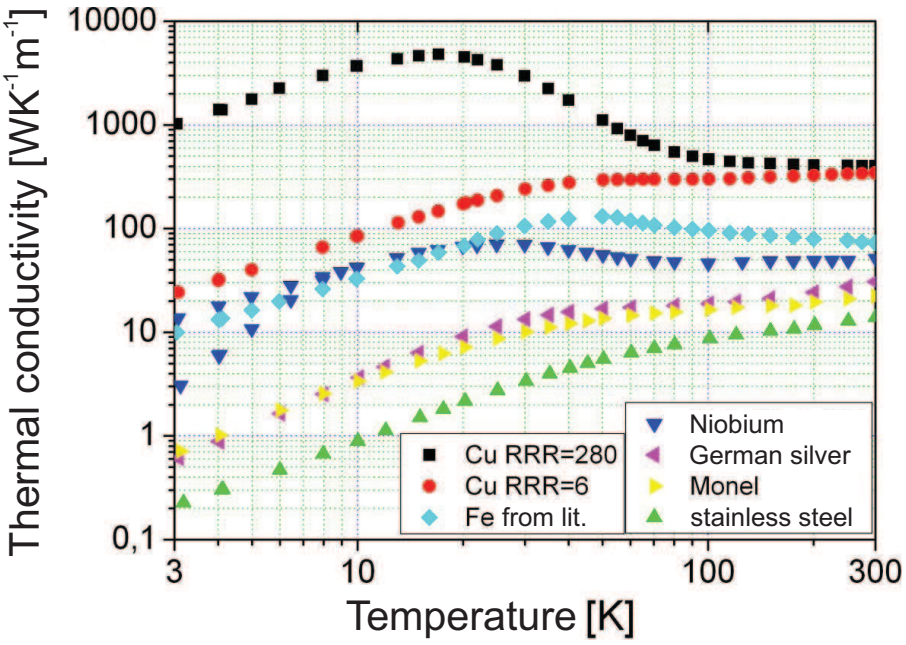

Figure 6.5: Thermal conductivity of several metals for cryogenic temperatures, figure taken from [Sch09]. OFHC copper has the highest, stainless steel the lowest values.

6.2.1 Design of the Valve

The shape of the oven itself has been designed such as to block the direct pathway between the stainless steel tubes, which are coaxial with the vacuum chamber. The choice of materials was motivated by their thermal conductivity: In the range below 100 K, the heat conductivity in stainless steel is roughly $\Lambda_{\mathrm{st}} = 0.1\ \mathrm{W/(K^2 m)} \cdot T$, whereas for OFHC copper it can peak to very high values up to 5000 W/(Km) at 20 K, depending on the purity. This can be read from figure 6.5, which also suggests that OFHC copper is among the best thermal conductors, whereas stainless steel is a relatively good thermal insulator. We approximate the copper curve to be constantly $\Lambda_{\mathrm{Cu}} = 1000\ \mathrm{W/(Km)}$ as a crude estimate. We want to consider thermal conduction through a rod-shaped object. Given its constant cross-sectional area A and the heating power P through it, we can derive the temperature profile $T(x)$ or the inverse relation $x(T)$:

$$\Lambda(T) = \frac{P}{A\frac{\mathrm{d}T}{\mathrm{d}x}} \quad \Rightarrow \quad \Lambda(T)\mathrm{d}T = \frac{P}{A}\mathrm{d}x.$$

If we insert the approximation for stainless steel, this is integrated to

$$\Delta x = 0.05\ \mathrm{mm}\frac{A}{\mathrm{mm}^2}\frac{\mathrm{mW}}{P}\frac{\Delta(T^2)}{\mathrm{K}^2}. \tag{6.5}$$

For copper we obtain

$$\Delta x = 1000\ \mathrm{mm}\frac{A}{\mathrm{mm}^2}\frac{\mathrm{mW}}{P}\frac{\Delta T}{\mathrm{K}}. \tag{6.6}$$

We want to satisfy two boundary conditions: (i) In the cold mode, the thermal load to the trap chamber—and consecutively to the cooler—shall not exceed 5 mW. (ii) During heating we can afford up to 100 mW. If the oven is not actively heated, the only heat source is at the connection to the radiation shield. We chose a stainless steel pipe with 3.18 mm diameter and 0.41 mm wall thickness for this connection. With the heating power of 5 mW flowing through a cross-sectional area of 3.6 mm^2, the temperature drops from 45 to 7 K over a length of 72 mm—being the distance between the oven and the shield. For the remaining drop from 7 to 4 K at the trap chamber, we use an OFHC copper wire with 8 mm length and 0.125 mm diameter to bypass the 15 mm long tube as can be seen in figure 6.4. In contrast to many other materials, the thermal conductivity below 10 K is comparable or even higher than the values between 10 and 80 K (see fig. 6.5). Only by this fact it is possible that the oven temperature in the cold mode will be around 7 K, whereas the heat load at 80 K is in the order of 110 mW—according to the estimation 6.6. Under these conditions, the stainless steel tube adds a heat load of 30 mW in the warm mode.

The foregoing reasoning brought the radiation shield in contact with a heat source, but the following point should be considered: If the tube was not anchored to the shield, it would form a direct connection to the room temperature environment. In this case a length of 3 m would be necessary. This shows that the shield serves as heat sink—now the entire tube can be much shorter, which is of advantage for pumping. To quantify this, we want to estimate of the pipe conductance. As long as inter-molecular collisions are the dominating process of momentum exchange, pumping can be described by the law of Hagen-Poiseuille for a laminar flow [Mes10],

$$\dot{V}_l = \frac{\pi r^4}{8\eta}\frac{\mathrm{d}p}{\mathrm{d}z}. \tag{6.7}$$

$\dot{V}$ denotes the volume flow (or synonymously conductance) through a tube of radius r and length l. η is the viscosity and $\mathrm{d}p/\mathrm{d}z \approx \Delta p/l$ the differential pressure drop. If the long pipe is the bottle neck of pumping power, we can assume zero pressure on one side and homogeneous pressure p (initially 1 bar) in the vacuum chamber. This corresponds to a particle number of

$$N = \rho V_C = \frac{pV_C}{k_B T},$$

where V_C is the chamber volume and ρ the gas density in it. We approximate the flow law 6.7: $\dot{V}_l = \kappa p$, $\kappa = \pi r^4/(8\eta l)$. The loss rate of total number of molecules is proportional to the flow rate: $\dot{N} = -\rho \dot{V}_l$, and thus we can find a differential equation for the pressure, assuming isothermal expansion:

$$\begin{aligned} \frac{\dot{p}}{p} = \frac{\dot{N}}{N} &= -\frac{\dot{V}_l}{V_C} = -\frac{\kappa p}{V_C} \\ \Rightarrow \frac{\mathrm{d}p}{p^2} &= -\frac{\kappa \mathrm{d}t}{V_C} \\ \Rightarrow \frac{1}{p} - \frac{1}{p_0} &= \frac{\kappa}{V_C}(t - t_0). \end{aligned}$$

Atmospheric pressure p_0 is almost 5 decades higher than the pressure p_T at which a transition from laminar to molecular flow occurs [Umr97]. So by neglecting $1/p_0$, we find a pumping time

of $t(p) = V_C/(\kappa p)$. At sufficiently low pressure, the mean free path reaches the dimension of the tube diameter and can no longer increase inversely proportional to the pressure. This marks the transition to molecular flow, where the conductance equals

$$\dot{V}_m = \frac{8r^3}{3l}\sqrt{\frac{\pi kT}{2M}}. \tag{6.8}$$

With the chamber volume we find a time constant of the now exponentially decreasing pressure: $\tau = V_C/\dot{V}_m$. To the length of the stainless steel tubes, an effective length of the oven for molecular flow has to be added. According to [Umr97], we estimate this to be 280 mm. With values for air ($M \approx 28$ GeV/c^2) at atmospheric pressure and with the tube and chamber dimensions we obtain the following results:

λ_0	=	60 nm	η	=	17 μPas
r	=	1.2 mm	l	=	700 mm
V_C	=	$3 \cdot 10^6$ mm^3	κ	=	68 mm^3/(Pas)
p_T	=	2.5 Pa	$t(p_T)$	=	$1.75 \cdot 10^4$ s = 4.9 h
$\dot{V}_m$	=	$2.0 \cdot 10^3$ mm^3/s	τ	=	$1.5 \cdot 10^3$ s = 25 min

Pumping to a pressure of 10^{-4} mbar $= 10^{-2}$ Pa will take about 7 hours.

6.2.2 Simulation and Test

The propagation through the valve has been simulated with Molflow+ [Mar10, Tin86, MS08]. Two virtual boundary areas are defined perpendicular to the pipe axis, roughly at the places of the arrows 'from gas bottle' and 'to trap chamber' in figure 6.4. A screenshot of the graphical user interface is shown in figure 6.6 for illustration. The virtual surface below the oven acts as gas source. The simulation generates a million atoms which start from here. The surface above is at the entrance of the vacuum chamber. It adsorbs and counts every atom arriving there. The other walls are the real inner surfaces of the oven and pipes. They are set to a certain sticking coefficient S. An atom touching such a wall will either be reflected diffusely with the probability $1 - S$ or adsorbed. The number of particles arriving at the top, divided by one million, is interpreted as propagation probability P.

The sticking coefficient depends on the temperatures of the surface and the gas. Literature values are in the range above 90 % for 4 K and fall below this value at a temperature of around 30 to 80 K. Some values have been collected and plotted in figure 6.7(a). With such high sticking probabilities, only very few particles will arrive, resulting in poor statistics. This consideration and the rather imprecise knowledge of the coefficient itself motivates the following method: The Monte-Carlo simulation is applied for different values of the sticking coefficient, and the probability P for an atom to arrive at the end surface is recorded. By an extrapolation to high coefficients, we can overcome the lack of statistics and obtain a more general estimation rather than just for one particular value of S. We expect a simple behavior: If an atom reaches the chamber, it must have hit the wall several times—the average number of such collisions shall be $\bar{z}$. $1 - S$ again denotes the reflection probability for each collision. Then the probability of propagation through

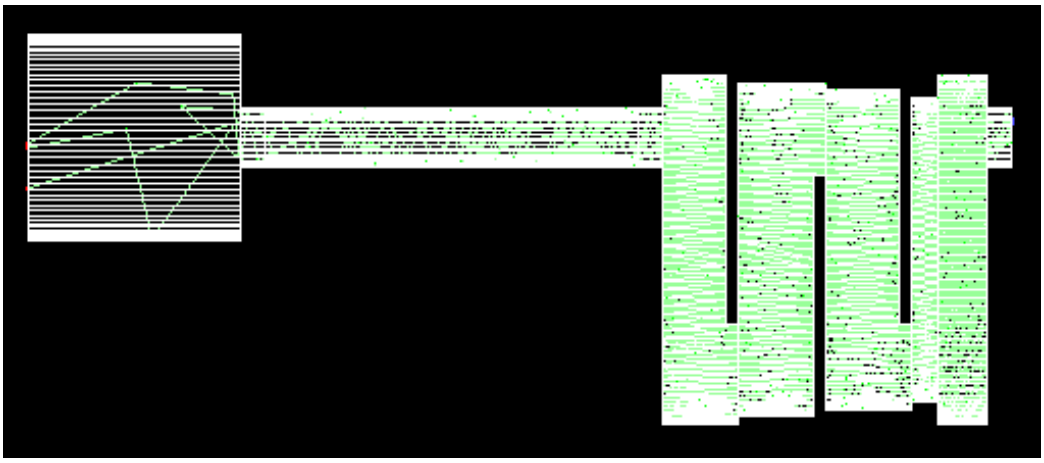

Figure 6.6: Part of the graphical output of a Molflow+ simulation [Mar10]. The inner surfaces of the oven and tubes are shown. The image has been turned by 90° counterclockwise with respect to the orientation in the experiment. In addition to the surfaces, some events are drawn in the screen. A blue dot represents atom desorption, green stands for reflection and red marks adsorption. The light green lines are trajectories. Although a million atoms have been simulated, only three of them are shown. In the present case, the sticking coefficient is zero and all atoms arrive at the top (left surface in the drawing).

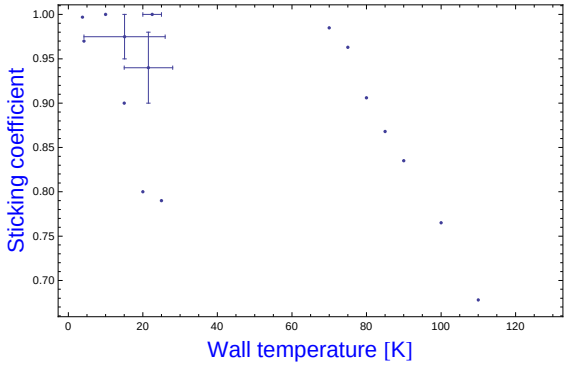

(a) The sticking probability S of argon gas on a cold wall, according to the references [Hae81, Lev71, IYF04, FBM93]. The discrepancies result from different gas temperatures.

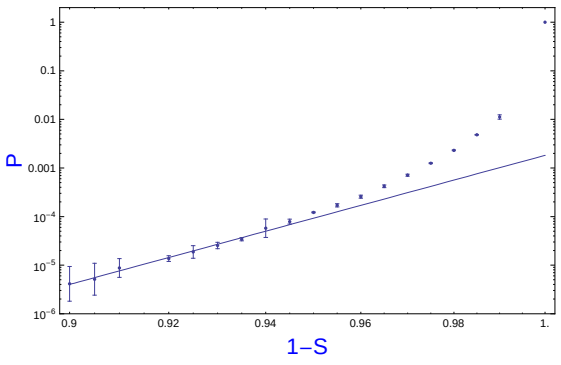

(b) Simulated propagation probability P for different sticking coefficients [Mar10].

Figure 6.7: Plots of sticking data and propagation probability.

the whole valve should be

$$P = (1 - S)^{\bar{z}}. \tag{6.9}$$

As long as atoms do not return from the chamber, this probability times the initial number of atoms is equal to the number of hits registered on the upper virtual plane. In a double logarithmic plot $\log P$ vs. $\log(1 - S)$, this would result in a line through the origin ($\log 1 = 0$) with the slope $\bar{z}$. Fig. 6.7(b) confirms this model to some extent: For sticking coefficients higher than 0.06 the simulated data can be approximated well by a straight line

$$\log P = m \log(1 - S) - b \tag{6.10}$$

with a slope m of 58 and an axis intercept at -2.74. These values depend on the fitting interval (if it is extended down to 0.02, they are 72 and -2.23), but in the range above $S = 6\,\%$, the fit and data agree within the error margins for either choice of parameters. Only if even lower sticking coefficients are included, the data cannot be consistently described by a straight line. As expected, for zero sticking, the propagation probability is one—but this important data point deviates significantly from the linear fit. The slope m in equation 6.10 directly corresponds to the average number of collisions. A non-zero axis intercept has no explanation within the model 6.9. Instead, if particles could return from the vacuum chamber and cross the entrance surface several times, this could lead to count numbers higher than one million. This effect scales with the sticking coefficient that is assigned to the virtual entrance surface. In our simulation, this surface was pumping perfectly, which excludes the effect and is well represented in the data point $(1 - S, P) = (1, 1)$.

Despite this open question, we extrapolate the fit up to 90 % sticking. We choose a rather conservative set of parameters to estimate the worst case of relatively high gas transmission in the closed mode and obtain $10^{-60.8}$. For a sticking coefficient of 0.5, the different fits yield probabilities between $10^{-23.9}$ and $10^{-20.2}$. According to this model, there will be only very few atoms arriving in the chamber, even if argon comes with atmospheric pressure from below the oven. It is clear that for medium-high temperature—corresponding to 50 % sticking—we must also take into account desorption from the inner surfaces of the oven. Apart from that, the sticking probability depends on the surface material and various contaminations, such as a layer of argon itself [FBM93].

Therefore, the presented simulations can only give a faint idea of the real behavior in the oven. In order to learn more about the gas flow, we will use the test setup described in section 4.1. The valve, which has been soldered to the vacuum chamber, will be connected to the cooling and heating devices as described in the previous sections. An IKR vacuum gauge will be placed next to the gas port of the copper vacuum chamber. The function and calibration of this gauge is briefly described in section 7.3. It is designed to detect atoms, if the pressure exceeds 10^{-11} mbar. These measurements could clarify how realistic the above presented models are. Also the reproducibility will be studied in order to estimate the role of an argon layer as mentioned before.

Chapter 7

The Electron Source

The emission of electrons from solid materials can be achieved through the thermionic, the photoelectric and the tunnel effect. The first is discarded because we cannot afford any avoidable heat load to the second stage of the cold-head—it has a cooling power of 1 W. The second was considered an option. The ATRAP collaboration reported successful use of a metal-coated window for production of an electron beam coaxial with the antiproton beam [LGL+07]. Thereby the antiprotons inevitably have to travel through the window, which fulfills the role of degrading them from 5 MeV to a few keV. The antiparticles are also strongly reduced in number and heated up, but the electrons are used to cool them in the trap. This works for the case of an intense beam of fast antiprotons—but in our situation, the subthermal atoms would have no direct access to the production trap. Further complications would be posed by the need for coupling in ultraviolet light for photoelectron production. A much more practical solution was found in the field emission electron source which is described in this section. The particular geometry (see fig. 7.1) with a tip pointing radially into the trap allows unperturbed axial access of both atoms and ions. This chapter first recalls basic properties of field emission, then I report on the machining and commissioning of the tips.

7.1 Field Emission

The underlying process of field emission is the tunneling of electrons through the potential barrier at the edge of a metal. The material forms a potential well with the depth W_a. In the free electron gas model, electrons do not interact with each other, but they obey the Pauli principle, thus they cannot all have zero kinetic energy. Therefore, the well is filled up to a maximum kinetic energy, the Fermi energy ϵ_F. The absolute value of the binding energy at the Fermi edge is the work function ϕ. The values for tungsten found in the literature are a work function of about 4.5 eV and a Fermi energy of 10.5 eV [Mah05]. Thus, we obtain a potential depth of 15 eV.

In the simplest case of two infinitely extended opposing plates at the distance d, there is a constant electric field $\mathcal{E}_a = U/d$ in the free space, where U is the acceleration voltage applied to the anode. The cathode shall be grounded. The attraction of an electron outside the solid material to its image charge is described by an additional term $e\mathcal{E}_i = -\alpha\hbar c/(2x)^2$ [Jac75]. This results in

a potential

$$V(x) = -W_a\theta(-x) + \left(-e\mathcal{E}_a x - \frac{\alpha\hbar c}{4x}\right)\theta(x). \tag{7.1}$$

$\theta(x)$ is the Heaviside step function. Already in the early days or quantum mechanics, Fowler and Nordheim [FN28, Nor28] solved this problem with a semiclassical approach, where tunneling through an arbitrary potential well is derived from the transmission through an infinitesimal well. I will only quote the most important results of this derivation, which is widely discussed in literature. For technical details I refer to the diploma thesis of S. Ulmer and citations therein [Ulm06]. I rather want to point out weak points of the model at the end of this section.

The tunneling current density for particles with charge e, mass m, velocity v, total energy $E < 0$, kinetic energy $\epsilon = mv^2/2 = E + W_a$ and density ρ is

$$j = ev\rho \left|S_V(E)\right|^2, \tag{7.2}$$

where $|S_V(E)|^2$ denotes the tunneling probability. The latter can be calculated exactly for a rectangular potential well of length d and height V_0:

$$|S_{\mathrm{rect}}(E)|^2 = \exp\left(-\frac{2}{\hbar}d\sqrt{2m(V_0 - E)}\right). \tag{7.3}$$

If the potential varies slowly compared to the wave function, i.e.

$$\left|\frac{1}{\epsilon}\frac{\mathrm{d}V}{\mathrm{d}x}\right| \ll |k| \equiv \sqrt{\frac{2m|V(x) - E|}{\hbar^2}}, \tag{7.4}$$

then the wave function and its modulus can be estimated with the WKB (Wentzel, Kramers, Brillouin) approximation [Kra26]:

$$|S_V(E)|^2 = \exp\left(-\frac{2}{\hbar}\int \mathrm{d}x\ \sqrt{2m(V(x) - E)}\right).$$

The integral is evaluated between the zero axis intersections of the square root:

$$\begin{aligned} |S_V(E)|^2 &= \exp\left(-\frac{4\sqrt{2mc^2E^3}}{3\hbar ce\mathcal{E}_a}v(y)\right), \\ v(y) &\approx 1 - 0.213y - 0.799y^2, \\ y &= \sqrt{\frac{\alpha\hbar ce\mathcal{E}_a}{E^2}}. \end{aligned} \tag{7.5}$$

The variable y and the function $v(y)$ are chosen according to [BKH53] and account for the influence of the image potential. We further define $\tilde{y}$ to be y with the binding energy E being evaluated to the negative work function, that is, the energy at the Fermi edge.

Coming back to the expression 7.2, the differential electron current density in an energy interval $[\epsilon, \epsilon+\mathrm{d}\epsilon]$ is given by the product of the density of states $D(\epsilon) \propto \sqrt{\epsilon}$ and the Fermi Dirac distribution $n(\epsilon, T)$:

$$\mathrm{d}j = ev\ D(\epsilon)\ n(\epsilon, T)\left|S_V(E)\right|^2 \mathrm{d}\epsilon,$$

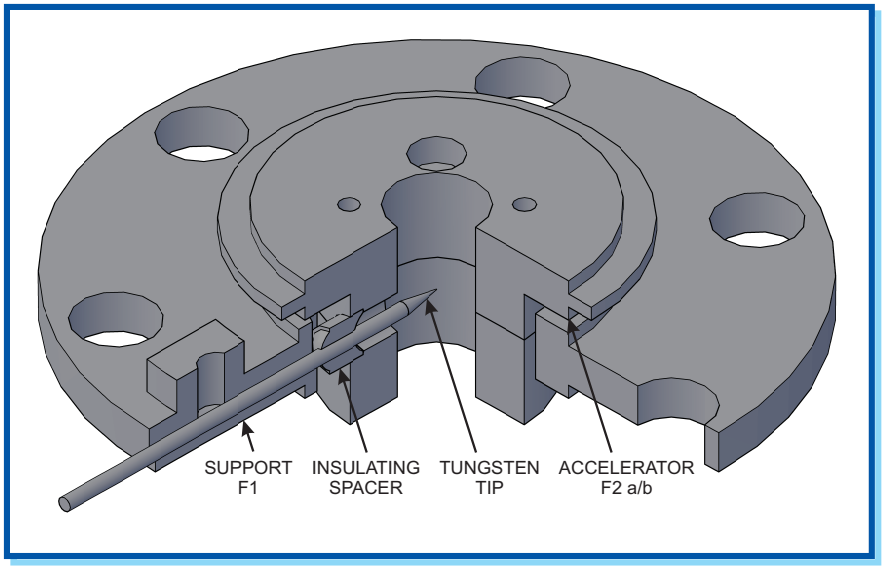

Figure 7.1: Drawing of the electrodes used to operate the field emission points.

which is integrated to obtain the total current density:

$$
\begin{aligned}
j &\approx \frac{a\mathcal{E}_a{}^2}{\phi} \exp\left(-\frac{b\phi^{3/2}}{\mathcal{E}_a} v(\tilde{y})\right), \\
a &\approx 1.5 \, \frac{\mu\mathrm{A\ eV}}{\mathrm{V}^2}, \\
b &\approx 6.8 \, \frac{\mathrm{V}}{\mathrm{nm\ eV}^{3/2}}.
\end{aligned}
$$

The size A of the emitting surface finally leads to the emission current $I = Aj$. The experimentally observed characteristic $I(U)$ can be modified to the Fowler-Nordheim form $\ln(IU^{-2})$ vs. U^{-1} and compared to the prediction

$$
\ln \frac{I}{U^2} = \text{const} - \frac{b\phi^{3/2}}{\mathcal{E}_a v(\tilde{y})} \approx \text{const} - \frac{m}{U}. \tag{7.6}
$$

From the slope m, the plate distance can be derived. Values for tungsten (see above) yield:

$$
d = \frac{U}{\mathcal{E}_a} = \frac{m}{b\phi^{3/2}} = 15 \ \mathrm{kVnm} \cdot m. \tag{7.7}
$$

Discussion

Now I want to check several assumptions made in the foregoing derivation. Instead of two infinite plates we employ a sharp tip as cathode which is surrounded by an acceleration electrode (see figure 7.1 and 7.2). The effective radius of curvature of this tip is defined by the anode voltage and the relevant field strength close to the tip. It replaces the plate distance d:

$$
r_c \equiv \frac{U}{\mathcal{E}_a}.
$$

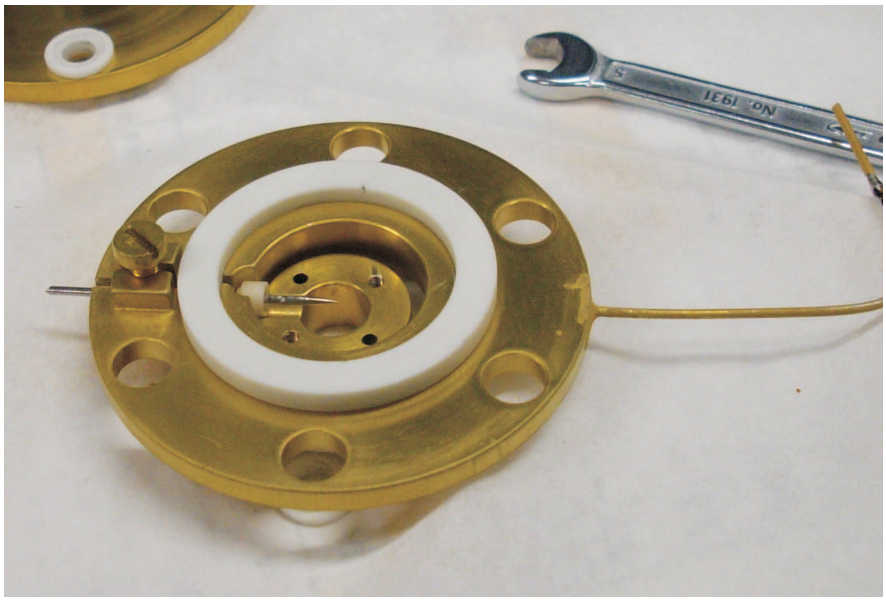

Figure 7.2: F1 and F2 with tungsten tip, screw and spacers.

The model of a constant electric field can be a good approximation if the tip has a planar geometry on the length scale $l \approx W_a/(e\mathcal{E}_a)$ of the classically forbidden zone. From the interpretation of r_c as a radius, it is clear that the tip is planar only at much smaller scales than this parameter. This implies the relation

$$|W_a| \ll |eU|$$

as a condition for the validity of the quantitative tunneling model. With the value of 15 eV for the potential depth W_a and an acceleration voltage U in the range of 800 V, the condition is well satisfied.

On the contrary, the assumption of large wave vectors, equation 7.4, is violated in every tunneling process, since at the edges of the potential well there is always a region with $k = 0$ and often particularly strong forces $\mathrm{d}V/\mathrm{d}x$. Only in the last decades, a fully quantum mechanical treatment of field emission was published [LL91]. Both the WKB method and the fully quantum mechanical solution neglect the current reduction due to space charge buildup close to the cathode (Schottky effect) [Ota07].

The total current should be obtained from an integration over the surface of the tip. Equation 7.6 assumes that the electric field and thus the current density is constant along an emitting surface A and zero everywhere else. An interesting point in this respect is the following: For electrons at the Fermi level $E = -\phi$, the values $y = 1$ and $v(y) = 0$ (see definition 7.5) are reached for a critical field strength $\mathcal{E}_{\mathrm{crit}} = 14\,\mathrm{V/nm}$. This means that electrons with the highest energy are no longer bound to the metal, leading to a tremendous increase of the current. For a geometry with one very sharp tip, this critical field is reached at a well-defined area, when the voltage exceeds a critical value U_{crit}. Only at much higher voltage, also less sharp parts of the surface will start firing and the emission characteristic deviates from the shape as described by

equation 7.6. If instead there are several tips with similar curvature, the emission current will be multiplied even in the regime of the initial critical voltage.

A further deviation from the linear form used for the Fowler-Nordheim fit is the dependence of the auxiliary function $v(\tilde{y})$ on the field strength. At low field strengths, $v(\tilde{y})$ is one, but for the critical field it gets zero. The physical interpretation is that the potential barrier can completely vanish and many electrons will be emitted with unitary probability instead of the exponential factor. Therefore, the determination of the radius of curvature according to equation 7.7 is only possible for low field (and current).

From the point of view of application, the particular shape of the characteristic is of minor importance. It is only used to distinguish field emission from the leakage currents through parallel resistors. The most important feature of the characteristic is the step-like shape. If this behavior is identified, the radius of curvature can be determined from

$$r_c = \frac{U_{\text{crit}}}{\mathcal{E}_{\text{crit}}} = 71 \, \frac{\text{nm}}{\text{kV}} U_{\text{crit}}, \tag{7.8}$$

as an alternative to equation 7.7 for the high current regime. Here it can also be seen clearly that for reasonable values of the applied voltage (about 1 kV), structures of less than 100 nm are necessary for field emission.

7.2 Field Emission Point Production

The tips have been produced from 1 mm thick rigid tungsten wire at a dedicated lab course experiment of Mainz University. The setup shown in figure 7.3 applies an electrochemical etching process in a particular way which allows to shape a sharp point. For a detailed description of the chemical process and practical information on handling the production I refer to appendix B.

A short tungsten wire is suspended in a sodium hydroxide bath and biased with +10 V. Tungsten ions dissolve from the surface and the wire narrows down. At the narrowest point the gravitational tension increases with the inverse square of the diameter, until the lower part of the wire breaks off. The etching process ceases immediately for this part, because it is disconnected from the anode. It falls down and is smoothly caught by a blob of shaving foam. This lower part later serves as cathode for field emission of electrons. With this assumption we derive the fracture diameter d' in appendix B. According to equation B.1, a 3 cm long wire will only be constricted to a diameter of 2 μm. However, tests with the tips made from the thick wire (see following section) did not confirm this consideration, but yielded much better results.

7.3 Field Emission Point Test

Immediately after the tips had been produced they have been labeled and inspected under an optical microscope with 4-fold magnification for documentation. Three of them had visible damages, whereas another one was polluted. The remaining 4 tips with labels 2, 4, 5 and 6 looked acceptable. However, an optical microscope can not tell if a tip has 100 nm radius of curvature. The best way to find out if the produced points emit a sufficiently high electron current is to test them in a setup similar to the one they have been designed for. So I mounted one tip after the

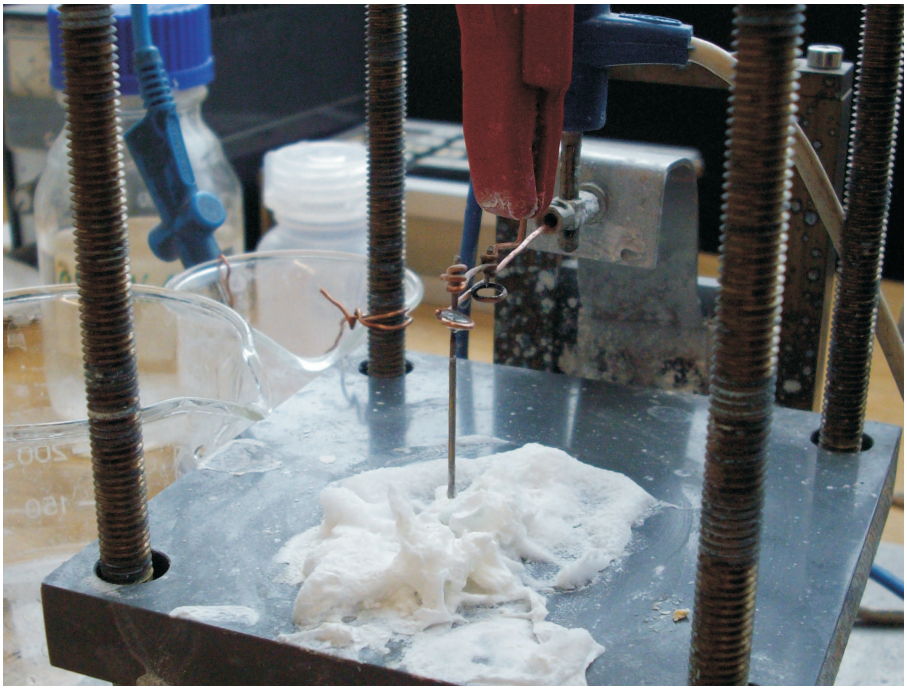

Figure 7.3: The production setup in Mainz. One tip has fallen down and been taken away from the shaving foam, the second one is almost finished.

other in an assembly of the electrodes H19, F2, F1. (See figure 7.5, for nomenclature refer to figure 4.2.) This stack was continued by one of the capture electrodes (e.g. C10) and completed by H8. The electrodes were insulated from each other by vitronit spacers. This stack could easily be mounted to threaded rods and in this configuration the tip was shielded almost completely from the environment. For several reasons it is necessary to wear gloves when assembling the components: The acid greases on the skin could penetrate through the fine galvanic layers and corrode the copper. Furthermore, they could bypass the insulating spacers—the measured leakage current revealed that the parallel resistance of the setup was in the order of a teraohm. On the contrary, the degassing of such substances was a minor point, because a pressure of 10^{-6} mbar is low enough for the purpose of this test. When discharges had occurred during operation, I polished the spacers with fine sandpaper and cleaned them in an acetone bath before reassembling, because any traces could lower the resistance.

The rods were fixed to a vacuum flange with high voltage feedthroughs and a UV glass view port (axial). A CF150 cross piece served as rubber-sealed vacuum chamber. The remaining ports hosted a Pfeiffer TMU 520 turbomolecular pump, a CF40 T-piece with two UHV gauges and a KF40 reduction piece which could be used as radial viewport for alignment purposes. The whole chamber was mounted to an Item® frame and connected to an Edwards RV12 forepump.

As gauges I used inverse magnetron tubes with a cold HV anode and an axial magnetic field. They ignite through field ionization and measure the current that results from a discharge avalanche. The Edwards AIM-S-NW25 and IKR 020 gauges were controlled by an Edwards TIC INST CONT and Balzers TPG 300, respectively. Both devices are specified with a 30 %

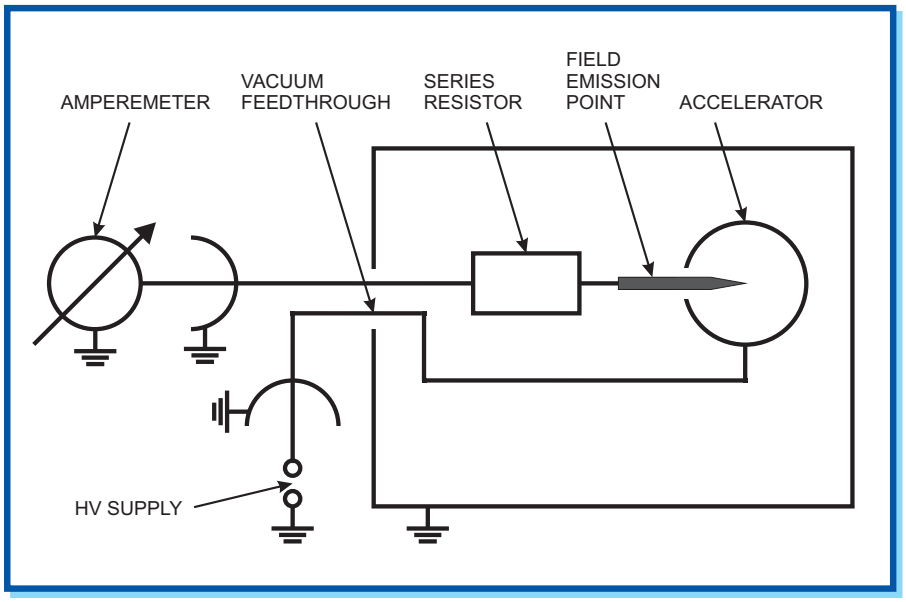

Figure 7.4: Equivalent circuit diagram of the wiring for the FEP test.

tolerance—their display always agreed within this margin. This observation served as a calibration check of the IKR for later use as a test instrument of the cryogenic gas injection (see section 6.2.2).

The FEP support electrode F1 was connected to the HV feedthrough via a series resistor for current limitation (see figure 7.4, nominal resistance of 200 MΩ). The current I through this electrode was measured with a Keithley Instr 414 S Picoammeter. The NIM modules Bertan Model 365 (positive bias) or Bertan Model 375N (negative bias) supply the uniform high voltage for the remaining electrodes, thus defining the extraction voltage U.

Within several hours the chamber was evacuated to roughly $7 \cdot 10^{-7}$ mbar. The zero point on the picoammeter was checked as well as the output of the voltage supply in the low voltage regime. Then the characteristic was taken in voltage steps of at least 50 V. When the voltage had been set to a new value, the current was read after waiting until it had stabilized. Thus the interval between several kV and zero—in case of tip 2 even −2.5 kV—was scanned back and forth to check for hysteresis.

The measured data U and I were processed as follows: The voltage drop across the resistor was calculated and subtracted: $U' = U - RI$. To this end, the actual resistance was determined to be 216 MΩ by short circuiting it to the high voltage electrode. U' is the physically relevant voltage which has to be inserted into the formulas from section 7.1. The characteristic I vs. U' was recorded at negative and low positive extraction voltages to quantify the leakage current I_0 through the feedthrough, the cables and spacers. In the regime below 500 V the characteristic is sign-insensitive, as figure 7.6 demonstrates. A quadratic fit to the relation of absolute values ($|I|$ vs. $|U'|$) shows good agreement, cubic and quartic fits don't give much different results.

Several reasons make the radius determination in a Fowler-Nordheim-plot (eqn. 7.7) practically impossible also for low currents:

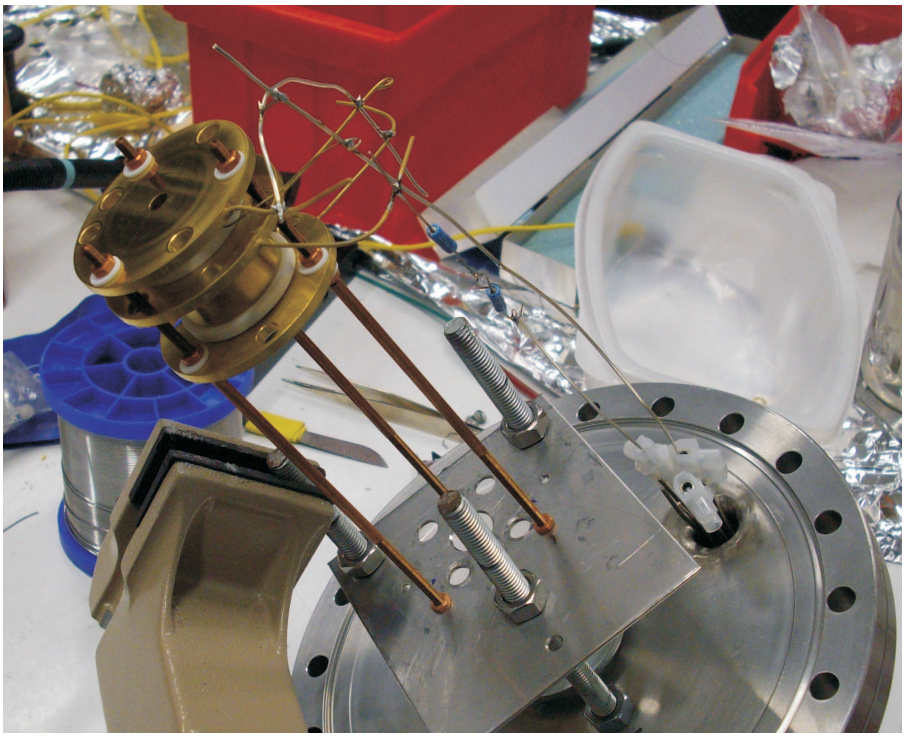

Figure 7.5: Electrode stack mounted to the vacuum flange with high voltage feedthroughs and a view port.

- A wide range of data points is needed to fit the non-linear leakage current characteristic, and it is hard to tell, how much of the non-linearity comes from field emission.
- The sign-insensitivity that occurred with tip 2 (with the other tips, no negative voltages were recorded) indicates that in the regime below 500 V the field emission current does not significantly differ from zero.
- There is an important source of systematic error, particularly in the low-current regime: When the voltage was set to a new value, the relaxation of the current happened very slowly (of the order of minutes) and showed some nonlinear behavior in the sense that the time constant depended on the deviation from the asymptotic value. There must be an effect other than the charging of a capacitor. We tried to clarify this by measuring the impedance between the two connectors with a PHILIPS PM 6303 RLC meter. The display did not stabilize, but often showed a capacitance of 5 pF and an inductance in the order of a kilohenry. This is clearly not related to a real coil, but it agrees with the behavior of slowly adapting currents. We couldn't find a satisfactory explanation for either. One reason might be that the impedance meter cannot handle a resistance of 200 MΩ.

Since the uncertainty doesn't allow a determination of the emission current at low voltage, we will stick to the uncorrected data. Now the only means left is to look for the step-like shape and use equation 7.8. Figure 7.7 shows double-logarithmic plots of the current-voltage characteristics. The most important observations are:

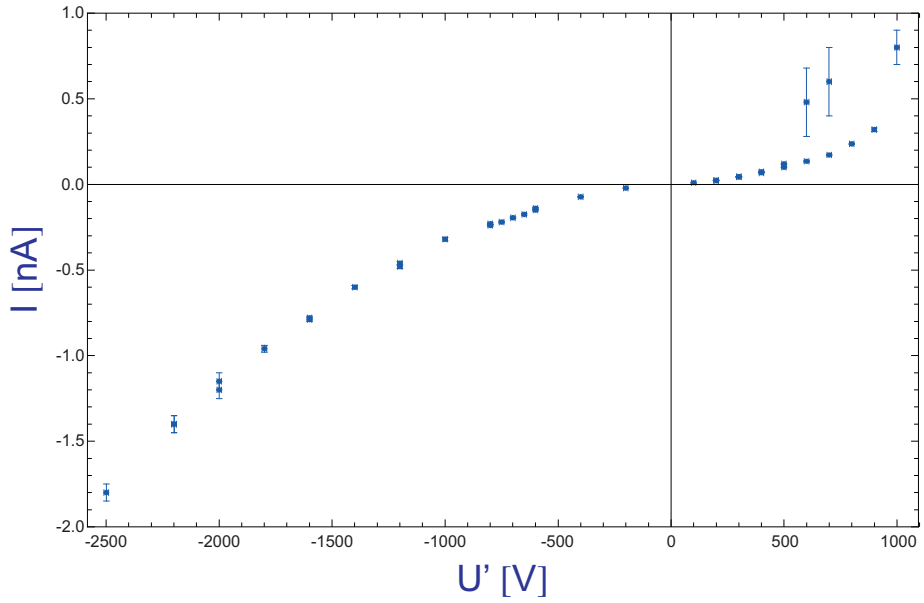

Figure 7.6: Leakage current characteristic, measured with tip 2.

Table 7.1: Estimated critical voltages and effective radii of curvature for three field emission points.

Tip label	U_{crit} [kV]	r_c [nm]
2	0.41	30
5	0.71	50
6	0.33	23

- Above a voltage threshold of several hundred volts, currents of some microamp can be detected. The quantitative analysis is given in table 7.1.

- The high current shows the quadratic behavior expected from equation 7.6. This can be well recognized in the double-logarithmic plot, since I chose equal scales for both axes. Then a quadratic law is depicted as a straight line with slope 2.

- In a certain voltage regime the current depends strongly on the history. Red arrows in the plots suggest a chronological order, which roughly describes the order of the data points. Even though we didn't find pure hysteresis, there is the tendency. For rising and falling voltage, the step between high and low current (i.e. emission and no emission) is retarded. This effect has been reported earlier [Ota07] and is explained with deformation of the tip as well as cleaning from contaminations which change the work function.

- An example of a tip not emitting at reasonable voltage is number four, see figure 7.8

Three out of four tested tips were found to have radii below a hundred nanometers in contrast to the expectation of two micrometers according to equation B.1. Possible explanations for the

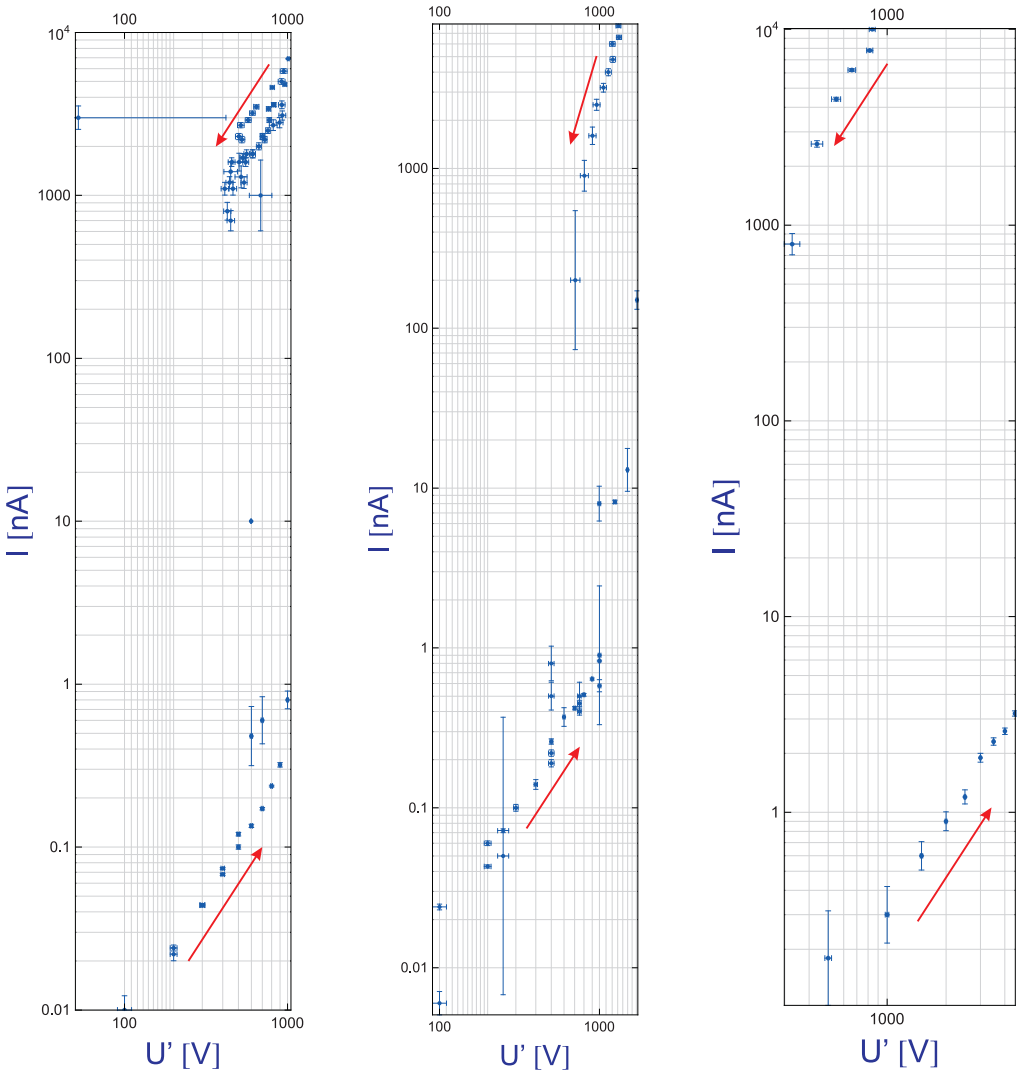

(a) Tip 2 (b) Tip 5 (c) Tip 6

Figure 7.7: Current-voltage characteristic of three tips, double-logarithmically with equal scales. The explanation is found in the text.

surprisingly small values are stated below. A definite answer could be found if the tips were observed in an electron microscope.

- Necking: At high stress, but before fracture, a reduction of cross-sectional area can occur in ductile materials. Similar to a liquid, atoms move in order to decrease the surface tension, if they are not so strongly bound to a particular position. If this explanation applies, the etching should be switched off as soon as necking starts, because the structural development needs some time. But since this goes along with continually growing stress, the sharpness is still limited. However, this explanation seems rather unlikely, because I used explicitly brittle tungsten.

- Particular shape: Even if the fracture produces a flat top of 2 μm diameter, the edge can be

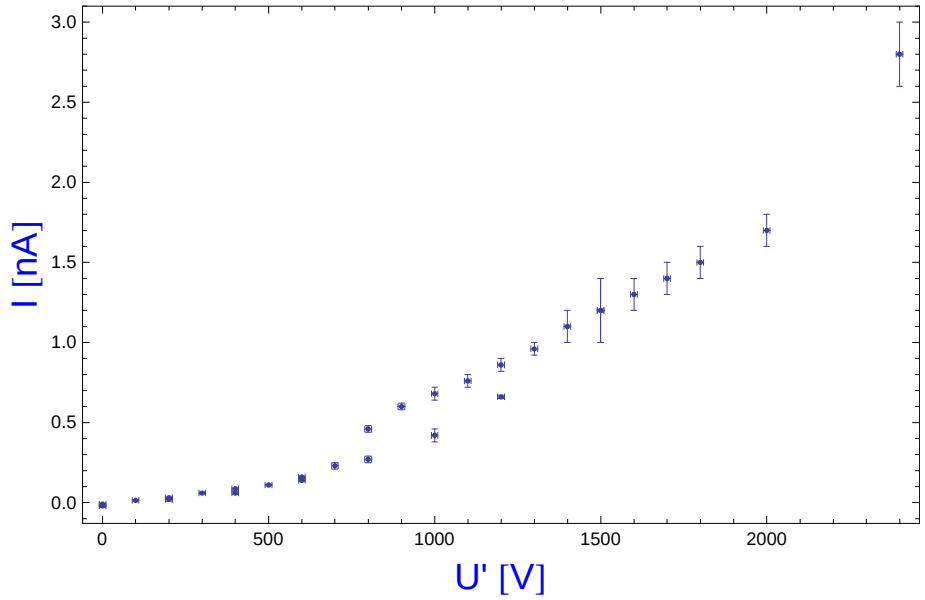

Figure 7.8: Current-voltage characteristic tip 4: No field emission detectable.

much sharper. Depending on the overall geometry in the field emission setup, this can still lead to a high electric field. In this case, any deformation would blunt such edges, thus fast etching and brittleness support this phenomenon.

7.4 Discussion

The tests were intended to simulate the situation during the experiment. Since I used the original geometry, the relation between extraction voltage and electric field will be exactly the same again. However, two important parameters will be changed in the final setup: The temperature and the magnetic field.

Firstly, at non-zero temperature, the Fermi edge is smeared out, resulting in a combination of field and thermionic emission. The effect of this can be quantified by the following estimation: The maximum of the confining potential 7.1 depends on the electric field as

$$V_{\max} = -\sqrt{\alpha\hbar c\, e\mathcal{E}_a}.$$

The derivative with respect to the field, evaluated at $\mathcal{E}_{\text{crit}}$ is

$$\left.\frac{\mathrm{d}V_{\max}}{\mathrm{d}\mathcal{E}_a}\right|_{\mathcal{E}_{\text{crit}}} = -2\frac{\alpha\hbar ce}{\phi} \approx -0.64\ \frac{\text{eV}}{\text{V/nm}}.$$

The thermal energy can be taken as a measure for the smearing out of the energy distribution, so there are many electrons with an energy of $-\phi + k_B T$. These can be classically extracted with a

lower field. For room temperature, this means a shift of

$$\mathrm{d}U_{\mathrm{crit}} = r_c k_B T \frac{\mathrm{d}\mathcal{E}_a}{\mathrm{d}V_{\max}} \approx -2\ \mathrm{V}$$

in terms of critical voltage. At cryogenic temperature, we cannot rely on this helping effect, but we have to apply 2 V more than in the test—this is feasible.

Then, the magnetic field plays a role by transforming the quasi-continuous conduction band to a series of Landau levels, separated by the cyclotron frequency $\Delta E = \hbar\omega_c$. Here, $\omega_c = \frac{e}{m^*}B$ is the cyclotron frequency of the electrons bound to the metal, but for this estimation we will make no difference between the effective mass m^* and the free electron mass m. At a sufficiently strong field strength, the modifications of the energy distribution can be resolved on an energy scale where the transmission probability changes significantly. F. Blatt calculated in which way this affects the emission current density [Bla63]:

$$\begin{aligned} J(x) &= J_0 \left(1 - \frac{1}{8x^2} + \frac{1}{4x^2} G(x)\right), \\ x &\equiv \frac{\epsilon_F}{\hbar\omega_c}, \\ G(x) &= \frac{1}{2} - 4\tilde{x}^2, \\ \tilde{x} = x + z, \quad z \in \mathbb{Z}, \quad -\frac{1}{2} &\le \tilde{x} < \frac{1}{2}. \end{aligned}$$

x is a measure for the inverse magnetic field strength, $G(x)$ is periodically extended to all x and accounts for the rising and falling of the Fermi energy due to normalization of the energy distribution. It is bounded to $|G(x)| < 0.5$. So even with a 7 T magnetic field, we obtain $x \approx 5.5 \cdot 10^3$, so that the corrections are suppressed by seven orders of magnitude.

In this chapter we demonstrated the extraction of a current of up to 10 μA. The current is emitted into a Penning trap formed by the magnetic field of the superconducting magnet and the electric potential created by the high voltage reflection electrodes on both ends. The electrons bounce back and forth until an equilibrium is reached between emission and loss due to Coulomb repulsion. There are several limits to the electron density in a trap. One is the Brillouin limit [DO99], at which the Coulomb repulsion compensates the radially trapping Lorentz force. It has the value

$$\rho_e = \frac{\varepsilon_0 B^2}{2m} = 2.4 \cdot 10^{14}\ \mathrm{cm}^{-3}$$

for electrons in a field of 7 T. The necessity for axial trapping defines another limit. The potential in the present case differs very much from a harmonic trapping potential, therefore don't apply the usual space charge limit of Penning traps. The strength of the electrostatic field must overcome the plasma repulsion and confine electrons with a kinetic energy of 750 eV. We model the field—experienced by an electron at the bottom of the almost cylindrical cloud—with a uniformly charged sphere of the same radius R and charge density $e\rho_e$ as the cylinder. The test electron is on the surface of the sphere. We account for the other charges further away with a factor 3, to be on the

safe side—their contribution is suppressed by the inverse square of the distance:

$$\mathcal{E}_e \approx 3\frac{\frac{4\pi}{3}R^3 e\rho_e}{4\pi\varepsilon_0 R^2} = \frac{e\rho_e R}{\varepsilon_0}$$

The potential in the reflection electrode drops over a distance in the order of the trap radius. We use only half of the voltage in respect of the kinetic energy of the electrons. The field $\mathcal{E}_r \approx 0.5$ kV/cm results in a limit of

$$\rho_e \approx \frac{\varepsilon_0 \mathcal{E}_r}{Re} = 4 \cdot 10^8 \text{ cm}^{-3}.$$

There are some reports on this so-called reflection mode [Don95, Her00], stating that—under similar conditions—an electron beam can be reflected several ten thousand times. This would lead to a current density of roughly 1 A/cm^2, or a density of $4 \cdot 10^9$ cm^{-3}. The considerations may be further modified, because of the observation of a non-uniform density—it decreases roughly with the inverse square root of the radius.

The number of reflections times the trap length, divided by the electron velocity gives the time in which the final amount of electrons is produced. It is below a millisecond. This also means that the electron energy can be controlled on the same time scale.

Chapter 8

Summary and Outlook

We have taken a glance at the motivations for a g-factor measurement and the theoretical description of this quantity. It was followed by an overview of the double-resonance technique and the setup in which it will be applied to medium-heavy and heavy highly charged ions. Then I reported on important preparations for the experiment, namely the design of a novel asymmetric harmonic trap and the production of boron-like argon ions. This includes field emission of electrons, controlled injection of gas and charge-breeding, resulting from the collision of both particle species.

We have found a trap geometry where the two lowest-order anharmonicities can be tuned out (compensated) simultaneously without shifting the motional frequencies of ions. The closed cylindrical shape has been modified to a design open on one side, so that ions can be loaded from the creation trap. The spectroscopy mesh leaves sufficient optical access for spectroscopy experiments. Nevertheless, there are no significant changes compared to the idealized trapping potential of a closed trap. This is a prerequisite for the determination of the bound-electron g-factor on a ppb level of accuracy.

The working principle of the cryogenic gas valve has been outlined. Simulations indicate that the valve should successfully seal the vacuum, at least against argon gas. At sufficient argon pressure from the outside, we are confident to find a sufficient number of atoms within the trap chamber.

The field emission points have been tested in a setup similar to the final layout. I have demonstrated that several tips emit a higher current than expected. These results of the electron source and the gas valve suggest that the required amount argon ions can be produced in a reasonable time interval.

The work of this thesis was mainly focused on design, drafting and construction of the electron source, the gas valve and an optical setup for laser spectroscopy. The recent delivery of the cryocooler marks the transition to a new stage in the preparations for the HITRAP g-factor experiment. We will soon test the adsorption valve to clarify the open questions. The lens system will be operated as soon as the image bundle has arrived. We will assemble the trap chamber and perform measurements of charge breeding and ion trapping.

After successful tests and experiments with argon and other potential medium-heavy candidates, we will move on to heavy ions. The heavy-ion synchrotron at GSI accelerates ions with

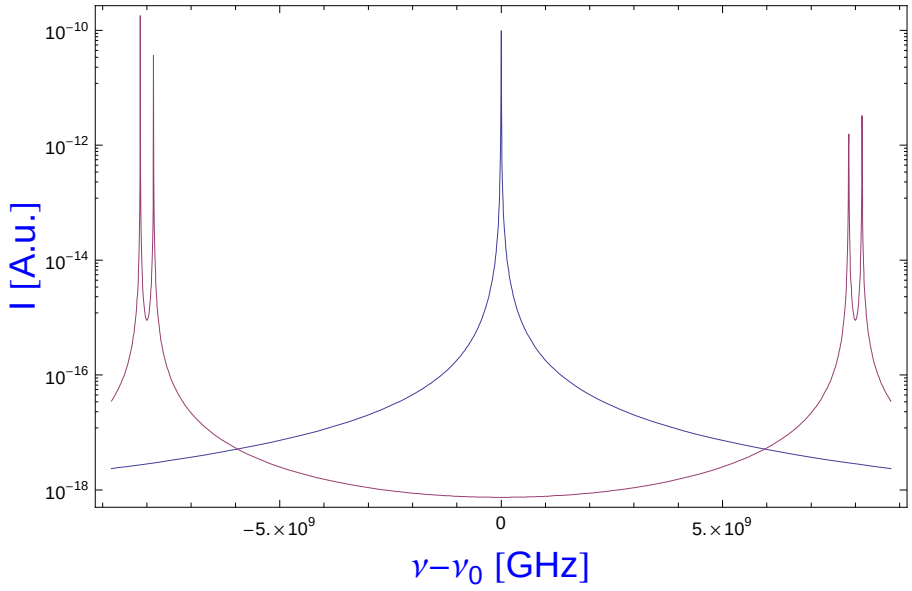

Figure 8.1: Detail of the line shape with magnetic field (two red double peaks, only circular polarization) and line shape without field (single blue peak). ν_0 is the field-free hyperfine-structure transition frequency.

medium charge to 400 MeV/u. They are then extracted to a stripper target, which produces a broad spectrum of high charge states. One particular state is selected and then cooled and decelerated in several steps, namely the experimental storage ring and two linear decelerator stages. A bunch of a hundred thousand heavy highly charged ions will be gathered in a Penning trap and further cooled to liquid helium temperature. This procedure is designed for a repetition rate of ten seconds [KBB+08].

If we consider hydrogen-like ions above a nuclear charge of about 60, there are several nuclides, for which the hyperfine-structure splitting of the $1s$ state is in the visible spectrum. This makes them candidates for double-resonance spectroscopy as well. Now, the total angular momentum and magnetic moment are composed from the respective quantities of the electron and the nucleus (having a momentum $\vec{I}$, magnetic moment μ_I and g-factor g_I):

$$g_F = g_J \cdot f(F,J,I) + g_I \cdot \frac{m_e}{m_p} \cdot f'(F,J,I), \tag{8.1}$$

where m_e/m_p is the mass ratio of electron and proton. It expresses that nuclear magnetic moments are usually three orders of magnitude smaller than the electron moment [Vog09]. Different possible level schemes are discussed in [QMSV08]. The composing g-factors in equation 8.1 can be disentangled, if g_F is measured in both hyperfine-structure levels. However, note the following observation: A particular feature of the double-resonance technique in hyperfine-structure transitions is explained using the example of hydrogen-like bismuth $^{209}Bi^{82+}$. It has a nuclear spin of $I = 9/2$, hyperfine-structure transition wavelength of 243 nm and Larmor frequency of $2\pi \cdot 16$ GHz. Figure 8.1 zooms in to a detail in the Zeeman-split line shape. The two components of the observed line doublets have opposite polarization ($\sigma+$ and $\sigma-$). The separation of the two lines is approximately $2\pi \cdot 300$ MHz and reflects the small value of the nuclear moment. If it was

resolved by a modulation technique or by scanning the ultraviolet laser in a controlled manner, we could derive the nuclear g-factor with even higher precision than what has been proposed in [QMSV08].

I want to close by coming back to the bound-electron g-factor. As I have stated in chapter 2, this quantity strongly depends on binding, QED and nuclear contributions. If the electron g-factor is measured in different charge states, these effects can be singled out, which opens the way for tests of bound-state QED calculations in the regime of strong fields with unprecedented accuracy. Further goals are the investigation of relativistic electron correlation effects and the determination of fundamental constants such as α. This would also increase the significance of QED tests by measurements of the free electron g-factor, which I have quoted in the introduction.

Appendix A

Angular Distribution

I want to motivate that the angular distribution of the fluorescence light emitted in the spontaneous M1 transition (such as the $2P_{3/2} - 2P_{1/2}$ decay) follows the same law as in the E1 transition, namely equation 5.4. The transition rate is determined with perturbation theory, which leads to Fermi's golden rule:

$$R = \frac{2\pi}{\hbar^2} \left|\langle i| H_{\text{int}} |f\rangle\right|^2 \delta(\omega_0 \pm \omega), \tag{A.1}$$

where ω_0 is the transition frequency and ω the frequency of the external field. I have already given the Hamiltonian operator of the magnetic dipole interaction in equation 2.4:

$$H_{\text{int}} = g_J \mu_B \frac{\vec{J}}{\hbar} \cdot \vec{B} \approx \frac{\mu_B}{\hbar} \left[\vec{L} + 2\vec{S}\right] \cdot \vec{B},$$

where I used the convenient approximation $g_S = 2$. While the static magnetic field $\vec{B}_0 = (0, 0, B_0)$ defines the coordinate system, the interaction of the decaying electron is with the field $\vec{B}_\omega$ of the emitted photon. This factor in the Hamiltonian does not act in the electron Hilbert space, therefore I want to calculate the transition matrix elements $\langle i| H_{\text{int}} |f\rangle \propto \langle i| \left[\vec{L} + 2\vec{S}\right] \cdot \vec{B}_\omega |f\rangle = \langle i| \left[\vec{L} + 2\vec{S}\right] |f\rangle \cdot \vec{B}_\omega$ independently and apply the scalar product afterwards.

Note the abbreviations for angular momentum states $|J, m_J\rangle$ as composed momenta from $L = 1$ and $S = 1/2$ with the Clebsch-Gordan coefficients:

$$\begin{aligned}
\left|\frac{3}{2}, \frac{3}{2}\right\rangle &= \left|1\,\frac{1}{2}; 1\,\frac{1}{2}\right\rangle \equiv |1\rangle\,|\uparrow\rangle \equiv |1\uparrow\rangle \\
\left|\frac{3}{2}, \frac{1}{2}\right\rangle &= \sqrt{\frac{1}{3}}\,|1\downarrow\rangle + \sqrt{\frac{2}{3}}\,|0\uparrow\rangle \\
\left|\frac{1}{2}, \frac{1}{2}\right\rangle &= \sqrt{\frac{2}{3}}\,|1\downarrow\rangle - \sqrt{\frac{1}{3}}\,|0\uparrow\rangle\,.
\end{aligned}$$

The equation $\vec{J} = \frac{1}{2}\vec{e}_x(J_+ + J_-) + \frac{1}{2i}\vec{e}_y(J_+ - J_-) + \vec{e}_z J_z$, where J_+ and J_- are rising and lowering operators for the z-component, holds for any angular momentum $\vec{J}$. We need the following relations

for ladder operators:

$$L_- |1\rangle = \hbar\sqrt{2}\,|0\rangle \qquad S_- |\uparrow\rangle = \hbar\,|\downarrow\rangle$$
$$L_+ |0\rangle = \hbar\sqrt{2}\,|1\rangle \qquad S_+ |\downarrow\rangle = \hbar\,|\uparrow\rangle\,.$$

Now we can calculate the matrix elements

$$\begin{aligned}
&\left\langle \frac{3}{2},\,\frac{3}{2}\right| \left[\vec{L}+2\vec{S}\right] \left|\frac{1}{2},\,\frac{1}{2}\right\rangle \\
&= \langle 1\uparrow| \left[\vec{L}+2\vec{S}\right] \left[\sqrt{\frac{2}{3}}\,|1\downarrow\rangle - \sqrt{\frac{1}{3}}\,|0\uparrow\rangle\right] \\
&= \langle 1\uparrow| \left[\sqrt{\frac{2}{3}}\,|\downarrow\rangle\,\vec{L}\,|1\rangle - \sqrt{\frac{1}{3}}\,|\uparrow\rangle\,\vec{L}\,|0\rangle + \sqrt{\frac{2}{3}}\,|1\rangle\,2\vec{S}\,|\downarrow\rangle - \sqrt{\frac{1}{3}}\,|0\rangle\,2\vec{S}\,|\uparrow\rangle\right] \\
&= -\sqrt{\frac{1}{3}}\,\langle 1|\,\vec{L}\,|0\rangle + \sqrt{\frac{2}{3}}\,|1\rangle\,\langle\uparrow|\,2\vec{S}\,|\downarrow\rangle \\
&= -\sqrt{\frac{1}{3}}\left[\frac{1}{2}\vec{e}_x\hbar\sqrt{2} + \frac{1}{2i}\vec{e}_y\hbar\sqrt{2}\right] + 2\sqrt{\frac{2}{3}}\left[\frac{1}{2}\vec{e}_x\hbar + \frac{1}{2i}\vec{e}_y\hbar\right] \\
&= \sqrt{\frac{2}{3}}\hbar\,[\vec{e}_x - i\vec{e}_y]
\end{aligned} \tag{A.2}$$

for the decay that changes m_J (σ-polarization), and

$$\begin{aligned}
&\left\langle \frac{3}{2},\,\frac{1}{2}\right| \left[\vec{L}+2\vec{S}\right] \left|\frac{1}{2},\,\frac{1}{2}\right\rangle \\
&= \left[\sqrt{\frac{1}{3}}\,\langle 1\downarrow| + \sqrt{\frac{2}{3}}\,\langle 0\uparrow|\right] \left[\vec{L}+2\vec{S}\right] \left[\sqrt{\frac{2}{3}}\,|1\downarrow\rangle - \sqrt{\frac{1}{3}}\,|0\uparrow\rangle\right] \\
&= \left[\sqrt{\frac{1}{3}}\,\langle 1\downarrow| + \sqrt{\frac{2}{3}}\,\langle 0\uparrow|\right] \left[\sqrt{\frac{2}{3}}\,|\downarrow\rangle\,\vec{L}\,|1\rangle - \sqrt{\frac{1}{3}}\,|\uparrow\rangle\,\vec{L}\,|0\rangle + \sqrt{\frac{2}{3}}\,|1\rangle\,2\vec{S}\,|\downarrow\rangle - \sqrt{\frac{1}{3}}\,|0\rangle\,2\vec{S}\,|\uparrow\rangle\right] \\
&= \sqrt{\frac{2}{9}}\,\langle 1|\,\vec{L}\,|1\rangle + \sqrt{\frac{2}{9}}\,\langle\downarrow|\,2\vec{S}\,|\downarrow\rangle - \sqrt{\frac{2}{9}}\,\langle 0|\,\vec{L}\,|0\rangle - \sqrt{\frac{2}{9}}\,\langle\uparrow|\,2\vec{S}\,|\uparrow\rangle \\
&= \sqrt{\frac{2}{9}}\hbar\vec{e}_z - \sqrt{\frac{2}{9}}\hbar\vec{e}_z - \sqrt{\frac{2}{9}}\hbar\vec{e}_z = -\sqrt{\frac{2}{9}}\hbar\vec{e}_z
\end{aligned} \tag{A.3}$$

for the decay connected with a π wave.

The probability to find an emitted photon with a particular magnetic field (amplitude) $\vec{B}_\omega$ can be derived from Fermi's golden rule, if this field vector is inserted in equation A.1. It follows that the probability distribution is proportional to the square of the scalar product of $\vec{B}_\omega$ and the term A.2 for the decay with σ polarization, which we are going to detect. Then the intensity is $I(\theta') \propto \left|[\vec{e}_x - i\vec{e}_y]\cdot\vec{B}_\omega\right|^2 \propto \sin^2\theta'$, where θ' is the angle between $\vec{B}_\omega$ and $\vec{e}_z$.

Now for an electromagnetic wave, the wave vector $\vec{k}$, indicating the direction of propagation, is perpendicular to the local magnetic field. I imagine two independent wave vector components, perpendicular to $\vec{B}_\omega$ and to each other. This is an intuitive argument, making plausible that $I(\theta)$ has the form

$$I(\theta) \propto 2 - \sin^2\theta = 1 + \cos^2\theta, \tag{A.4}$$

which is equal to the directional characteristic assumed in equation 5.4.

Helpful references on that topic can be found on the web:

http://pdg.lbl.gov/2008/reviews/clebrpp.pdf
http://www.iopb.res.in/~phatak/em/node25.html
http://cos.cumt.edu.cn/jpkc/dxwl/zl/zl1/Physical\%20Review\%20Classics/atomic/099.pdf
http://electron6.phys.utk.edu/qm2/modules/m10/time.htm
http://iopscience.iop.org/0034-4885/41/11/002/pdf
http://www-theor.ch.cam.ac.uk/software/cadpac/chap6/node19.html

Appendix B

Details about FEP Production

The tips have been produced from 1 mm thick rigid tungsten wire at a dedicated lab course experiment of Mainz University. The setup shown in figure B.1 applies the electrochemical etching process

$$\mathrm{W_{(s)}} + \mathrm{H^+_{(aq)}} \rightarrow \mathrm{W^+_{(aq)}} + \frac{1}{2}\mathrm{H_{2(g)}}$$

in a particular way which allows to shape a sharp point.

The top of a roughly 4 cm long tungsten wire is fixed to an alligator clip, which is connected to the positive pole of a VOLTCRAFT TNG 30 voltage supply. Thus the tungsten wire is the anode. A few mm below, the wire pierces through a lamella of highly concentrated sodium hydroxide base, suspended in a wire loop of 5 mm diameter, which forms the cathode.

When the supply is switched on to about 10 V, the process starts and tungsten ions dissolve from the wire surface, where it is covered with the base. The voltage supply drives the electrons to the anode, where they reduce protons—even in a base, there are always some hydronium ions. The only function of sodium hydroxide is to increase the electric field at the electrodes: Due to the high concentration of ions, the solution can be polarized and the electric field is shielded from the inside. The voltage drops mainly in the thin layers close to the two electrode surfaces, where accordingly the field is very strong. Then even a few volts are sufficient for field emission of electrons from the cathode and tungsten ions from the anode.

The wire narrows down leading to a hyperboloidal shape (see figure B.2). At the narrowest point the gravitational tension increases with the inverse square of the diameter, until the lower part of the wire breaks off. The etching process ceases immediately for this part, because it is disconnected from the anode. It falls down and is smoothly caught by a blob of shaving foam. This lower part later serves as cathode for field emission of electrons.

From the production on, the sharpened wires have to be handled very carefully. Any contact and also strong impacts could distort and thus destroy the tender tip. After a wire has been picked up from the foam breaker with forceps it is rinsed with distilled water to remove ions, which could condense to a crystal on the tip. Then each wire is taped onto a foam plastic pad with a number written on the tape. Together with the pad, the tips are laid into a plastic case and wrapped in another Styrofoam filled box for protection (see figure B.3)

It seems helpful to make some practical remarks for readers who want to repeat the procedure:

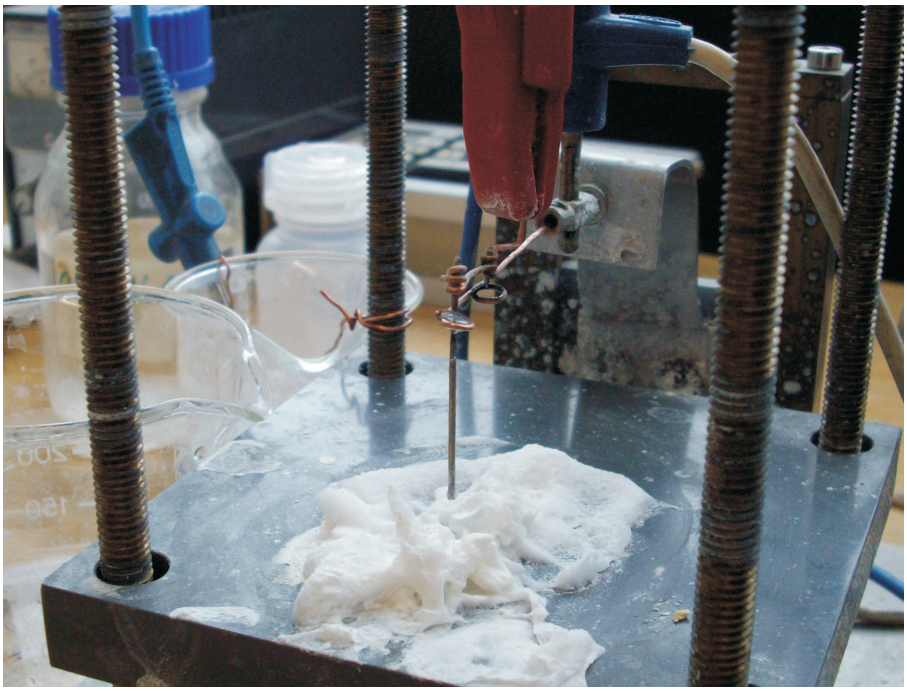

Figure B.1: The production setup in Mainz. One tip has fallen down and been taken away from the shaving foam, the second one is almost finished.

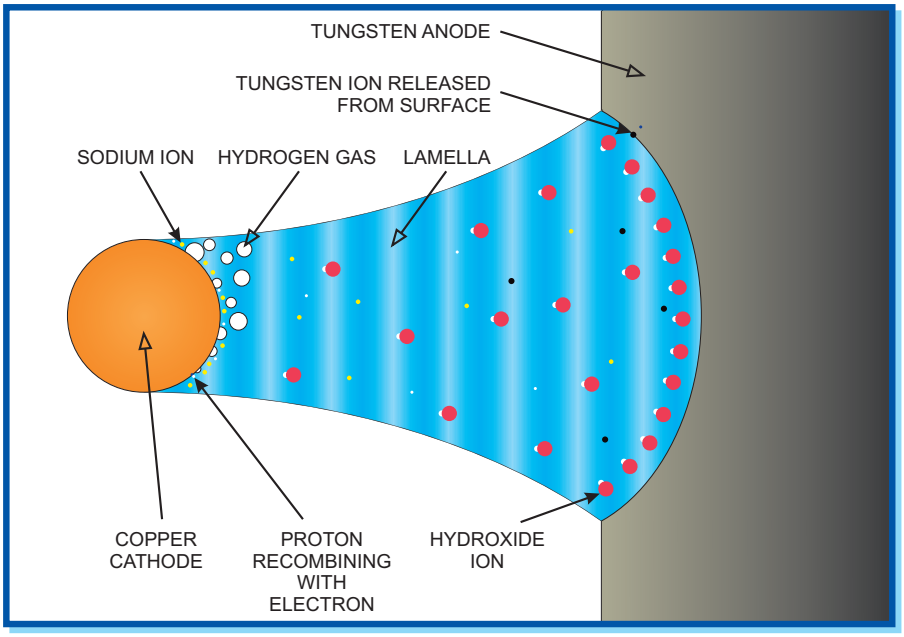

Figure B.2: The etching process, viewed in section through the tungsten wire, copper loop and sodium hydroxide lamella. Zoomed in to the left-hand side.

Figure B.3: Transport and storage box with tungsten wires. The tips point into the space that has been cut free from foam plastic.

The setup is designed to use 100 μm wire, for which the process naturally lasts significantly shorter than for the 1 mm wire that I used. In order to speed up the production, two wires were etched in parallel. Another significant modification due to the wire diameter is its much heavier weight of our wire compared to the thin one. Under the simple assumption stated above, the fracture diameter d' can be derived from the ultimate tensile strength $\sigma \approx 1.5$ GPa [TW65], gravitational acceleration g, tungsten density $\rho_{\mathrm{W}} = 19.3\,\mathrm{g/m^3}$ and the length l and diameter d of the lower part of the wire:

$$\begin{aligned} \pi \left(\frac{d'}{2}\right)^2 \sigma = F_G = \pi \left(\frac{d}{2}\right)^2 \rho g l \\ \Rightarrow d' = d\sqrt{\rho l g/\sigma}. \end{aligned} \tag{B.1}$$

According to this consideration, a 3 cm long wire will only be constricted by three orders of magnitude (more precisely, by a factor of $2 \cdot 10^{-3}$) which is consistent with measurements of tips produced from the 100 μm wire [Ota07]. However, later tests with the tips made from the thick wire (see section 7.3) did not confirm this consideration, but yielded much better results.

Originally a different voltage supply than the one described here was foreseen for this procedure. It comprises a current limiting control, which automatically switches off the voltage if a current increase indicates that a tip is finished. This is particularly necessary if one intends to use the upper part of a wire. As a drawback, the maximal output current is too low for processing the thick wire in a reasonable amount of time. Besides, the sensitive switching mechanism is often prematurely triggered. So it was soon replaced by the VOLTCRAFT supply, since the switching is not needed for a good quality of the lower part. Even with this supply, the production of two

tips takes about an hour. During this time, the liquid often has to be refreshed, because some of it is spilled due to the rapid formation of hydrogen.

Unfortunately, the tungsten wire (of which there is still more than a meter spare material left) is a little thicker than 1 mm and fits neither into the channel of the FEP support electrode F1 nor into the insulating bead (see figure 7.1). So a second bath was prepared and four wire pieces together with an additional cathode were suspended into it to prepare them, while two pieces were in the main procedure.

This bath was also used to clean the wires (particularly the tips) from spots resembling oil. These are probably residuals of the insulating layer around the copper wire used for contacting everything. The layer had been partially sandpapered, but some of it may have dissolved in the sodium hydroxide base.

Appendix C

The Sumitomo Cold-Head

The cold-head has been described in section 4.1. I mentioned that it will sometimes be open for cold-temperature tests, as a service for other groups as well. For this reason I quote the drawing supplied by Sumitomo. It is depicted in figure C.1.

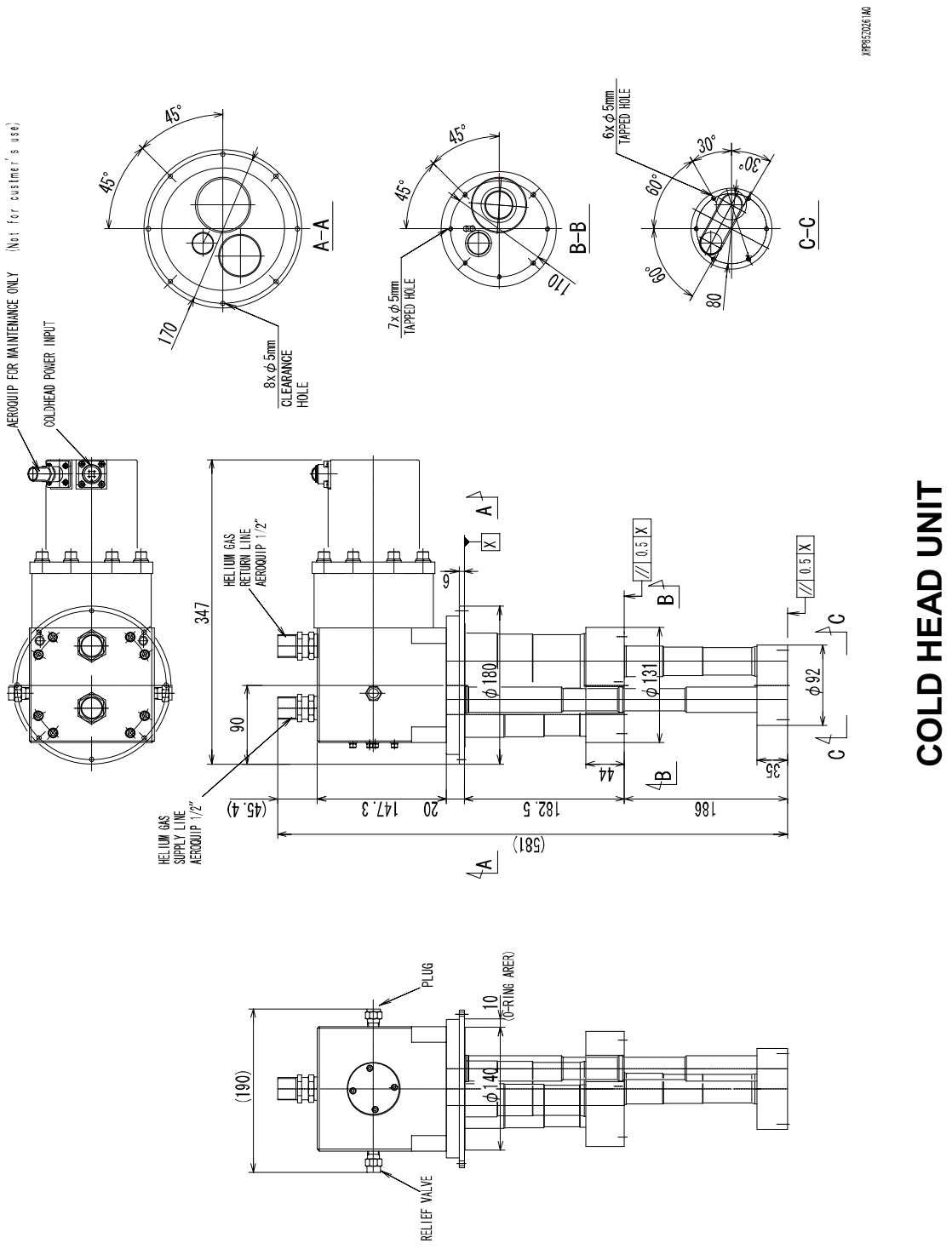

Figure C.1: Technical drawing of the Sumitomo cold-head [SHI08a].

Bibliography

[AHKN07] T. Aoyama, M. Hayakawa, T. Kinoshita, and M. Nio. Revised Value of the Eighth-Order Contribution to the Electron $g-2$. *Phys. Rev. Lett.*, 99(110406), 2007.

[BDH+05] T. Beier, S. Djekic, H. Häffner, P. Indelicato, H.-J. Kluge, W. Quint, V.M. Shabaev, J. Verdú, T. Valenzuela, G. Werth, and V.A. Yerokhin. Determination of the electron's mass from g-factor experiments on $^{12}C^{5+}$ and $^{16}O^{7+}$. *Nucl. Instr. and Meth. in Phys. B*, 205(15), 2005.

[BG82] L.S. Brown and G. Gabrielse. Precision spectroscopy of a charged particle in an imperfect Penning trap. *Phys. Rev. A*, 25(2423), 1982.

[BHH+02] T. Beier, H. Häffner, N. Hermanspahn, S.G. Karshenboim, H.-J. Kluge, W. Quint, S. Stahl, J. Verdú, and G. Werth. New determination of the electron's mass. *Phys. Rev. Lett.*, 88(011603), 2002.

[BKH53] R.E. Burgess, H. Kroemer, and J.M. Houston. Corrected Values of Fowler-Nordheim Field Emission Functions $v(y)$ and $s(y)$. *Phys. Rev.*, 90(515), 1953.

[BKS06] R. Becker, O. Kester, and Th. Stöhlker. Simulation of charge breeding for trapped ions. In *HCI*, 2006.

[Bla63] F.J. Blatt. Field Emission in a Magnetic Field. *Phys. Rev.*, 131(1), 1963.

[Bre28] G. Breit. The magnetic moment of the electron. *Nature*, 122(649), 1928.

[BRM00] V.A. Bernshtam, Yu.V. Ralchenko, and Y. Maron. Empirical formula for cross section of direct electron impact ionization of ions. *J. Phys. B*, 33(5025), 2000.

[CdMC+08] M. Cadoret, E. de Mirandes, P. Cladé, S. Guellati-Khélifa, C. Schwob, F. Nez, L. Julien, and F. Biraben. Combination of Bloch Oscillations with a Ramsey-Bordé Interferometer: New Determination of the Fine Structure Constant. *Phys. Rev. Lett.*, 101(230801), 2008.

[CHK+10] C.W. Chou, D.B. Hume, J.C.J Koelemeij, D.J. Wineland, and T. Rosenband. Frequency Comparison of Two High-Accuracy Al^+ Optical Clocks. *Phys. Rev. Lett.*, 104(070802), 2010.

[DCLUD+03] I. Draganić, J.R. Crespo López-Urrutia, R. DuBois, S. Fritzsche, V.M. Shabaev, R. Soria Orts, I.I. Tupitsyn, Y. Zou, and J. Ullrich. High Precision Wavelength

Measurements of QED-Sensitive Forbidden Transitions in Highly Charged Argon Ions. *Phys. Rev. Lett.*, 91(183001), 2003.

[DDD+09] D.E. Donets, E.D. Donets, E.E. Donets, V.V. Salnikov, V.B. Shutov, and E.M. Syresin. Production and ion-ion cooling of highly charged ions in electron string ion source. *Rev. Sci. Instrum.*, 80(063304), 2009.

[DE73] H. Dehmelt and P. Ekstrom. Proposed $g-2$ experiment on stored single electron or positron. *Bull. Am. Phys. Soc.*, 18(727), 1973.

[Deh84] H. Dehmelt. g-Factor of electron centered in symmetric cavity. *Proc. Natl. Acad. Sci. USA*, 81(8037), 1984. Erratum ibidem 82(6366), 1985.

[Dir28] P.A.M. Dirac. The Quantum Theory of the Electron. *Proc. Roy. Soc. London A*, 117(610), 1928.

[DO99] D.H.E. Dubin and T.M. O'Neil. Trapped nonneutral plasmas, liquids, and crystals (the thermal equilibrium states). *Rev. Mod. Phys.*, 71(1), 1999.

[Don95] E.D. Donets. Review of Recent Developments for Electron-Beam Ion Sources (EBIS). *Rev. Sci. Instrum.*, 67(873), 1995.

[FBM93] W. Friess, T. Brunner, and D. Menzel. Nonwetting and Stickung of Argon on Alkali Metal Surfaces. *Surface Sc.*, 307–309(182), 1993.

[FK07] V.V. Flambaum and M.G. Kozlov. Enhanced Sensitivity to the Time Variation of the Fine-Structure Constant and m_p/m_e in Diatomic Molecules. *Phys. Rev. Lett.*, 99(150801), 2007.

[FN28] R.H. Fowler and L.W. Nordheim. Electron emission in intense electric fields. *Proc. R. Soc. Lond.*, A119(173), 1928.

[Foo05] C.J. Foot. *Atomic Physics*. Oxford University Press, 2005.

[FRG+95] V. Fisher, Yu. Ralchenko, A. Goldgirsh, D. Fisher, and Y. Maron. A scaling of multiple ionization cross sections. *J. Phys. B*, 28(3027), 1995.

[GHR89] G. Gabrielse, L. Haarsma, and S. L. Rolston. Open-endcap Penning traps for high precision experiments. *Int. J. of Mass Spectrom. and Ion Processes*, 88(319), 1989.

[GM84] G. Gabrielse and F.C. Mackintosh. Cylindrical Penning traps with orthogonalized anharmonicity compensation. *Int. J. of Mass Spectrom. and Ion Processes*, 57(1), 1984.

[Hae81] R. Haefer. *Kryo-Vakuumtechnik. Grundlagen und Anwendungen*, page 60. Springer, Berlin, 1981.

[HBH+00] H. Häffner, T. Beier, N. Hermanspahn, H.-J. Kluge, W. Quint, S. Stahl, J. Verdú, and G. Werth. High-Accuracy Measurement of the Magnetic Moment Anomaly of the Electron Bound in Hydrogenlike Carbon. *Phys. Rev. Lett.*, 85(255308), 2000.

[Her00] N. Hermanspahn. Das magnetische Moment des gebundenen Elektrons in wasserstoffartigem Kohnenstoff (C^{5+}). PhD thesis, Johannes-Gutenberg-Universität Mainz, 2000.

[HFG08] D. Hanneke, S. Fogwell, and G. Gabrielse. New Measurement of the Electron Magnetic Moment and the Fine Structure Constant. *Phys. Rev. Lett.*, 100(120801), 2008.

[Hun75] F. Hund. *Geschichte der Quantentheorie*. Bibliographisches Institut, Mannheim, Germany, 1975.

[HW00] H. Haken and H.C. Wolf. *Atom- und Quantenphysik*. Springer, Heidelberg, 2000.

[IYF04] T. Ishiyama, T. Yano, and S. Fujikawa. Molecular dynamics study of kinetic boundary conditions at an interface between argon vapor and its condensed phase. *Surface Sc.*, 16(8), 2004.

[Jac75] J.D. Jackson. *Classical Electrodynamics*. Wiley, New York, 1975.

[KBB+08] H.-J. Kluge, T. Beier, K. Blaum, L. Dahl, S. Eliseev, F. Herfurth, B. Hofmann, O. Kester, S. Koszudowski, C. Kozhuharov, G. Maero, W. Nörtershäuser, J. Pfister, W. Quint, U. Ratzinger, A. Schempp, R. Schuch, Th. Stöhlker, R.C. Thompson, M. Vogel, G. Vorobjev, D.F.A. Winters, and G. Werth. Chapter 7 HITRAP: A Facility at GSI for Highly Charged Ions. In S. Salomonson and E. Lindroth, editors, *Current Trends in Atomic Physics*, volume 53 of *Advances in Quantum Chemistry*, page 83. Academic Press, 2008.

[KF47] P. Kusch and H.M. Foley. Precision measurement of the ratio of the atomic g values in the $^2P_{3/2}$ and $^2P_{1/2}$ states of gallium. *Phys. Rev.*, 72(1256), 1947.

[KF48] P. Kusch and H.M. Foley. On the intrinsic moment of the electron. *Phys. Rev.*, 74(250), 1948.

[KPR+00] L. Khriachtchev, M. Pettersson, N. Runeberg, J. Lundell, and M. Räsänen. A stable argon compound. *Nature*, 406(6798), 2000.

[Kra26] H.A. Kramers. Wellenmechanik und halbzählige Quantisierung. *Z. Phys.*, 39(828), 1926.

[LBB+11] D. Lindenfels, N.P.M. Brantjes, G. Birkl, W. Quint, V.M.Shabaev, and M. Vogel. Bound Electron g-Factor Measurement by Double-Resonance Spectroscopy on a Fine-Structure Transition. *Can. J. Phys.*, 89(1), 2011.

[Lev71] L.L. Levenson. Condensation Coefficients of Argon, Krypton, Xenon, and Carbon Dioxide Measured with a Quartz Crystal Microbalance. *J. Vac. Sci. Technol.*, 8(629), 1971.

[LGL+07] B. Levitt, G. Gabrielse, P. Larochelle, D. Le Sage, W.S. Kolthammer, R. McConnell, J. Wrubel, A. Speck, D. Grzonka, W. Oelert, T. Sefzick, Z. Zhang, D. Comeau, M.C.

George, E.A. Hessels, C.H. Storry, M. Weel, and J. Walz. Single-component plasma of photoelectrons. *Phys. Lett. B*, 656(25), 2007.

[Lin08] D. Lindenfels. Report on Considerations for the Design of a Precision Trap. 2008.

[LJCLU+05] A. Lapierre, U.D. Jentschura, J.R. Crespo López-Urrutia, J. Braun, G. Brenner, H. Bruhns, D. Fischer, A.J. González Martínez, Z. Harman, W.R. Johnson, C.H. Keitel, V. Mironov, C.J. Osborne, G. Sikler, R. Soria Orts, V. Shabaev, H. Tawara, I.I. Tupitsyn, J. Ullrich, and A. Volotka. Relativistic Electron Correlation, Quantum Electrodynamics, and the Lifetime of the $1s^2 2s^2 2p\,^2P^o_{3/2}$ Level in Boronlike Argon. *Phys. Rev. Lett.*, 95(183001), 2005.

[LL91] L.D. Landau and E.M. Lifshitz. *Quantum mechanics*. Pergamon, Oxford, 1991.

[Lot67] W. Lotz. An Empirical Formula for the Electron-Impact Ionization Cross-Section. *Z. Phys.*, 206(205), 1967.

[Mae08] G. Maero. Cooling of highly charged ions in a Penning trap for HITRAP. PhD thesis, Ruprecht-Karls-Universität Heidelberg, 2008.

[Mag08] Magnex Scientific / Varian Inc / Agilent Technologies. 7T/160AS Vertical Magnet Customer Interface ANZ341861A. Unpublished, Nov 2008.

[Mag09a] Magnex Scientific / Varian Inc / Agilent Technologies. 21210 axial field 0 to 4m.xls. Unpublished, Nov 2009.

[Mag09b] Magnex Scientific / Varian Inc / Agilent Technologies. Site Acceptance Document. Unpublished, Dec 2009.

[Mag09c] Magnex Scientific / Varian Inc / Agilent Technologies. Technical Specifications TS1644B. Unpublished, Jan 2009.

[Mah05] G. Mahler. *Die Grundlagen der Fernsehtechnik*. Springer, Heidelberg, 2005.

[Mar10] C. Marzini. Simulations with CBSIM and Molflow. Private communication, 2010.

[Mes10] D. Meschede. *Gerthsen Physik*. Springer, 2010.

[MGW05] F.G. Major, V.N. Gheorghe, and G. Werth. *Charged Particle Traps*. Springer, Heidelberg, 2005.

[MR82] J. Mehra and H. Rechenberg. *The Historical Development of Quantum Theory*, volume 1. Springer, New York, 1982.

[MS08] O. Malyshev and F. Sharipov. Software for Modelling of Free Molecular Flows, 2008.

[Nor28] L.W. Nordheim. The Effect of the Image Force on the Emission and Reflexion of Electrons by Metals. *Proc. R. Soc. Lond.*, A121(788), 1928.

[NTZ07] H. Nersisyan, C. Toepffer, and G. Zwicknagel. *Interactions between Charged Particles in a Magnetic Field*. Springer, Heidelberg, 2007.

[Ota07] J.A. Otamendi. Development of an Experiment for Ultrahigh-Precision g-Factor Measurements in a Penning-Trap Setup. PhD thesis, Johannes-Gutenberg-Universität Mainz, 2007.

[PCJY05] K. Pachucki, A. Czarnecki, U.D. Jentschura, and V.A. Yerokhin. Complete two-loop correction to the bound-electron g factor. *Phys. Rev. A*, 72(022108), 2005.

[PSS+97] H. Persson, S. Salomonson, P. Sunnergren, I. Lindgren, and M.G.H. Gustavsson. A theoretical survey of QED tests in highly charged ions. *Hyperfine Int.*, 108(3), 1997.

[QMSV08] W. Quint, D.L. Moskovkhin, V.M. Shabaev, and M. Vogel. Laser-mirowave double-resonance technique for g-factor measurements in highly charged ions. *Phys. Rev. A*, 78(032517), 2008.

[Qui95] W. Quint. The g_j Factor of Hydrogenic Ions. *Phys. Scripta*, T59(203), 1995.

[RHS+08] T. Rosenband, D.B. Hume, P.O. Schmidt, C.W. Chou, A. Brusch, L. Lorini, W.H. Oksay, R.E. Drullinger, T.M. Fortier, J.E. Stalnaker, S.A. Diddams, W.C. Swann, N.R. Newbury, W.M. Itano, D.J. Wineland, and J.C. Bergquist. Frequency Ratio of Al^+ and Hg^+ Single-Ion Optical Clocks; Metrology at the 17th Decimal Place. *Science*, 319(1808), 2008.

[Sch48] J. Schwinger. On quantum-electrodynamics and the magnetic moment of the electron. *Phys. Rev.*, 73(416), 1948.

[Sch09] M. Schwarz. Wärmeleitfähigkeit supraleitender Kompositleiter im Temperaturbereich von 4 K bis 300 K. PhD thesis, Universität (TH) Karlsruhe, Germany, 2009.

[SG22] O. Stern and W. Gerlach. Das magnetische Moment des Silberatoms. *Z. Phys.*, 9(353), 1922.

[SGO+06] V.M. Shabaev, D.A. Glazov, N.S. Oreshkina, A.V. Volotka, G. Plunien, H.-J. Kluge, and W. Quint. g-Factor of Heavy Ions: A New Access to the Fine Structure Constant. *Phys. Rev. Lett.*, 96(253002), 2006.

[SGS+02] V.M. Shabaev, D.A. Glazov, M.B. Shabaeva, V.A. Yerokhin, G. Plunien, and G. Soff. g-factor of high-Z lithiumlike ions. *Phys. Rev. A*, 65(062104), 2002.

[Sha10] V.M. Shabaev. Preliminary calculation for boron-like argon. Private communication, 2010.

[SHI08a] SHI Cryogenics Group. RP-082B Cold Head. Unpublished, 2008.

[SHI08b] SHI Cryogenics Group. SRP-082B_datasheet. Unpublished, 2008.

[Sta98] S. Stahl. Aufbau eines Experiments zur Bestimmung elektronischer g-Faktoren einzlner wasserstoffähnlicher Ionen. PhD thesis, Johannes-Gutenberg-Universität Mainz, 1998.

[SVDJD81] P.B. Schwingberg, R.S. Van Dyck Jr., and H.G. Dehmelt. Preliminary comparison of the positron and electron spin anomalies. *Phys. Rev. Lett.*, 47(1679), 1981.

[Tin86] Tingwei Xu and J-M. Laurent and O. Gröbner. Monte Carlo Simulation of the Pressure and of the Effective Pumpiung Speed in the Large Electron Positron Collider (LEP). Technical Report LEP-VA/86-02, CERN, 1986.

[TW65] T.E. Tietz and J.W. Wilson. *Behavior and Properties of Refractory Metals.* Tokyo University International Edition, 1965.

[Ulm06] S. Ulmer. Entwicklung eines experimentellen Aufbaus zur Messung des g-Faktors des Protons in einer Penning-Falle. Diploma thesis, Ruprecht-Karls-Universität Heidelberg, 2006. (Engl. translation: Development of an experimental setup for the measurement of the proton g-factor in an Penning trap).

[Umr97] W. Umrath. *Grundlagen der Vakuumtechnik.* Leybold Vakuum GmbH, Köln, 1997.

[UWS02] UWS Umweltmanagement GmbH. Berufsgenossenschaftliche Vorschriften (BGV) B11 - Eletromagnetische Felder. http://www.umwelt-online.de/regelwerk/arbeitss/uvv/bgvb/b11_ges.htm, 2002.

[VAB+08] M. Vogel, J. Alonso, K. Blaum, W. Quint, B. Schabinger, S. Sturm, J. Verdú, A. Wagner, and G. Werth. The anomalous magnetic moment of the electron in hydrogenlike ions. A test of bound-state QED: Recent, present and future precision experiments. *Eur. Phys. J. Special Topics*, 163(113), 2008.

[VAD+05] M. Vogel, J. Alonso, S. Djekic, H.-J. Kluge, W. Quint, S. Stahl, J. L. Verdú, and G. Werth. Towards electronic g-factor measurements in medium-heavy hydrogenlike and lithium-like ions. *Nucl. Instr. and Meth. in Phys. Res. B*, 235(7), 2005.

[VDS+04] J. Verdú, S. Djekic, S. Stahl, T. Valenzuela, M. Vogel, G. Werth, T. Beier, H.-J. Kluge, and W. Quint. Electronic g-factor of hydrogenlike oxygen $^{16}O^{7+}$. *Phys. Rev. Lett.*, 92(093002), 2004.

[Vog09] M. Vogel. The anomalous magnetic moment of the electron. *Contemp. Phys.*, 50(437), 2009.

[VQN10] M. Vogel, W. Quint, and W. Nörtershäuser. Trapped Ion Oscillation Frequencies as Sensors for Spectroscopy. *Sensors*, 10(2169), 2010.

[Wei67] S. Weinberg. A model of leptons. *Phys. Rev. Lett.*, 19(21), 1967.

[WVST06] D.F.A. Winters, M. Vogel, D. Segal, and R.C. Thompson. Electronic detection of charged particle effects in a Penning trap. *J. Phys. B*, 39(3131), 2006.

[Zap79] S.A. Zapryagaev. A theoretical survey of QED tests in highly charged ions. *Opt. Spectrosc.*, 47(9), 1979.

[Zwi06] G. Zwicknagel. Electron Cooling of Highly Charged Ions in Penning Traps. In M. Drewsen, U. Uggerhoj, and H. Knudsen, editors, *Non-neutral Plasma Physics VI.* AIP Conf. Proc., 2006.

Danksagung

Wolfgang, du bist ein sehr freundlicher und geduldiger Chef! Dich schickte der Himmel, als ich in meinem Studium zwar viele Möglichkeiten, aber keine Orientierung hatte. Danke für alle Motivation und alles, was ich von dir lernen kann. Ich schätze sehr, dass ich meine Fragen meistens unmittelbar mit dir klären kann. Auch dein erfolgreicher Einsatz für meine Zukunft ist mir wertvoll.

Manuel beeindruckt und inspiriert mich durch sein scheinbar unerschöpfliches Wissen auf allen möglichen Gebieten, sei es relevant oder einfach nur interessant. Danke für deine weisen Ratschläge und deine Verlässlichkeit, insbesondere bei Korrekturen!

Sören Engelmann, auch dich hat der Himmel geschickt. Besonderen Dank für die Vakuumkammer, ohne die ich vielleicht immer noch ein Schreibtischtäter wäre.

Unsere beiden Praktikanten, Christoph und Markus, seien auch erwähnt. Inhaltlichen Austausch hatte ich bislang mehr mit Christoph - danke für die wertvolle Zusammenarbeit. Aber ihr seid beide wertvolle Ergänzungen!

Klaas, thank you for taking the time to generate the images. Also your valuable preparations for the g-factor experiment shall not be forgotten.

Vielen Dank für die freundliche Förderung durch Thomas Stöhlker und Klaus Blaum.

Many more colleagues enriched my work with helpful discussions or other support. I deeply appreciate your equipment, experience and patience: The entire HITRAP group, Christophor Kozhuharov, Evgeny Donets, Vitaly Shutov (I hope, I got the name right), Günter Werth, Stefan Stahl, Stefan Ulmer, Birgit Schabinger, Vladimir Shabaev, Stephan Fritzsche, Andrej Surzhykov, Jörg Kurdal, Stefan Wilfert, Rosemarie Vincelli, Benjamin Botermann, José Crespo, Reinard Becker and many others.

Meinen Kollegen A. Bardonner, N. Bönsch, T. Dettinger, M. Eck, R. Erlenbach, R.-J. Heinz, E. Kammer, M. Müller, D. Racano, R. Reiter, M. Romig und E. Wagner gebührt Anerkennung für ihre hervorragende technische Arbeit und Beratung. Wo wären wir ohne Sie?

Danke, Herr Prof. Neumann, dass Sie das Zweitgutachten übernommen haben.

Fabrizio und Laura habe ich im vergangenen Jahr sehr lieb gewonnen, weit über den fachlichen Austausch hinaus. Sollten sich unsere Wege doch trennen, was ich nicht hoffe - seid gesegnet!

Auch Alex, Sebastian, Sergiy und Regina mag ich gern. Good boy, Serge!

Pierre danke ich für die Tipps zur Diplomarbeit. Wir können den Kontakt auch gerne darüber hinaus vertiefen.

Frau Knop ist eine sehr angenehme Vermieterin.

Nun möchte ich einigen Freunden und Bekannten aus meiner Zeit in Lüneburg (Florian,

Bastemeyers, Marina, Moritz, Philipp, Sebastian, Birte, Gudrun, Juliane, Knut, Kuhagens, Marcel, Rebecca, Stefan, Ingrid, K. Riggert), Villingen (Daniel, Hannah, Speitelsbachs, S. Karin, überhaupt den Aidlinger Schwestern) und Heidelberg (Silke, Steffen, Thomas, Achenbachs, Beckers, Böhnkes, Joachim, Peterschmitts, Carmen, Holk, Michael, Stefan, Johannes, Kathrin, Michael und Maria, Denis, Hannes, Kai, Romain, Stephan, Thorben, Simon, Felix und Maren) herzlich danken, dass sie da sind. Besonders genannt seien zudem Benni, Bergers, Martin, Nelson, Ollmann, Robert, Selli, Zäddi, Christian, Marcel, Knittels, Alex, Christina, Ellen und Joscha aus meiner Gemeinde, der Ecclesia Darmstadt. Wer nicht erwähnt ist, sei mir nicht böse. Ihr seid Spitze!

Vielen Dank meiner Familie, besonders meinem Bruder, Mitbewohner und Freund Albrecht. Du hattest in den letzten Wochen nicht viel zu lachen mit mir. Danke für die Lasten, die du mir in der heißen Phase abgenommen hast, auch für deine leckeren Gerichte. Und so ein bisschen Ablenkung tut auch ganz gut... Birgit und Christoph, ich freue mich über jede Begegnung mit euch. Arnims und Großmami, euch sehe ich hoffentlich bald wieder. Mami und Papi, danke für eure Liebe und Unterstützung, die ich gar nicht umfassend würdigen kann! Euer Zuhören, Beraten, Ermahnen, eure Gedanken - heute und natürlich auch früher. Ich habe euch lieb. Ich kann auch nur danken für die finanzielle Versorgung. Nicht auszudenken, wenn ich neben dem Studium hätte ernsthaft arbeiten müssen!

Danke allen Freunden für eure Geduld, euer Ermutigen, euer Schweigen und beten. Aber der größte Dank gilt meinem himmlischen Vater, der gar nicht nur im Himmel ist, sondern eure und meine Gebete hört und spürbar für mich da ist. Wo wäre ich, wenn DU mich nicht immer wieder gestärkt und motiviert hättest? Danke für diese schöne Welt, die ich erforschen darf. Danke, dass du größer bist als jeder Berg. Ich brauche vor der Schlange nicht zu erstarren, du hast ihr den Kopf zertreten! Danke, dass es mehr gibt als eine nicht perfekte Diplomarbeit. Du hast mich an den neuen Himmel und die neue Erde erinnert, als ich es am meisten brauchte. Und danke für die vielen konkreten Hilfen, Auswege, Ideen, das Gelingen - alles, was ich habe, verdanke ich dir!

So möchte ich schließen mit einem Zitat aus dem Verhör des Apostels Paulus durch König Herodes Agrippa II. und Statthalter Festus:

> "[...] Aber bis heute hat Gott mir geholfen, und so stehe ich als sein Zeuge vor den Menschen, den hoch gestellten wie den ganz einfachen. Ich verkünde nichts anderes, als was die Propheten und Mose angekündigt haben: Der versprochene Retter, sagten sie, muss leiden und sterben und wird als der Erste unter allen Toten auferstehen, um dem jüdischen Volk und allen Völkern der Welt das rettende Licht zu bringen."
>
> Als Paulus sich auf diese Weise verteidigte, rief Festus ihm zu: "Du bist verrückt geworden, Paulus! Das viele Studieren hat dich um den Verstand gebracht!" Paulus aber antwortete: "Hochverehrter Festus, ich bin nicht verrückt. Was ich sage, ist wahr und vernünftig. [...]"
>
> Apostelgeschichte Kapitel 26, Verse 22-25, Gute Nachricht Bibel

Erklärung:

Ich versichere, dass ich diese Arbeit selbstständig verfasst habe und keine anderen als die angegebenen Quellen und Hilfsmittel benutzt habe.

Heidelberg, den 15.11.2010 .....